

Numerical Assessment of the Performance of Jet-Wing Distributed Propulsion on Blended-Wing-Body Aircraft

Vance Fredrick Dippold, III

A Thesis submitted to the Faculty of
Virginia Polytechnic Institute and State University
In partial fulfillment of the requirements for the degree of

Master of Science
In
Aerospace Engineering

J.A. Schetz, Chair

W.H. Mason

B. Grossman

July 28, 2003
Blacksburg, Virginia

Keywords: Computational Fluid Dynamics, Jet-Wing, Jet-Flap,
Distributed Propulsion, Blended-Wing-Body

Copyright © 2003, Vance F. Dippold, III

Numerical Assessment of the Performance of Jet-Wing Distributed Propulsion on Blended-Wing-Body Aircraft

Vance F. Dippold, III

(ABSTRACT)

Conventional airliners use two to four engines in a Cayley-type arrangement to provide thrust, and the thrust from these engines is typically concentrated right behind the engine. Distributed propulsion is the idea of redistributing the thrust across most, or all, of the wingspan of an aircraft. This can be accomplished by using several large engines and using a duct to spread out the exhaust flow to form a jet-wing or by using many small engines spaced along the span of the wing. Jet-wing distributed propulsion was originally suggested by Kuchemann as a way to improve propulsive efficiency. In addition, one can envision a jet-wing with deflected jets replacing flaps and slats and the associated noise.

The purpose of this study was to assess the performance benefits of jet-wing distributed propulsion. The Reynolds-averaged, finite-volume, Navier-Stokes code GASP was used to perform parametric computational fluid dynamics (CFD) analyses on two-dimensional jet-wing models. The jet-wing was modeled by applying velocity and density boundary conditions on the trailing edges of blunt trailing edge airfoils such that the vehicle was self-propelled. As this work was part of a Blended-Wing-Body (BWB) distributed propulsion multidisciplinary optimization (MDO) study, two airfoils of different thickness were modeled at BWB cruise conditions. One airfoil, representative of an outboard BWB wing section, was 11% thick. The other airfoil, representative of an inboard BWB wing section, was 18% thick. Furthermore, in an attempt to increase the propulsive efficiency, the trailing edge thickness of the 11% thick airfoil was doubled in size. The studies show that jet-wing distributed propulsion can be used to obtain propulsive efficiencies on the order of turbofan engine aircraft. If the trailing edge thickness is expanded, then jet-wing distributed propulsion can give improved

propulsive efficiency. However, expanding the trailing edge must be done with care, as there is a drag penalty. Jet-wing studies were also performed at lower Reynolds numbers, typical of UAV-sized aircraft, and they showed reduced propulsive efficiency performance. At the lower Reynolds number, it was found that the lift, drag, and pitching moment coefficients varied nearly linearly for small jet-flap deflection angles.

Acknowledgements

I would like to thank my advisor, Dr. Schetz, for his guidance and patience with my work. Under his suggestion, I joined the Multidisciplinary Analysis and Design (MAD) Center at Virginia Tech in their work on the Blended-Wing-Body with distributed propulsion. During the two years I have worked for him, Dr. Schetz has given me much direction and helped me to see how to glean insight from both successes and apparent failures.

I also thank the other members of my graduate committee, Dr. Mason and Dr. Grossman. In the past, I worked under Dr. Mason's guidance during my senior aircraft design project. Dr. Mason often seemed to respond to our questions with even more questions, but he was trying to help us discover the answers for ourselves. Dr. Grossman's insight has been equally helpful. I thank each for their time and support.

I also acknowledge the other members of the BWB Distributed Propulsion group. I am especially thankful for Andy Ko and Serhat Hosder and for all their help and support. I spent many hours picking their minds. I am also thankful for the insight of Dr. Haftka, who helped me not get lost in the details or lose sight of the "big picture." I am honored to have worked with some of the best.

I also recognize the people at NASA Langley for their support, especially William M. Kimmel. Without NASA's financial support, this work would not have been possible.

I wish to also recognize my family. My parents have always been there to love and support me. The teaching and encouragement they have given me throughout the years has given me a great foundation for me to build. They have given me more than I could have ever expected. I am also thankful for my younger brother, Sam, who is beginning his graduate studies in Ocean Engineering at Virginia Tech. His presence in Blacksburg has been a real encouragement to me through the past few years. I'd also like to thank my little sister, Laurie. She's the greatest, and I always look forward to refreshing phone calls with her.

I would also like to acknowledge several of my friends. Owen Lofthus and Andy Goldfinger have been there as "sounding boards." I thank Kevin Rainey for challenging me to be adventurous, and I thank Jeremiah Lewis for teaching me all I know about

roller hockey. I also thank Mike Swann for giving me the opportunity to serve and grow with New Life Campus Fellowship. I also recognize my friends and former suitemates, Matthew Christopher, Timothy Fescue, and Michael Kheir - they are the rest the "Hawaiian shirt crew."

I am also very thankful for Mill Mountain Coffee Shop. Like so many others, I also wrote much of my thesis in their relaxing, laid-back dining room. Plus, they make some great Italian sodas and "Snow Monkey Plum" iced tea.

Finally, I thank my Lord and Redeemer, the Messiah Jesus. He has given me value that words alone cannot express. I give this work for the glory of his name.

Table of Contents

Acknowledgements.....	iv
Table of Contents	vi
List of Figures.....	viii
List of Tables	xiii
Nomenclature	xv
Chapter 1. Introduction.....	1
Chapter 2. Background and Literature Review	5
2.1. Jet-Wing and Jet-Flap Work	5
2.2. Distributed Propulsion and Propulsive Efficiency	8
2.3. Definition of Distributed Propulsion Approach.....	10
Chapter 3. Method and Model.....	12
3.1. Model Flow Conditions	12
3.2. Representative Wing Sections	13
3.2.1. MSES Flow Solver.....	16
3.2.2. Airfoil Development	16
3.2.3. Expanding the Trailing Edge	22
3.3. Modeling Distributed Propulsion Using ANSYS Flotran	24
3.3.1. ANSYS Flotran.....	24
3.3.2. The ANSYS Embedded Region and Transition to the Jet-Wing.....	27
3.3.2.1. Approximation of the Jet-Wing’s Effect Using a Virtual Flap.....	29
3.3.2.2. Embedded Region Boundary Conditions	30
3.3.2.3. Embedded Region Grid Modeling	35
3.3.2.4. Solving the Flow in the Embedded Region.....	37
3.4. Modeling the Jet-Wing with GASP	39
3.4.1. Grid Generation	39
3.4.1.1. Outboard 1xTE Airfoil	40
3.4.1.1.1. Low Reynolds Number Outboard 1xTE Airfoil Cases	43
3.4.1.2. Outboard 2xTE Airfoil	44
3.4.1.3. Inboard Airfoil	45
3.4.2. GASP Modeling Parameters	46
3.4.2.1. Defining Surfaces on Computational Domain	46

3.4.2.2.	Grid Sequencing and Levels	47
3.4.2.2.1.	Special Hybrid Grid for the Inboard Airfoil.....	47
3.4.2.3.	Specifying Freestream Properties.....	53
3.4.2.4.	Specifying Jet Flow Properties	54
3.4.2.5.	Boundary Conditions	55
3.4.2.6.	Inviscid, Viscous, and Thermo-Chemistry Models.....	56
3.4.2.7.	Run Settings.....	56
3.4.2.8.	Post Processing.....	58
3.4.3.	Calculating Force Coefficients	59
Chapter 4.	Computational Results.....	62
4.1.	Jet-Wing Studies for BWB at Cruise	62
4.1.1.	Outboard 1xTE Jet-Wing Airfoil Results.....	64
4.1.2.	Outboard 2xTE No-Jet Airfoil Results	67
4.1.3.	Outboard 2xTE Jet-Wing Airfoil Results.....	71
4.1.4.	Inboard No-Jet Airfoil Results	75
4.1.5.	Inboard Jet-Wing Airfoil Results	78
4.2.	Jet-Wing Studies for Low Reynolds Number Vehicles.....	84
4.2.1.	Outboard 1xTE No-Jet Airfoil Results at Low Reynolds Number	85
4.2.2.	Outboard 1xTE Jet-Wing Airfoil Results at Low Reynolds Number	86
4.2.3.	Outboard 1xTE Airfoil Jet-Flap Studies at Low Reynolds Number	88
Chapter 5.	Conclusions	93
5.1.	Recommended Further Studies:.....	94
References		96
Appendix A.	Tabulated Airfoil Coordinates.....	100
A.1.	Outboard 1xTE Airfoil Coordinates	100
A.2.	Outboard 2xTE Airfoil Coordinates	104
A.3.	Inboard Airfoil Coordinates	108
Appendix B.	MSES Flowfield Data Extraction.....	112
Vita		117

List of Figures

Figure 1.1: A Blended-Wing-Body aircraft [9].....	1
Figure 1.2: Distributed propulsion with many engines applied to a conventional transport aircraft [10].	2
Figure 1.3: Planform of distributed propulsion with several engines applied to BWB [12].	3
Figure 2.1: Kuchemann's jet-wing aircraft concept [13].....	6
Figure 2.2: Ball-Bartoe JW-1 jet-wing aircraft [20].....	7
Figure 2.3: A typical velocity profile behind a body and engine [12].	9
Figure 2.4: The velocity profile of a perfect distributed propulsion body/engine system [12].	10
Figure 2.5: The velocity profile of a realistic distributed propulsion body/engine system [12].	10
Figure 2.6: Hybrid distributed propulsion approach, using jet-wing and high-bypass-ratio turbofan propulsion [12].....	11
Figure 2.7: Hybrid distributed propulsion approach at a wing section without turbofan engine, where only jet-wing propulsion is present (figure adapted from [12]).....	11
Figure 3.1: Planform of BWB concept [3]. Arrows (added) show locations of representative airfoils.....	14
Figure 3.2: Pressure distribution of outboard wing section from Boeing BWB [3].	15
Figure 3.3: Pressure distribution of inboard wing section from Boeing BWB [3].	15
Figure 3.4: NASA SC(2)-0710 Supercritical airfoil [26].....	17
Figure 3.5: NASA SC(2)-0410 Supercritical airfoil [26].....	17
Figure 3.6: Pressure distribution of original SC(2)-410 airfoil.....	18
Figure 3.7: Pressure distribution of SC(2)-0410 airfoil, with "wiggles" removed.	18
Figure 3.8: Pressure distribution of SC(2)-0410 airfoil with cubic bumps.	19
Figure 3.9: Pressure distribution of "Outboard" airfoil: SC(2)-0410 airfoil with cubic bumps and stretched lower surface.	20
Figure 3.10: "Outboard" airfoil geometry	21
Figure 3.11: Comparison of "Outboard" airfoil geometries.	21
Figure 3.12: "Inboard" airfoil geometry	22

Figure 3.13: MSES pressure distribution of Inboard airfoil at $C_L = 0.30$	22
Figure 3.14: Comparison of "Outboard" airfoil geometries (y-axis distorted to pronounce expanded TE).	23
Figure 3.15: Comparison of "Outboard" airfoil geometries (close-up view).....	24
Figure 3.16: Two-dimensional distributed propulsion concept using a ducted propulsor.	24
Figure 3.17: ANSYS Flotran pressure distribution for NACA=0012 airfoil in subsonic flow. Experimental data is from [34].....	25
Figure 3.18: ANSYS Flotran pressure distribution for NACA=0012 airfoil in Mach 0.50 flow. Experimental data is from [34].....	25
Figure 3.19: ANSYS Flotran pressure distribution for NACA=0012 airfoil in transonic flow. Experimental data is from [34].....	26
Figure 3.20: ANSYS Flotran y^+ values for first grid point on NACA 65(3)-018 airfoil. ...	27
Figure 3.21: Embedded region approach used in ANSYS Flotran.	28
Figure 3.22: Embedded region approach with jet-wing.....	29
Figure 3.23: Boundary Layer velocity vector orientations.....	32
Figure 3.24: Embedded region Inlet boundary condition: x-component of velocity.	33
Figure 3.25: Embedded region Inlet boundary condition: y-component of velocity.....	34
Figure 3.26: Embedded region Inlet boundary condition: pressure.....	34
Figure 3.27: Embedded region Outlet boundary condition: pressure.	35
Figure 3.28: Initial sizing of Embedded region.	36
Figure 3.29: Initial ANSYS Flotran Embedded region grid.	37
Figure 3.30: Embedded region pressure distribution.....	38
Figure 3.31: Embedded region pressure distribution for velocity, pressure, and total temperature inlet boundary conditions at various region sizes.	38
Figure 3.32: Embedded region pressure distribution for velocity and total temperature inlet boundary conditions at various region sizes.	39
Figure 3.33: General airfoil grid geometry and nomenclature.....	41
Figure 3.34: First grid point y^+ values for Outboard 1xTE no-jet airfoil.	42
Figure 3.35: 2-zone grid of Outboard 1xTE airfoil (computational region).....	42
Figure 3.36: 2-zone grid of Outboard 1xTE airfoil (airfoil).....	43
Figure 3.37: 2-zone grid of Outboard 1xTE airfoil (trailing edge).	43

Figure 3.38: 2-zone grid of Outboard 2xTE airfoil (trailing edge).	45
Figure 3.39: 2-zone grid of Inboard airfoil (airfoil).	46
Figure 3.40: GASP surface definitions.	47
Figure 3.41: Inboard no-jet airfoil GASP grid convergence history.	49
Figure 3.42: Inboard no-jet airfoil GASP first grid point y^+ value on Medium grid.	49
Figure 3.43: Inboard no-jet airfoil GASP pressure distribution on Medium grid.	50
Figure 3.44: Inboard no-jet airfoil GASP skin friction on Medium grid.	50
Figure 3.45: Inboard airfoil "Hybrid" grid.	51
Figure 3.46: Inboard no-jet airfoil GASP grid convergence history using Hybrid grid.	51
Figure 3.47: Inboard no-jet airfoil GASP first grid point y^+ value on Hybrid grid.	52
Figure 3.48: Inboard no-jet airfoil GASP pressure distribution on Hybrid and Medium grids.	52
Figure 3.49: Inboard no-jet airfoil GASP skin friction on Hybrid and Medium grids.	53
Figure 3.50: Fine grid convergence typical of outboard airfoils.	58
Figure 3.51: Orientation of jet-wing in GASP.	59
Figure 4.1: Comparison of GASP and MSES pressure distributions for Outboard 1xTE airfoil at $\alpha = 2.66^\circ$.	63
Figure 4.2: Comparison of GASP and MSES pressure distributions for Outboard 1xTE airfoil at $C_L = 0.628$.	63
Figure 4.3: Outboard 1xTE no-jet and jet-wing airfoil pressure distributions for $C_{L_{Net}} = 0.628$.	65
Figure 4.4: Velocity profile downstream of Outboard 1xTE no-jet and jet-wing airfoils, $x/c=1.01$.	66
Figure 4.5: Streamlines and Mach number contours at trailing edge of Outboard 1xTE no-jet airfoil.	66
Figure 4.6: Streamlines and Mach number contours at trailing edge of Outboard 1xTE jet-wing airfoil.	67
Figure 4.7: Pressure contours at the trailing edge of the Outboard 1xTE jet-wing airfoil.	67
Figure 4.8: Outboard 1xTE and Outboard 2xTE no-jet airfoil pressure distributions for $C_{L_{Net}} = 0.628$.	68

Figure 4.9: Streamlines and Mach number contours at trailing edge of Outboard 2xTE no-jet airfoil.....	69
Figure 4.10: Comparison of GASP pressure distribution on trailing edge base of Outboard 1xTE and 2xTE no-jet airfoils.	71
Figure 4.11: Velocity profile downstream of Outboard 1xTE and Outboard 2xTE no-jet airfoils.....	71
Figure 4.12: Outboard 2xTE no-jet and jet-wing airfoil pressure distributions for $C_{L_{Net}} = 0.628$	73
Figure 4.13: Velocity profile downstream of Outboard 2xTE no-jet and jet-wing airfoils.	73
Figure 4.14: Velocity profile downstream of Outboard 1xTE and Outboard 2xTE jet-wing airfoils.....	74
Figure 4.15: Streamlines and Mach number contours at trailing edge of Outboard 2xTE jet-wing airfoil.	74
Figure 4.16: Pressure contours at the trailing edge of the Outboard 2xTE jet-wing airfoil.	75
Figure 4.17: Inboard no-jet airfoil convergence history using Hybrid Grid.	76
Figure 4.18: Inboard no-jet airfoil GASP "peak" and "valley" and MSES solutions of pressure distributions.	77
Figure 4.19: Inboard no-jet airfoil GASP "peak" and "valley" and MSES solutions of upper surface skin friction.....	77
Figure 4.20: Streamlines and Mach number contours around Inboard no-jet airfoil.	78
Figure 4.21: Streamlines and Mach number contours near trailing edge of Inboard no-jet airfoil. Note region of separated flow.....	78
Figure 4.22: Inboard jet-wing airfoil GASP grid convergence history.....	81
Figure 4.23: Inboard no-jet and jet-wing airfoil GASP pressure distributions.	81
Figure 4.24: Inboard no-jet and jet-wing airfoil GASP upper surface skin friction.....	82
Figure 4.25: Streamlines and Mach number contours around Inboard jet-wing airfoil... ..	82
Figure 4.26: Streamlines and Mach number contours near trailing edge of Inboard jet-wing airfoil. Note region of separated flow.....	83
Figure 4.27: Pressure contours at the trailing edge of Inboard jet-wing airfoil.	83
Figure 4.28: Velocity profile downstream Inboard no-jet and jet-wing airfoils.....	84

Figure 4.29: Comparison of GASP pressure distribution for Outboard 1xTE no-jet airfoil at design and low Reynolds numbers.	85
Figure 4.30: Outboard 1xTE no-jet and jet-wing airfoil pressure distribution at low Reynolds number.....	87
Figure 4.31: Velocity profile downstream of Outboard 1xTE no-jet and jet-wing airfoils at low Reynolds number.....	87
Figure 4.32: Velocity profile downstream of Outboard jet-wing airfoils at design and low Reynolds numbers.....	88
Figure 4.33: Trends in lift, drag, pitching moment with jet deflection angle constant angle of attack and low Reynolds number.....	89
Figure 4.34: Comparison of GASP pressure distributions for Outboard 1xTE jet-wing/-flap airfoil at constant angle of attack and low Reynolds number.....	90
Figure 4.35: Comparison of GASP pressure distribution near the trailing edge of the Outboard 1xTE jet-wing/-flap airfoils at low Reynolds number.....	91
Figure 4.36: Streamlines and Mach number contours at trailing edge of Outboard 1xTE jet-wing/-flap airfoils at Low Reynolds number.....	91
Figure 4.37: Pressure contours at trailing edge of Outboard jet-flap airfoils at Low Reynolds number.....	92

List of Tables

Table 3.1: Freestream properties for BWB at cruise.....	13
Table 3.2: Outboard airfoil three-dimensional and two-dimensional characteristics.....	17
Table 3.3: Outboard airfoil cubic bump parameters.....	19
Table 3.4: Inboard airfoil three-dimensional and two-dimensional characteristics.....	21
Table 3.5: Inboard airfoil cubic bump parameters.....	22
Table 3.6: ANSYS Flotran validation tests with NACA-0012 airfoil.	25
Table 3.7: ANSYS Flotran grid y^+ value requirements.....	26
Table 3.8: Virginia Tech Boundary Layer applet parameters for Outboard 1xTE airfoil upper surface.....	31
Table 3.9: Outboard 1xTE airfoil grid spacings (see Figure 3.33).	41
Table 3.10: Outboard 1xTE airfoil Gridgen extrusion smoothing parameters for Airfoil zone.....	42
Table 3.11: Low Reynolds number Outboard 1xTE airfoil grid spacings (see Figure 3.33).	44
Table 3.12: Low Reynolds number Outboard 1xTE airfoil Gridgen extrusion smoothing parameters for Airfoil zone.	44
Table 3.13: Inboard airfoil grid spacings (see Figure 3.33).	45
Table 3.14: Inboard airfoil Gridgen extrusion smoothing parameters for Airfoil zone....	45
Table 3.15: GASP freestream properties for representative airfoil models.	54
Table 3.16: GASP jet flow properties for representative jet-wing airfoil models.	55
Table 4.1: Outboard 1xTE no-jet and jet-wing airfoil results for $C_{L_{Net}} = 0.628$	65
Table 4.2: Outboard 1xTE and Outboard 2xTE no-jet airfoil results for $C_{L_{Net}} = 0.628$	68
Table 4.3: Outboard 1xTE and Outboard 2xTE no-jet airfoil drag breakdown.	70
Table 4.4: Outboard 2xTE no-jet and jet-wing airfoil results for $C_{L_{Net}} = 0.628$	72
Table 4.5: Inboard no-jet airfoil results.....	77
Table 4.6: Inboard no-jet and first iteration jet-wing airfoil results.....	80
Table 4.7: Inboard no-jet and (final) jet-wing airfoil results.	80
Table 4.8: Outboard 1xTE no-jet airfoil results for design and lower Reynolds numbers	85
Table 4.9: Outboard 1xTE no-jet and jet-wing airfoil results for $Re_c = 5.67e6$	86

Table 4.10: Outboard 1xTE jet-wing and jet-flap airfoil results for $Re_c = 5.67e6$	89
Table B.1: Flowfield quantities from MSES.....	113

Nomenclature

BL	Boundary Layer
BWB	Blended-Wing-Body
CFD	Computational Fluid Dynamics
MDO	Multidisciplinary Optimization
NASA	National Aeronautics and Space Administration
NACA	National Advisory Council for Aeronautics
TE	Trailing Edge
a	Speed of sound
a_∞	Freestream speed of sound
a_{jet}	Jet flow speed of sound
b	Wing span
b_{jet}	Span of jet-wing
c	Chord length
c_{2D}	Chord length for two-dimensional analysis
C_D	Drag coefficient
$C_{D_{net}}$	Net drag coefficient, includes jet thrust
$C_{D_{local}}$	Local drag coefficient, with respect to span
C_J	Jet thrust coefficient
C_L	Lift coefficient
$C_{L_{net}}$	Net lift coefficient, includes jet thrust
$C_{L_{2D}}$	Lift coefficient for two-dimensional analysis
C_p	Pressure coefficient
D	Drag
D_{local}	Local drag, with respect to span
D_{Net}	Net drag, includes jet thrust
\vec{F}	Generic force vector; specify using pressure, viscous, momentum flux
Fx_{Inv}	Inviscid force in x-direction

Fx_Total	Total force in x-direction, not including momentum flux forces
Fx_Vis	Viscous force in x-direction
Fy_Inv	Inviscid force in y-direction
Fy_Total	Total force in y-direction, not including momentum flux forces
Fy_Vis	Viscous force in y-direction
h_{jet}	Jet height
\hat{i}, \hat{j}	Unit vectors in x- and y-directions
L	Lift
L_{Net}	Net lift, includes jet thrust
m	Jet flow mass
M	Local flow Mach number
M_∞	Freestream Mach number
M_{jet}	Jet flow Mach number
M_{2D}	Mach number for two-dimensional analysis
Mz_Inv	Moment about quarter chord from inviscid forces
Mz_Thrust	Total moment about quarter chord, includes momentum flux forces
Mz_Total	Moment about quarter chord from inviscid and viscous forces
Mz_Vis	Moment about quarter chord from viscous forces
p	Pressure
p_∞	Freestream pressure
p_{jet}	Jet flow pressure
$p_{TE_{upper}}$	Pressure at upper surface trailing edge
$p_{TE_{lower}}$	Pressure at lower surface trailing edge
Q	The set of variables defined in GASP used to specify the flow conditions: temperature, pressure, density, velocity, laminar and turbulent viscosities, and Mach number.
Q_∞	In GASP, the set of flow parameters specifying the freestream conditions.
Q_{local}	In GASP, the set of flow parameters specifying conditions at an individual cell.

q	Dynamic pressure
R	Gas constant
Re	Reynolds number
Re_c	Chord Reynolds number
Re_{trans}	Transition Reynolds number
S, S_{ref}	Jet reference area
$Surf$	Airfoil surface not including trailing edge
$\frac{t}{c}$	Thickness ratio
$\left(\frac{t}{c}\right)_{2D}$	Thickness ratio for two-dimensional analysis
$T, Thrust_{jet}$	Jet thrust
T_{jet}	Temperature of jet flow
T_∞	Temperature of freestream
T_0	Total, or stagnation, temperature
$Thrust_{GASP}$	Thrust force from GASP, not including jet inflow
$Thrust_x$	Total force in x-direction, including momentum flux forces
$Thrust_y$	Total force in y-direction, including momentum flux forces
u, v, w	Velocity magnitude in the x-, y-, and z-directions
u_{BL}, v_{BL}	Velocity magnitude in the x-, y-directions aligned with boundary layer
U	Velocity magnitude
U_∞	Freestream velocity magnitude
U_{jet}	Jet velocity magnitude
U_e	Boundary layer edge velocity magnitude
$\hat{U}_x, \hat{U}_y, \hat{U}_z$	Component of velocity unit vector in x-, y-, and z-directions
x, y, z	Coordinates
y^+	Transverse coordinate for law of the wall
α	Airfoil angle of attack
β	Ratio of jet velocity to freestream velocity
δ	Boundary layer thickness

δ_{ini}	Initial boundary layer thickness
δ_{TE}	Boundary layer thickness at trailing edge
γ	Ratio of specific heats
η_P	Froude propulsive efficiency
$\Lambda_{\frac{1}{4}}$	Quarter-chord sweep
μ	Dynamic viscosity
μ_∞	Freestream dynamic viscosity
μ_{lam}	Laminar dynamic viscosity
μ_{vis}	Viscous dynamic viscosity
θ	Local airfoil surface slope
ρ	Density
ρ_∞	Freestream density
ρ_{jet}	Jet flow density
ρ_{scaled}	Density scaled for Reynolds number
τ	Jet deflection angle
ν	Kinematic viscosity

Chapter 1. Introduction

The air transportation industry continues to grow in the world today: more passengers, more flights, and busier airports and skies. In an effort to meet these ever-growing needs, NASA and Boeing have developed the Blended-Wing-Body (BWB) aircraft concept ([1], [2], [3], [4], [5]). As the name implies, the BWB (pictured in Figure 1.1) blends together the wings and the passenger cabin into one, highly-integrated structure. To accomplish this requires synergy between all the major systems: aerodynamics, controls, structures, propulsion, payload, etc. This synergistic approach has been shown to improve performance: reduce fuel burn, take-off weight, empty weight, and required thrust; and increase the lift-to-drag ratio [1], [2], [3], [4], [5]. A BWB aircraft concept is highly integrated and requires Multidisciplinary Optimization (MDO) [6], [7], [8] to develop a feasible BWB design. The MDO code will find a BWB design that not only meets various performance and mission constraints, but that is also optimized with respect to one or more design objectives, such as take-off gross weight or noise.

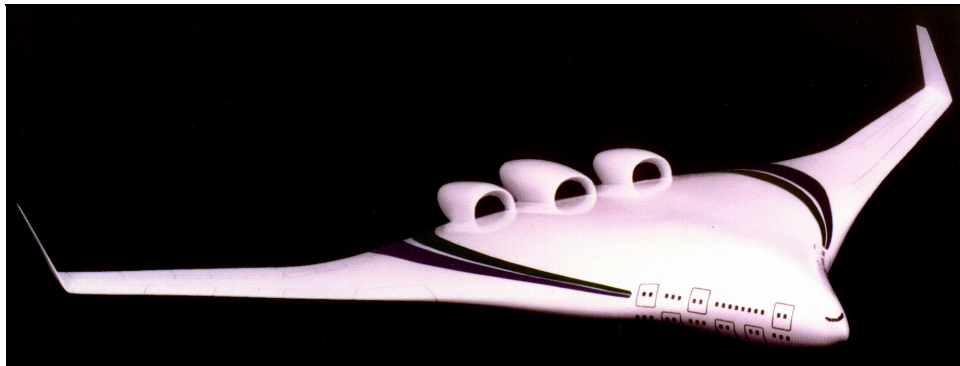


Figure 1.1: A Blended-Wing-Body aircraft [9].

Two priorities in the airline industry today are to reduce emissions and reduce noise [10], [11]. Distributed propulsion has been suggested to meet these goals.

Distributed propulsion is the idea of distributing a fixed-wing aircraft's thrust power over all or part of the span of the aircraft. As shown in Figure 1.2 and Figure 1.3, distributed propulsion can be accomplished with a few or many engines. While distributed propulsion was originally suggested as a way to reduce noise [10], it offers a number of other potential benefits as well. Distributed propulsion offers potentially greater safety in the form of engine redundancy: with numerous engines, a failed engine will not as critically impact an aircraft's thrust and control performance as with a conventional aircraft. Also, through load redistribution by distributing many smaller engines across the span of the wings, distributed propulsion can potentially reduce gust load/flutter problems and provide passive load alleviation resulting in reduced wing weight. Distributed propulsion can also improve affordability by using smaller, easily interchangeable engines. In addition to these potential benefits, one of the major advantages of distributed propulsion is that it is a synergistic integration of the propulsion system with the airframe. In nature, the integration of propulsion and lift systems is readily evident: birds' and insects' wings produce both thrust and lift. Lastly, the "jet-wing," one distributed propulsion configuration, was proposed by Kuchemann¹ as a way to increase propulsive efficiency [13].

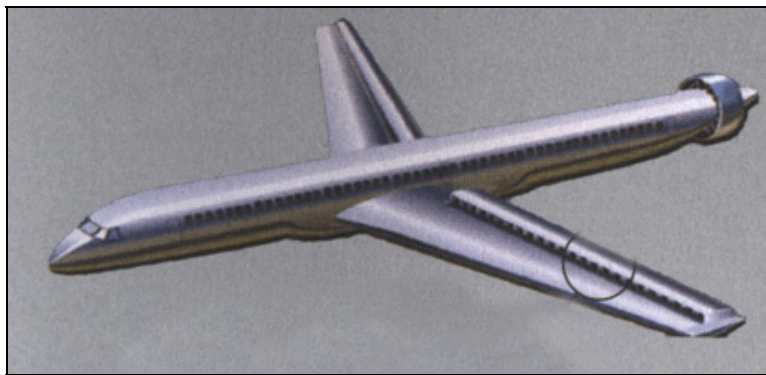


Figure 1.2: Distributed propulsion with many engines applied to a conventional transport aircraft [10].

¹ The original reference to Kuchemann's introduction of the jet-wing concept has been cited as: "On the Possibility of Connecting the Production of Lift with that of Propulsion," *M.A.P. Volkenrode, Reports and Translations* No. 941-1 Nov., 1947, APPENDIX I, Kuchemann, D., "The Jet Wing." However, a copy of this reference could not be obtained.

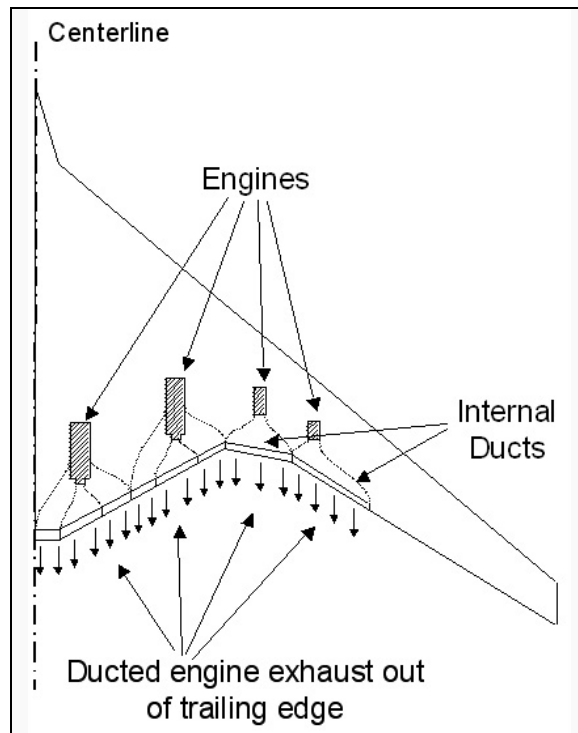


Figure 1.3: Planform of distributed propulsion with several engines applied to BWB [12].

With a little thought, one can see a common thread amongst distributed propulsion and the BWB: both require a high level of integration between their subsequent components. Therefore, distributed propulsion could be applied to the BWB concept. While models suitable for MDO have been developed for the BWB with conventional propulsion systems [6], [7], [8], new models had to be developed for the integration of distributed propulsion [12]. Numerical studies in viscous compressible flow are desired to help validate the performance gains of Ko's jet-wing distributed propulsion model and to provide higher-fidelity response surfaces for the MDO code.

This thesis discusses computational fluid dynamics (CFD) studies performed with several two-dimensional jet-wing distributed propulsion models. While CFD tests were run using only two-dimensional airfoil models, these models were representative of the airfoil sections found on the BWB aircraft. The goals of this study were to ascertain the effect of jet-wing distributed propulsion on propulsive efficiency and to observe how jet-wing distributed propulsion affects the flowfield around the airfoil. The structure of this work is as follows:

- Chapter 2 discusses previous work with jet-flap and jet-wing systems and reviews propulsive efficiency as applied to distributed propulsion.

- Chapter 3 explains the development of jet-wing distributed propulsion models for CFD studies.
- Chapter 4 presents the results from the parametric CFD studies.
- Chapter 5 discusses what conclusions can be made from the studies and suggests directions for future studies.

Chapter 2. Background and Literature Review

2.1. *Jet-Wing and Jet-Flap Work*

The jet-wing and jet-flap are two similar ideas. Both blow a jet out from the wing, either at or near the trailing edge. In some configurations, the jet is blown over part of the airfoil. The jet-flap differs from the jet-wing simply by employing a layer of exhaust flow and by deflecting the jet as if it were a flap on the trailing edge of an airfoil. The jet-flap is typically associated with high-lift applications, while the jet-wing is associated with vehicle cruise conditions. While the focus of this work is on the jet-wing, the histories of both, the jet-wing and the jet-flap, must be examined because they are so similar.

The jet-wing is not a new idea. Kuchemann suggested the jet-wing as early in 1938 as a way to improve propulsive efficiency [13]. Kuchemann's jet-wing aircraft concept, shown in Figure 2.1, would bury the engines in the wing and use turbojet engines with non-annular cold-air bypass ducts. While duct losses would be inevitable, Kuchemann suggested that the jet-wing would still be more efficient than the conventional Cayley-type arrangement with isolated engines [14]. While the jet-wing seems favorable, apparently Kuchemann did not perform any detailed analysis to assess the possible benefits.

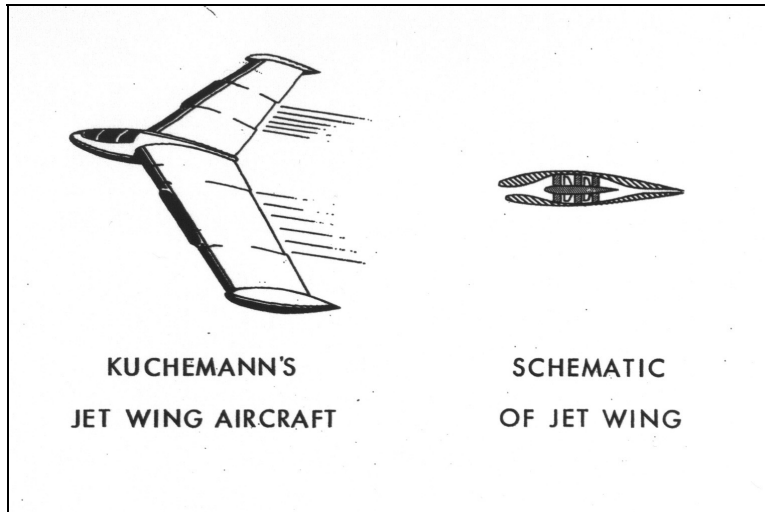


Figure 2.1: Kuchemann's jet-wing aircraft concept [13].

At about the same time Kuchemann proposed the jet-wing, Hagendorn and Ruden conducted low-speed wing tunnel tests of a jet-flap configuration [15]. The model consisted of an airfoil with a trailing edge jet blown from a thin slot over a flap. This work concentrated on high-lift applications, with a lift coefficient of $C_L \approx 6$.

Later, Spence derived an analytical solution for a thin two-dimensional airfoil with a thin trailing edge jet [16]. This solution was developed for inviscid, incompressible flow, using thin-airfoil theory. While Spence's jet-flap theory was valid only for small jet deflection angles, it still had high lift applications and used large jet coefficient values, $C_J > 1$, where C_J is defined in Equation (2.1) below:

$$C_J = \frac{m \cdot U_{jet}}{\frac{1}{2} \cdot \rho_{\infty} \cdot U_{\infty}^2 \cdot S} \quad (2.1)$$

where U_{jet} = Jet flow velocity

U_{∞} = Freestream velocity

m = Jet flow mass

S = Jet reference area

ρ_{∞} = Freestream density

Spence's jet-flap theory compared well with experimental data.

Ives and Melnik [17] developed a numerical solution for jet-flapped airfoils. Based on a finite differencing scheme, Ives and Melnik's solution could analyze jet-flaps in inviscid, transonic flow. This work also focused on high-lift applications and used

small to moderate jet coefficients. Ives and Melnik used their method to analyze a jet-flap on a supercritical airfoil with thick trailing edge.

Transonic jet-flap experiments were performed by Yoshihara and Zonars [18]. With shocks present in their experiments, Yoshihara and Zonars were able to reexamine the “thrust recovery” observed on jet-flaps in low-speed flows. Using high jet deflection angles and low jet coefficient values of $C_j = 0.02$, their work found that, while the jet-flap increased lift, it increased drag and nose-down pitching moment. Tests were also conducted on three-dimensional wings, and it was found that wing-fuselage junctions reduced the beneficial jet-flap effects.

Kimberlin [19], [20] discusses experimental flight tests performed on the Ball-Bartoe JW-1 jet-wing aircraft [21]. The JW-1, pictured in Figure 2.2, incorporated a slotted jet on the upper surface of the wing with an ejector and was designed for high-lift, short-take-off purposes. Kimberlin found that the ejector gave poor performance.

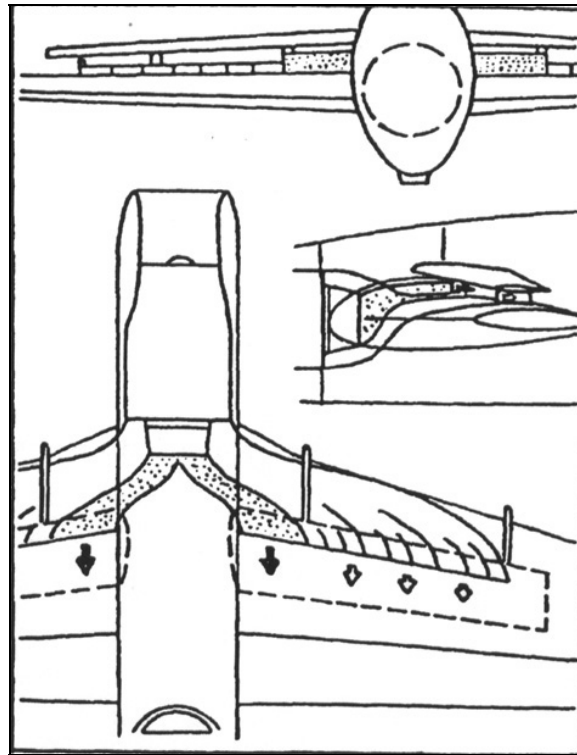


Figure 2.2: Ball-Bartoe JW-1 jet-wing aircraft [20].

Spence’s jet-flap theory was extended by Ko [12], [24] and incorporated into a jet-wing distributed propulsion model for MDO. Ko extended Spence’s theory by including the effects of sweep. Jet-flap thrust vectoring was used as a means for aircraft control, instead of ailerons and other moving surfaces. Ko showed that jet-wing

distributed propulsion applied to a BWB aircraft can reduce the take-off gross weight (TOGW) over a BWB with a conventional propulsion system.

2.2. Distributed Propulsion and Propulsive Efficiency

Kuchemann suggested that the jet-wing configuration would improve propulsive efficiency when he introduced the concept in 1938 [13]. However, literature has provided no detailed assessment of this proposal. The propulsive efficiency is improved because a jet exiting out the trailing edge of the wing ‘fills in’ the wake directly behind the wing. Naval architects had been implementing this concept for years on ships and submarines by installing a single propeller directly behind a streamlined axisymmetric body (neglecting the ‘sail’ and control surfaces). This configuration tends to maximize the propulsive efficiency of the ship-propeller system, even through the wake is typically not perfectly filled [21]. Similar improvements in propulsive efficiency are potentially attainable with the proposed jet-wing distributed propulsion system.

The Froude Propulsive Efficiency, η_P , is defined as the ratio of useful power out of the propulsor to the rate of kinetic energy added to the flow by the propulsor, as shown in Equation (2.2) [22].

$$\eta_P = \frac{T \cdot U_\infty}{q \cdot S_{ref} \cdot U_\infty \cdot \beta \cdot (\beta - 1)} \quad (2.2)$$

where T = Thrust

U_∞ = Freestream velocity

S_{ref} = Reference area

q = Dynamic pressure

β = Ratio of engine jet velocity to freestream velocity

Equation (2.2) can be reduced to the form of propulsive efficiency given in Equation (2.3), where U_{jet} is the jet velocity.

$$\eta_P = \frac{2}{\frac{U_{jet}}{U_\infty} + 1} \quad (2.3)$$

Ko considers a simple analysis of a two-dimensional, non-lifting, self-propelled vehicle with an engine [12], shown in Figure 2.3. In this arrangement, the wake of the body is independent of the jet from the engine. Furthermore, the vehicle is defined as self-propelled, meaning that the thrust of the engine must exactly balance the drag

associated with the velocity deficit due to the wake of the body. Propulsive efficiency loss is a consequence of any net kinetic energy left in the wake (characterized by non-uniformities in the velocity profile) compared to that of a uniform velocity profile. For a typical high-bypass-ratio turbofan at Mach 0.85, the Froude Propulsive Efficiency is about 80% [23].

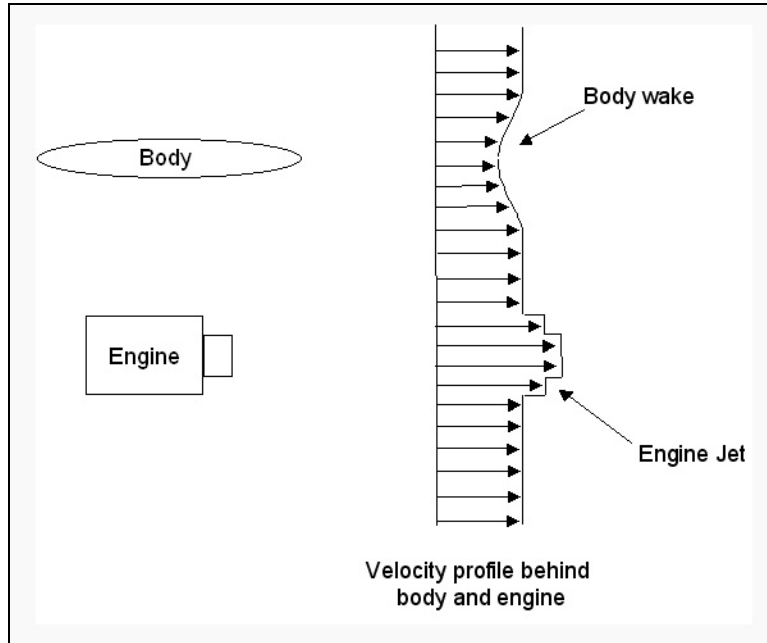


Figure 2.3: A typical velocity profile behind a body and engine [12].

Next, Ko considered the distributed propulsion system shown in Figure 2.4, in which the jet and the wake of the body are combined. In the ideal system, the jet perfectly ‘fills in’ the wake, creating a uniform velocity profile. In this case, the kinetic energy added to the flow by the jet compared to that of a uniform velocity profile is zero, and the propulsive efficiency is $\eta_p = 100\%$. However, the jet does not fully ‘fill in’ the wake in practice, but creates smaller non-uniformities in the velocity profile, as illustrated in Figure 2.5. But, the resulting velocity profile contains a smaller net kinetic energy than that of the case where the body and engine are independent shown in Figure 2.3. The efficiency of a distributed propulsion system will be bounded by the efficiency of the body/engine configuration (nominally 80%) and the perfect distributed propulsion configuration of 100%. Ko, Schetz, and Mason [24] present an analysis of the propulsive efficiency of a distributed propulsion system of this type. It is necessary to note, however, that the effect of the jet on the overall pressure distribution of the body

was not included in this simplified analysis. It is expected that the jet will entrain the flow over the surface of the body and increase drag.

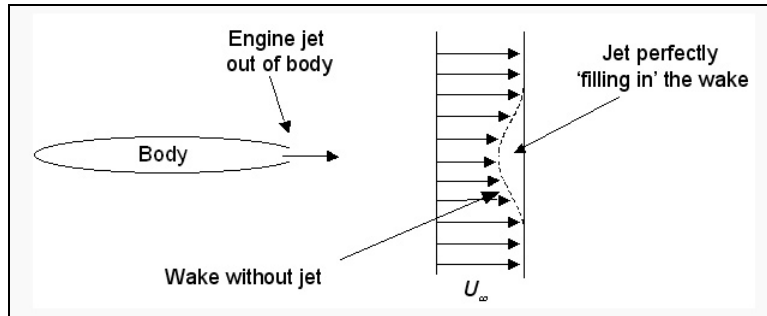


Figure 2.4: The velocity profile of a perfect distributed propulsion body/engine system [12].

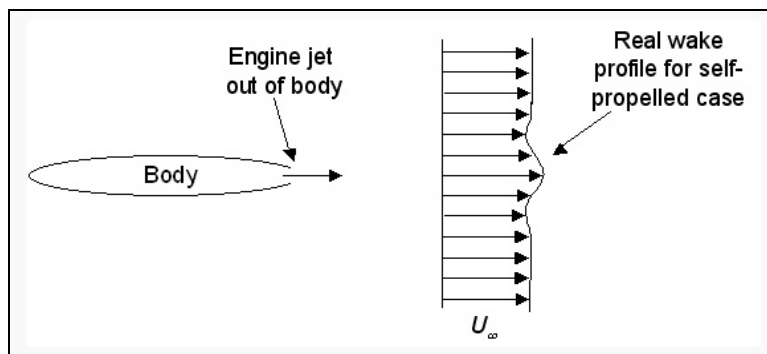


Figure 2.5: The velocity profile of a realistic distributed propulsion body/engine system [12].

2.3. Definition of Distributed Propulsion Approach

This research endeavor was part of a larger project with the goals of reducing emissions and noise of a BWB aircraft by applying distributed propulsion. The distributed propulsion design used in this project is a hybrid approach, illustrated in Figure 2.6, that uses high-bypass-ratio turbofan engines with some of the exhaust ducted through a jet-wing. The jet-wing system uses thrust from the cold fan exhaust of the high-bypass-ratio turbofan engines to overcome the drag due to viscous and pressure forces, while the rest of the thrust of the turbofan overcomes the induced drag. This thesis will discuss the performance of only the jet-wing portion of this combined distributed propulsion system, illustrated in Figure 2.7. As a reference baseline for propulsive efficiency performance, the propulsive efficiency given by Hill and Peterson [23] of $\eta_p = 80\%$ will be used. However, it must be understood that $\eta_p = 80\%$ is being used simply as a reference since there is no propulsion system to use for a direct comparison to the jet-wing. Also, the propulsive efficiencies computed in this thesis are only for the jet-wing portion of this hybrid distributed propulsion system. The actual

propulsive efficiency of the entire distributed propulsion system will likely be different. Lastly, it should be understood that $\eta_p = 80\%$ is typical of only the most efficient high-bypass-ratio turbofan engines. If the jet-wing propulsion system has a propulsive efficiency even slightly greater than 80%, than it performs better than most modern propulsion systems.

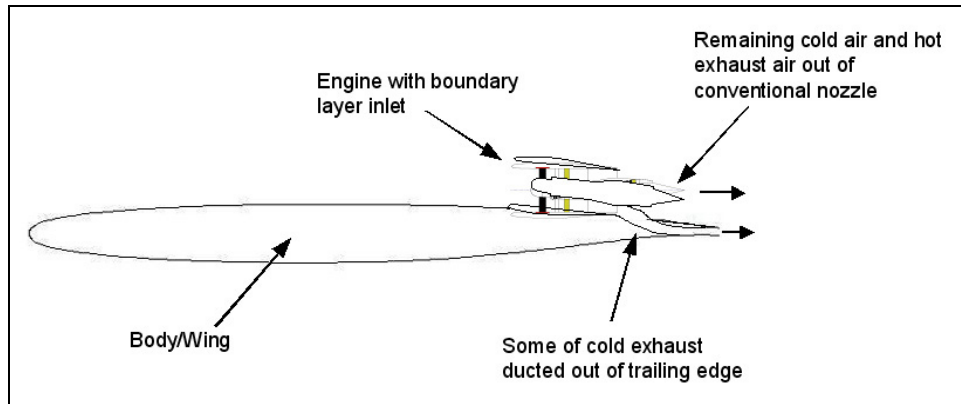


Figure 2.6: Hybrid distributed propulsion approach, using jet-wing and high-bypass-ratio turbofan propulsion [12].

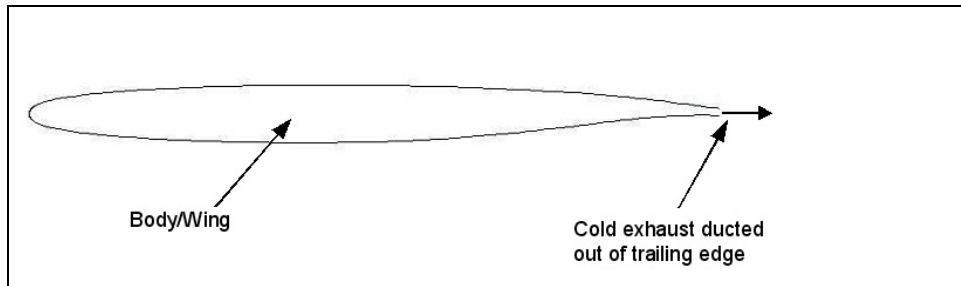


Figure 2.7: Hybrid distributed propulsion approach at a wing section without turbofan engine, where only jet-wing propulsion is present (figure adapted from [12]).

Chapter 3. Method and Model

As this CFD investigation of distributed propulsion began, several questions needed to be answered:

- What does the distributed propulsion system look like?
- How do we model this distributed propulsion system?
- On what type of wing or airfoil do we model the distributed propulsion system?
- What flow conditions should the CFD model simulate?

Literature repeatedly showed two concepts for distributed propulsion: the jet-wing, as shown in Figure 2.1 and applying small engines to the upper surface of the wings, either in nacelles or ducts, as illustrated in Figure 1.2. Because the more recent artists' conceptions showed distributed propulsion as many engines on the upper surface of the wing, that concept was initially selected. However, as will be further explained, a jet-wing configuration was later chosen and analyzed.

The 1996 Boeing BWB configuration control document [3] served to help answer the third and fourth questions. The report was selected as a reference in the airfoil model development, because it provided many details regarding the aerodynamics of the BWB.

3.1. Model Flow Conditions

A primary goal of this study was to investigate how distributed propulsion affects the propulsive efficiency and aerodynamic performance of a BWB-type aircraft. According to the Boeing report [3], the BWB was designed for a range of 7,000 nmi, so it will therefore spend most of its flight time at cruise conditions. The cruise conditions (Mach 0.85 at an altitude of 35,000 ft) were chosen as the flow conditions of this research

endeavor. Using a U.S. Standard Atmosphere table [25], and converting to SI units, the flow conditions were calculated and are presented in Table 3.1.

Table 3.1: Freestream properties for BWB at cruise.

Freestream Mach number, M_∞	0.85
Freestream temperature, T_∞	218.9 K
Freestream pressure, p_∞	23919 N/m²
Freestream density, ρ_∞	0.3807 kg/m³
Freestream speed of sound, a_∞	296.6 m/s
Freestream dynamic viscosity, μ_∞	1.435e-5 N·s/m²
Freestream velocity, u_∞	218.9 m/s
Reynolds number per meter chord length, Re/c	5.67e+6

3.2. Representative Wing Sections

In an effort to simplify the task of performing a CFD analysis of a BWB with distributed propulsion, it was determined that computations should first be performed on representative two-dimensional wing section models. As mentioned earlier, no previous numerical or experimental studies regarding distributed propulsion were found in the literature. A two-dimensional model would allow making a number of computations in the endeavor to understand distributed propulsion and to validate analytical models. Using the planform given in the 1996 Boeing BWB report [3], two span locations were chosen for representative airfoil sections: an outboard section at 62% of the span and an inboard section at 22% of the span. The BWB planform and span sections are shown in Figure 3.1. The wing section chord lengths are 7.99 m at the outboard station and 28.09 m at the inboard station.

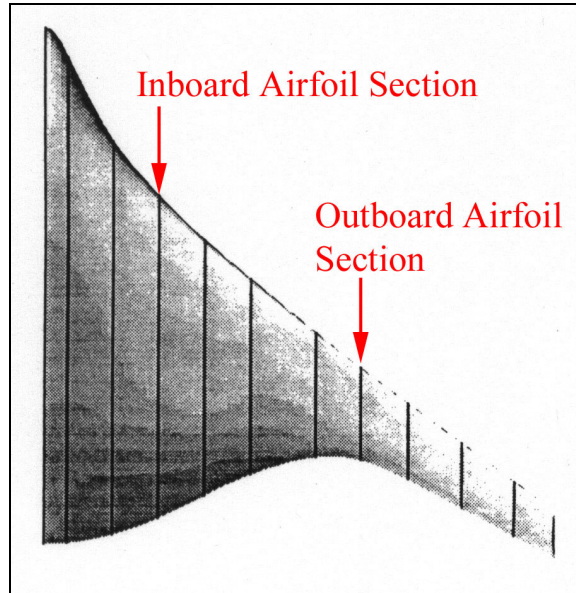


Figure 3.1: Planform of BWB concept [3]. Arrows (added) show locations of representative airfoils.

The outboard span station was chosen because it resembles the wing of a conventional transport aircraft in thickness ($\frac{t}{c} = 10\%$), quarter-chord sweep ($\Lambda_{\frac{1}{4}} = 32^\circ$), and lift coefficient ($C_L = 0.50$). The pressure distribution on this airfoil section is shown in Figure 3.2. It was also thought that this outboard span station would not see highly three-dimensional flows. So, while the outboard section was still representative of part of the BWB, the results would be expected to be similar to what would be found on conventional transport aircraft wings with distributed propulsion. The inboard airfoil section has a much larger thickness ($\frac{t}{c} = 18\%$), slightly higher quarter-chord sweep ($\Lambda_{\frac{1}{4}} = 35^\circ$), lower lift coefficient ($C_L = 0.22$), and the pressure distribution shown in Figure 3.3. This span section was chosen to investigate how the distributed propulsion impacts the flow around, and performance of, thicker wing sections, as found inboard on the BWB.

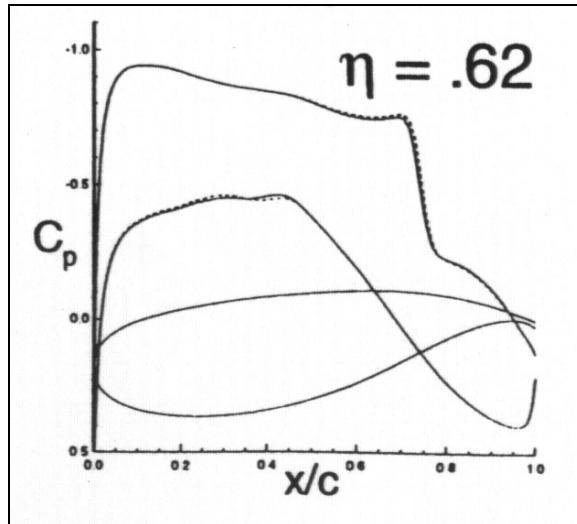


Figure 3.2: Pressure distribution of outboard wing section from Boeing BWB [3].

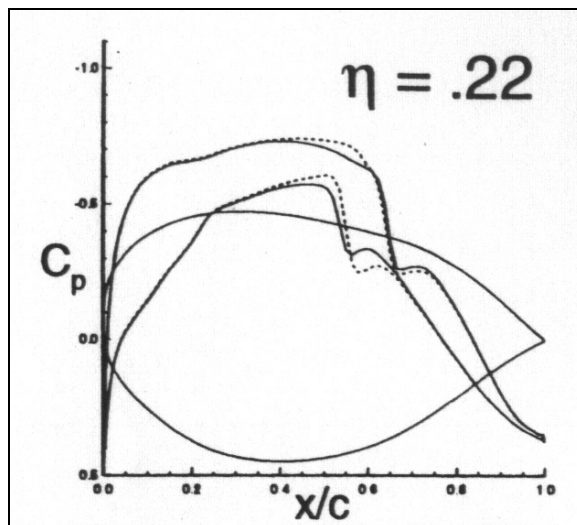


Figure 3.3: Pressure distribution of inboard wing section from Boeing BWB [3].

The 1996 Boeing BWB report [3] shows that the airfoils used are of an advanced cambered design, with shocks typically occurring on the latter half of the airfoil. These airfoils look very similar to the NASA supercritical airfoils presented by Harris [26], in both shape and pressure distribution. Therefore, our representative airfoils are based on NASA supercritical airfoils.

The NASA supercritical airfoil family is characterized with a blunt nose, a thick trailing edge, a pressure “plateau” before the shock, and some aft camber. When compared to airfoils with closed trailing edges, the presence of the thick trailing edge on the supercritical airfoils results in a significant reduction in wave drag at transonic Mach numbers. The thick trailing edge does cause a recirculation region downstream which

produces a base drag on the trailing edge face, but the trailing edge base drag is more than offset by the decreased wave drag at transonic Mach numbers [26]. As will be later discussed, the typical thickness of these thick trailing edges is about 0.7% of the chord, which permits a jet-wing to be easily incorporated into supercritical airfoils.

3.2.1. MSES Flow Solver

The multi-element airfoil analysis code MSES [27], [28] was used to assist in the development of representative BWB airfoils. MSES couples a finite-volume method to solve the steady Euler equations on an “intrinsic streamline grid” in the inviscid region with an integral boundary layer method in the viscous region [28]. Of significance to our purposes, MSES can solve transonic flows with shocks and flows with some separation. MSES can also predict turbulent transition. Ko, et al. [29], found MSES to be useful and accurate in similar airfoil design work. The MSES code reads in the airfoil geometry and a list of parameters including freestream Mach number, Reynolds number, and several grid parameters. MSES can solve a flow for a specified angle of attack or a specified lift coefficient. In a matter of minutes on an SGI workstation, MSES can compute a solution to an airfoil flow problem. MSES outputs the lift and drag coefficients, the resulting angle of attack or lift coefficient, the surface pressure distribution, boundary layer quantities, and flowfield quantities. The very low run-time cost made MSES appealing in the selection of the representative airfoil models.

3.2.2. Airfoil Development

Beginning with the representative outboard airfoil – hereafter referred to as “Outboard” airfoil – an airfoil of similar thickness and lift coefficient to the Boeing BWB was selected from the NASA supercritical airfoil family [26]. The outboard section has a chord length of 7.99 m, a thickness of 10%, a lift coefficient of 0.50, and a quarter-chord sweep of 32°. Using Equation (3.1), two-dimensional airfoil characteristics corresponding to this section of a three-dimensional wing were found.

$$\begin{aligned}
 c_{2D} &= c \cdot \cos\left(\Lambda_{\frac{1}{4}}\right) \\
 M_{2D} &= M_{\infty} \cdot \cos\left(\Lambda_{\frac{1}{4}}\right) \\
 C_{L_{2D}} &= \frac{C_L}{\left(\cos\left(\Lambda_{\frac{1}{4}}\right)\right)^2} \\
 \left(\frac{t}{c}\right)_{2D} &= \frac{\left(\frac{t}{c}\right)_{streamwise}}{\cos\left(\Lambda_{\frac{1}{4}}\right)}
 \end{aligned} \tag{3.1}$$

For the Outboard airfoil, the results are shown in Table 3.2. Comparing the characteristics required by the Outboard airfoil with the NASA supercritical airfoils, it became clear that two airfoils could possibly work: the SC(2)-0710 airfoil and the SC(2)-0410 airfoil. These two airfoils are shown in Figure 3.4 and Figure 3.5, respectively. Both of these airfoils have a thickness of 10%, and a design Mach number near 0.72. While the SC(2)-0710 has a design lift coefficient of 0.7 and may look like the better candidate, it also has a high amount of aft camber, resulting in a larger pitching moment. More recent BWB designs show reduced aft-loading on wing sections than the previous designs [30], [31]. Therefore, the SC(2)-0410 airfoil, which has a design lift coefficient of 0.4 and less aft camber (and consequentially a smaller pitching moment), was favored, but it would require modifications to increase its lift performance and further reduce its aft loading.

Table 3.2: Outboard airfoil three-dimensional and two-dimensional characteristics.

	3-D	2-D
$\frac{1}{4}$ -chord sweep, $\Lambda_{\frac{1}{4}}$	32°	--
Chord, c	7.99 m	6.77 m
Thickness, $\frac{t}{c}$	8.6%	10%
Lift Coefficient, C_L	0.50	0.69
Freestream Mach number, M_∞	0.85	0.72

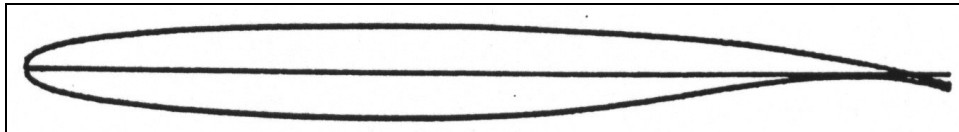


Figure 3.4: NASA SC(2)-0710 Supercritical airfoil [26].

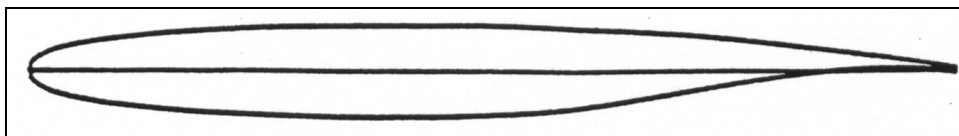


Figure 3.5: NASA SC(2)-0410 Supercritical airfoil [26].

Figure 3.6 shows the pressure distribution predicted with MSES of the SC(2)-0410 airfoil at Mach 0.72, a Reynolds number of 38.4 million, and a lift coefficient of 0.72. The pressure distribution is characterized by “wiggles,” as documented by Ko [29]. The first modification of the airfoil was to eliminate those coordinates from Harris [26] causing the “wiggles.” The pressure distribution of an improved coordinate set is shown in Figure 3.7. Note that most of the “wiggles” in the pressure distribution have been removed.

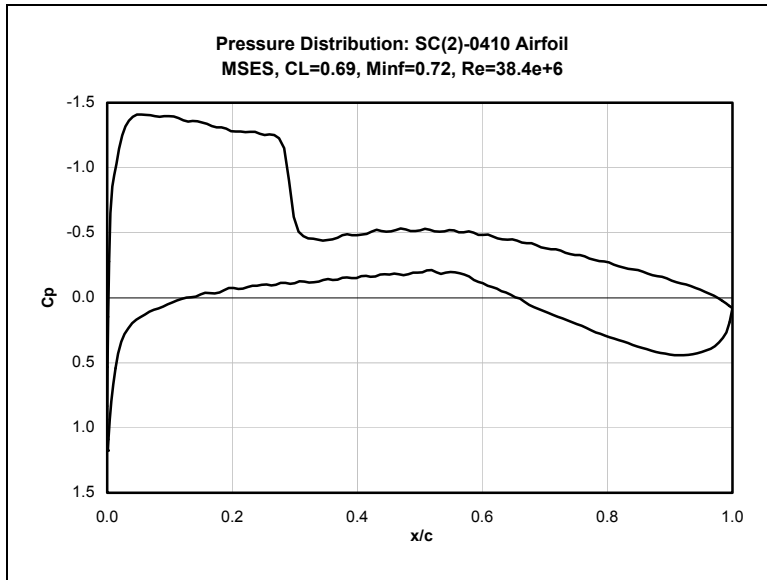


Figure 3.6: Pressure distribution of original SC(2)-410 airfoil.

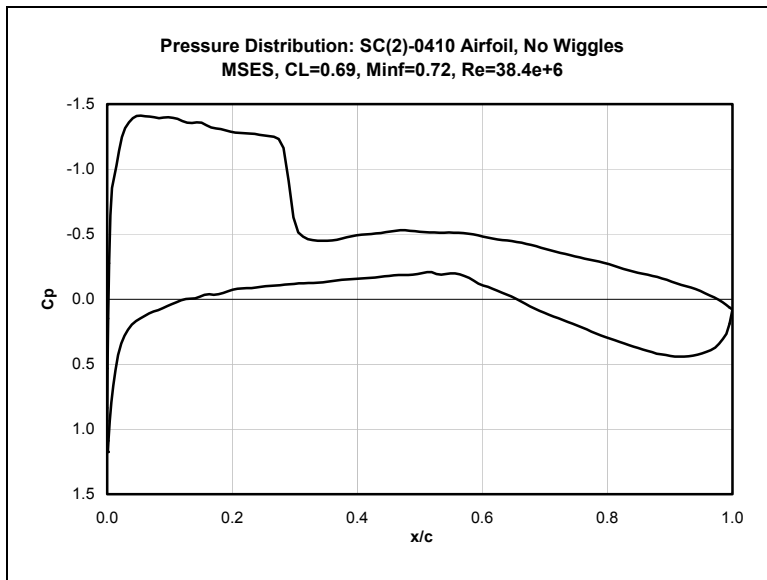


Figure 3.7: Pressure distribution of SC(2)-0410 airfoil, with “wiggles” removed.

The next issue that was addressed was to adapt the airfoil for our selected conditions. It was necessary to make modifications to change two characteristics of the SC(2)-0410 airfoil’s pressure distribution. First, the shock was rather strong and could result in a large wave drag. Therefore, a reduction of the shock strength was desired. Second, recent BWB studies suggest that reduced aft-loading is favored over previous designs [30], [31]. One way to reduce the effect of the pitching moment is to decrease the aft-loading of the airfoil. Similar changes in an airfoil’s pressure distribution were made by Ko [29] by adding and subtracting cubic bumps to and from the airfoil using a

cubic bump algorithm [32]. A “cubic bump” is a small bump applied to a region of the airfoil that maintains the slope and curvature of the airfoil at the endpoints of the bump. The airfoil designer can choose the height of the bump (positive or negative), the length of the bump, and the location of the maximum height. A cubic bump was added to the upper surface of the SC(2)-0410 airfoil to weaken the shock and move it aft. Another cubic bump was added to the aft portion of the lower surface in an attempt to reduce the aft-loading caused by the aft camber. The parameters for the two cubic bumps that were used are given in Table 3.3. The pressure distribution resulting from the addition of cubic bumps is shown in Figure 3.8.

Table 3.3: Outboard airfoil cubic bump parameters.

Bump Parameter	Upper Surface Bump	Lower Surface Bump
Location of bump beginning, x_1	0.000	0.550
Location of bump maximum thickness, x_2	0.380	0.900
Location of bump ending, x_3	1.000	1.050
Maximum thickness of bump, $\Delta\left(\frac{t}{c}\right)$	0.008	0.010
Length of body, x_{\max}	1.000	1.000

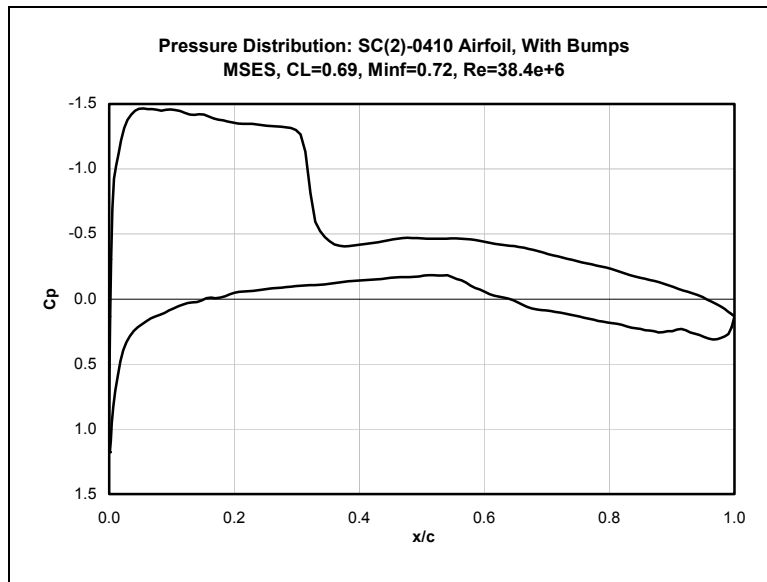


Figure 3.8: Pressure distribution of SC(2)-0410 airfoil with cubic bumps.

The result still did not reduce the aft-loading satisfactorily. This was because the cubic bump applied to the aft end of the lower surface maintained the slope at the trailing edge, thus it was not possible to further reduce the camber at the trailing edge. The next attempted modification made was to linearly stretch the lower surface of the airfoil. The last 5% of the lower surface of the airfoil was eliminated, and the remaining

95% of the lower surface was stretched in a linear fashion. In a constant stretching procedure, the original x -value of each coordinate is multiplied by approximately 105.3%. Analytically, constant stretching is shown in Equation (3.2) for a chord length of c and a truncation point x_t . In the linear stretching procedure as used here, the displacement in the x -direction of each point varies linearly from 0% at the leading edge to 105.3% at the trailing edge. Linear stretching is shown analytically in Equation (3.3). The resulting pressure distribution, after applying the cubic bumps and lower surface stretching, is compared with that of the original SC(2)-0410 airfoil in Figure 3.9. The final Outboard airfoil is illustrated in Figure 3.10 and compared with the SC(2)-0410 airfoil in Figure 3.11. The Outboard airfoil coordinates are listed in Appendix A.

$$x_{new} = \left(\frac{c}{x_t} \right) \cdot x; 0 \leq x \leq x_t \quad (3.2)$$

$$x_{new} = \left(c + \frac{x}{x_t} \right) \cdot x; 0 \leq x \leq x_t \quad (3.3)$$

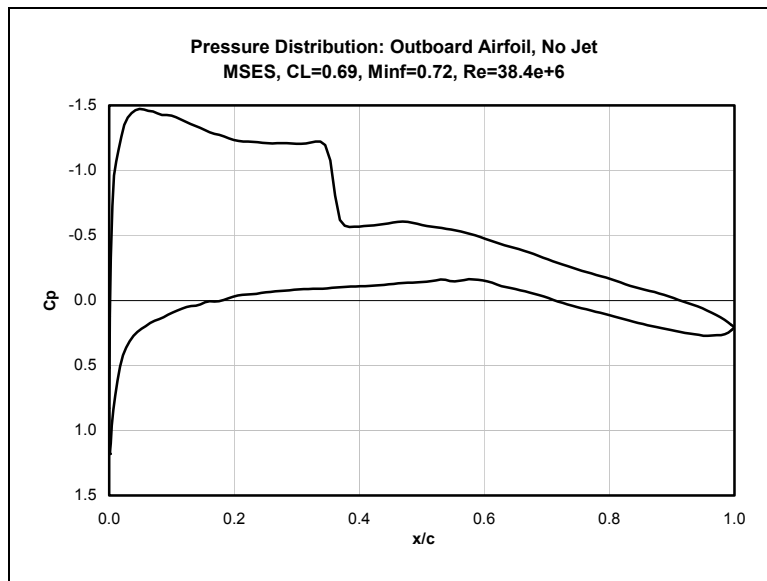


Figure 3.9: Pressure distribution of "Outboard" airfoil: SC(2)-0410 airfoil with cubic bumps and stretched lower surface.

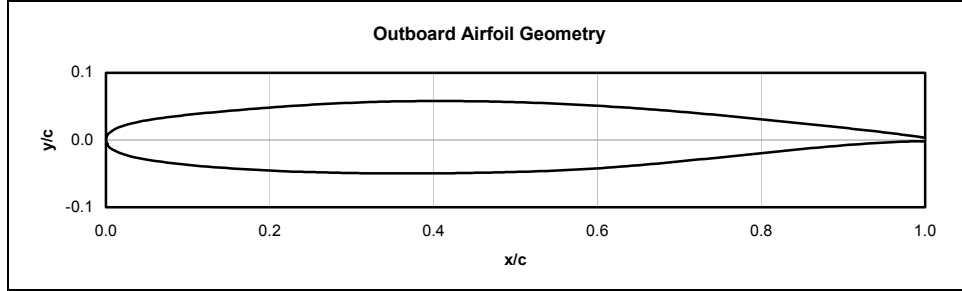


Figure 3.10: "Outboard" airfoil geometry

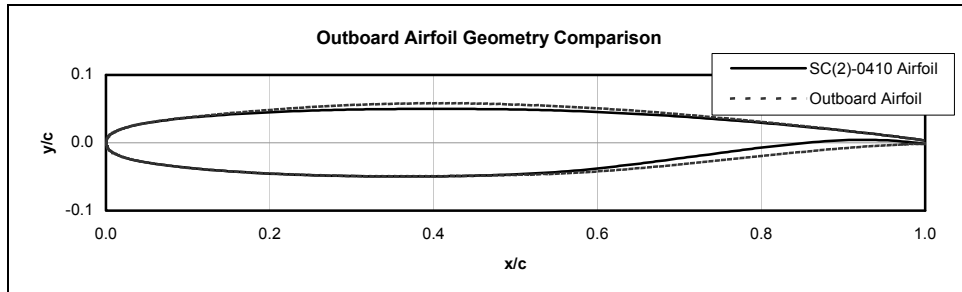


Figure 3.11: Comparison of "Outboard" airfoil geometries.

A similar process was applied to the Inboard airfoil. The two-dimensional airfoil results are given in Table 3.4. The Inboard airfoil was developed using *Foilgen* [33]. *Foilgen* creates an airfoil using the NACA 4-digit airfoil series equations and several parameters specified by the user. The airfoil used had a thickness of $\frac{t}{c}=18\%$, a maximum camber of 0.4%, and the maximum camber located at $\frac{x}{c}=6\%$. Cubic bumps were then added to this airfoil in order to make the pressure distribution of the Inboard airfoil approximate that of the inboard Boeing BWB wing section (see Figure 3.3). The cubic bump parameters are given in Table 3.5. Note that the slope was specified at the ending of the second lower surface bump. This was done so that the resulting airfoil more closely matched that of the Boeing report [3]. The final Inboard airfoil geometry is shown in Figure 3.12, its pressure distribution is shown in Figure 3.13, and its geometry is given in Appendix A.

Table 3.4: Inboard airfoil three-dimensional and two-dimensional characteristics

	3-D	2-D
$\frac{1}{4}$ -chord sweep, $\Lambda_{\frac{1}{4}}$	35°	--
Chord, c	28.09 m	23.01 m
Thickness, $\frac{t}{c}$	18%	18%
Lift Coefficient, C_L	0.22	0.30
Freestream Mach number, M_∞	0.85	0.75

Table 3.5: Inboard airfoil cubic bump parameters.

Bump Parameter	Upper Surface Bump	Lower Surface Bump 1	Lower Surface Bump 2
Location of bump beginning, x_1	0.000	0.000	0.600
Location of bump maximum thickness, x_2	0.075	0.001	1.000
Location of bump ending, x_3	0.500	0.500	1.000
Maximum thickness of bump, $\Delta\left(\frac{t}{c}\right)$	0.005	0.005	0.0005
Slope at end of bump, $\left(\frac{dy}{dx}\right)_3$	--	--	0.500
Length of body, x_{\max}	1.00	1.00	1.00

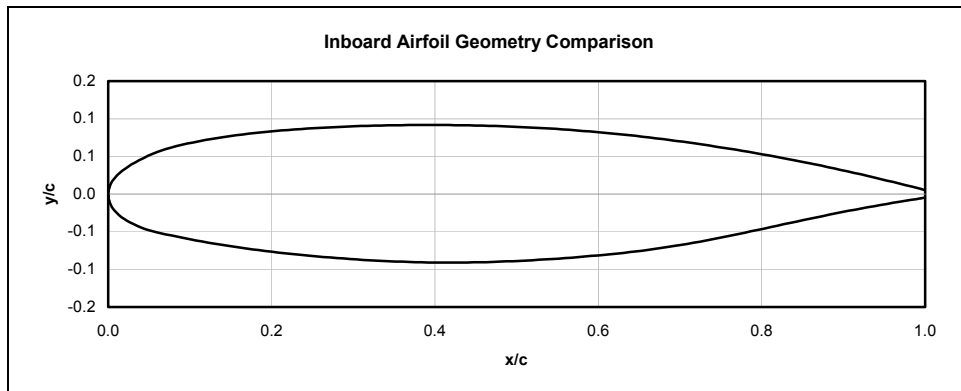


Figure 3.12: "Inboard" airfoil geometry

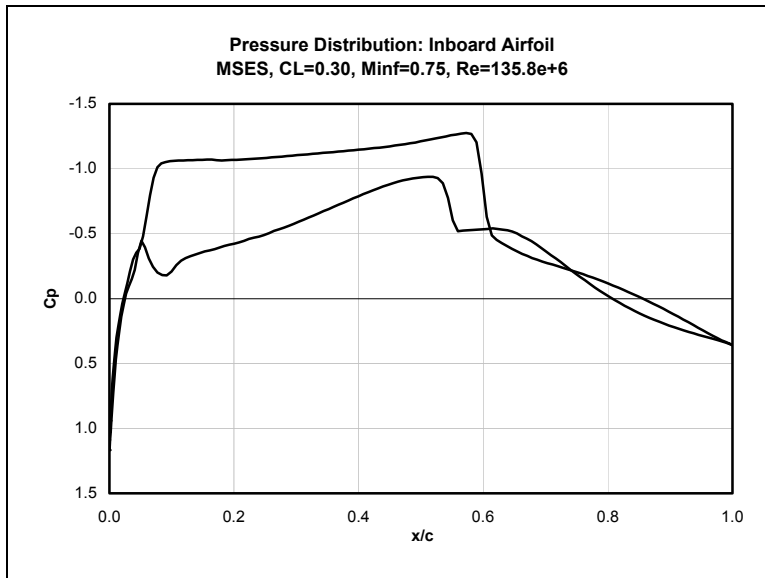


Figure 3.13: MSES pressure distribution of Inboard airfoil at $C_L = 0.30$.

3.2.3. Expanding the Trailing Edge

One more airfoil development technique was performed in this research pursuit, namely expanding the trailing edge of the airfoil. One of the goals of the jet-wing

distributed propulsion concept study is to increase the propulsive efficiency of the aircraft. As will be further discussed later, the propulsive efficiency of the baseline Outboard airfoil with the jet-wing applied was slightly lower than the 80% propulsive efficiency typical of turbofans [23]. By studying the simplified form of propulsive efficiency, Equation (2.3), it is observed that one can *increase* propulsive efficiency by *decreasing* the speed of the jet. When other properties are kept constant, if the jet speed is decreased, the jet area must be increased for an equal amount of thrust from the jet. Therefore, an attempt was made at decreasing the jet exit speed and increasing the exit area of the jet-wing. This was accomplished by expanding the height of the airfoil trailing edge. The method chosen to accomplish expanding the trailing edge was to truncate the airfoil at the location of desired trailing edge height and then linearly stretch the airfoil to the correct chord length. Again, the x -values of the airfoil coordinates are displaced according to Equation (3.3) for a specified chord length of c and truncation point x_t . This trailing edge expansion was performed on the Outboard airfoil, and it increased the trailing edge height to 0.98% of the chord (whereas the original TE height 0.49% of the chord). The modifications are shown in Figure 3.14 and Figure 3.15, and the coordinates are tabulated in Appendix A. The Outboard airfoil with the original trailing edge thickness is now referred to as the “Outboard 1xTE” airfoil, and the Outboard airfoil with the double thickness trailing edge is referred to as the “Outboard 2xTE” airfoil.

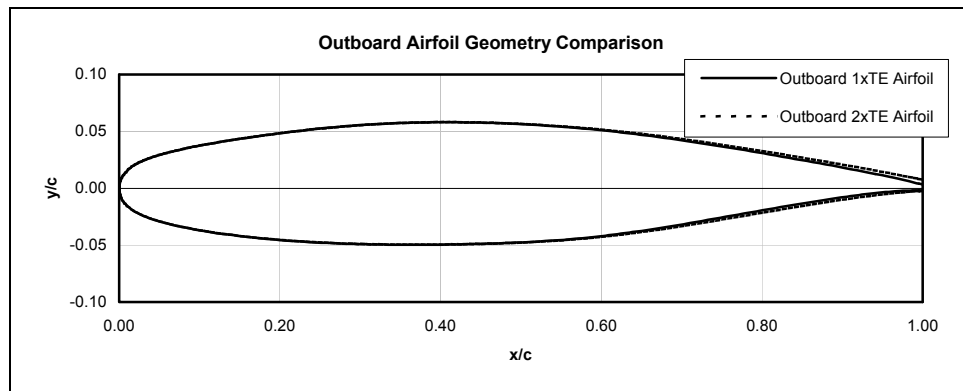


Figure 3.14: Comparison of "Outboard" airfoil geometries (y-axis distorted to pronounce expanded TE).

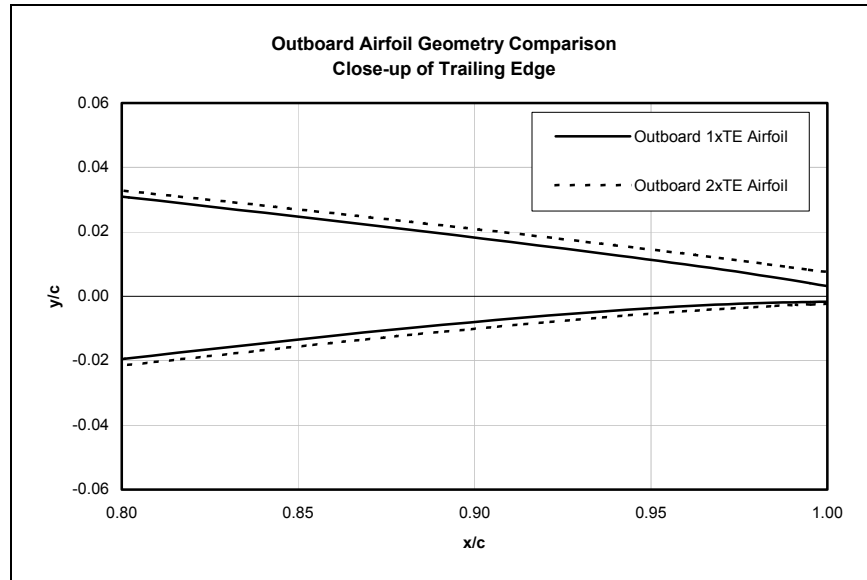


Figure 3.15: Comparison of "Outboard" airfoil geometries (close-up view).

3.3. Modeling Distributed Propulsion Using ANSYS Flotran

As previously mentioned, the initial distributed propulsion configuration was based from concepts showing distributed propulsion as many engines on the upper surface of the wing. Our two-dimensional model of distributed propulsion would apply a ducted propulsor to the upper surface of the airfoil, toward the trailing edge. This is illustrated in Figure 3.16. One challenge with this distributed propulsion concept is modeling the propulsor, but a CFD code was found with this capability: ANSYS Flotran.

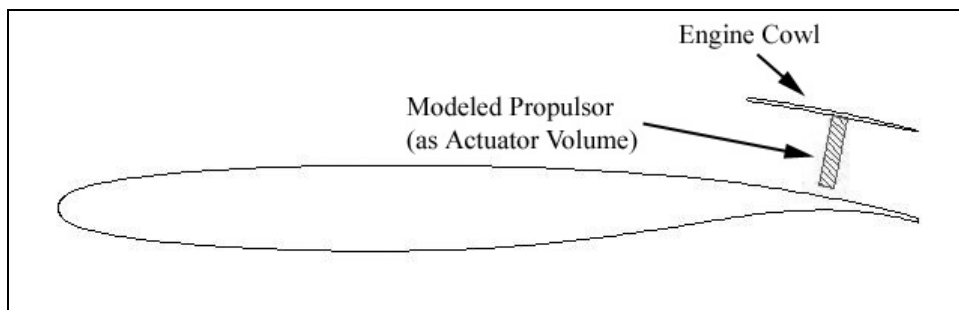


Figure 3.16: Two-dimensional distributed propulsion concept using a ducted propulsor.

3.3.1. ANSYS Flotran

ANSYS Flotran is a finite element Navier Stokes code, with the ability to model pumps and actuator disks (or volumes) as force fields. For this reason, ANSYS Flotran was selected to model our initial two-dimensional distributed propulsion system. Before constructing the distributed propulsion model in ANSYS Flotran, an NACA-0012 airfoil was run to validate results with experimental data [34]. Three runs were made at the flow conditions shown in Table 3.6. At the subsonic Mach number flows, the

ANSYS Flotran results agreed with the experimental results, as observed in Figure 3.17. However, as the flow Mach number was increased (see Figure 3.18), the ANSYS Flotran solution disagreed. In fact, at a transonic Mach number, ANSYS Flotran failed to predict the formation of a shock, which is shown in Figure 3.19. This problem caused concern.

Table 3.6: ANSYS Flotran validation tests with NACA-0012 airfoil.

Run	1	2	3
Freestream Mach number, M_∞	0.300	0.500	0.754
Angle of attack, α	-0.02°	-0.02°	2.98°
Reynolds number, Re	$1.40e+6$	$2.33e+6$	$3.52e+6$

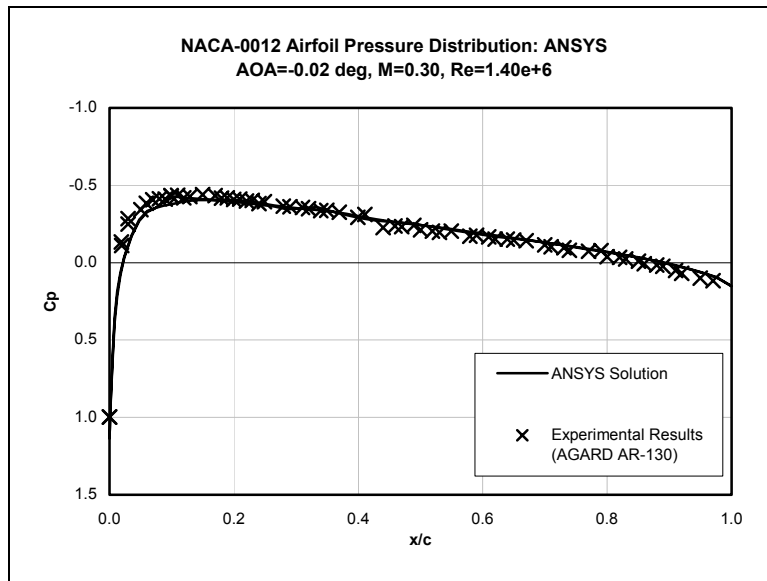


Figure 3.17: ANSYS Flotran pressure distribution for NACA=0012 airfoil in subsonic flow. Experimental data is from [34].

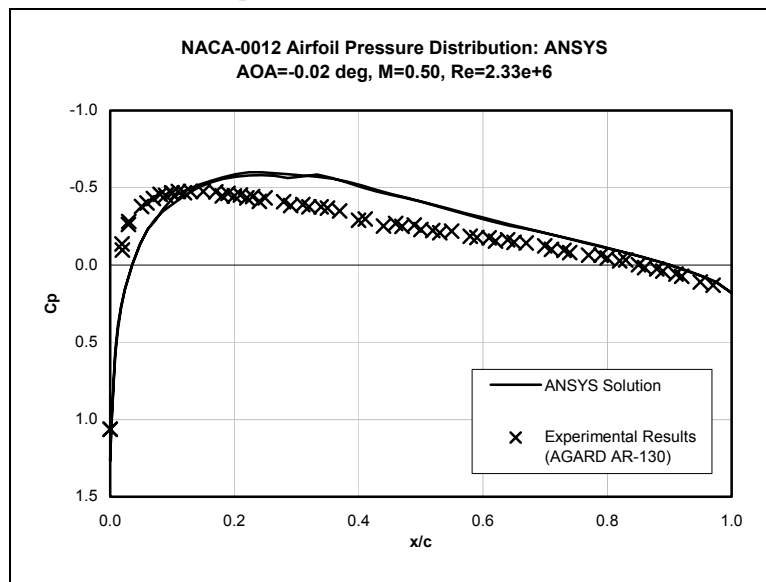


Figure 3.18: ANSYS Flotran pressure distribution for NACA=0012 airfoil in Mach 0.50 flow. Experimental data is from [34].

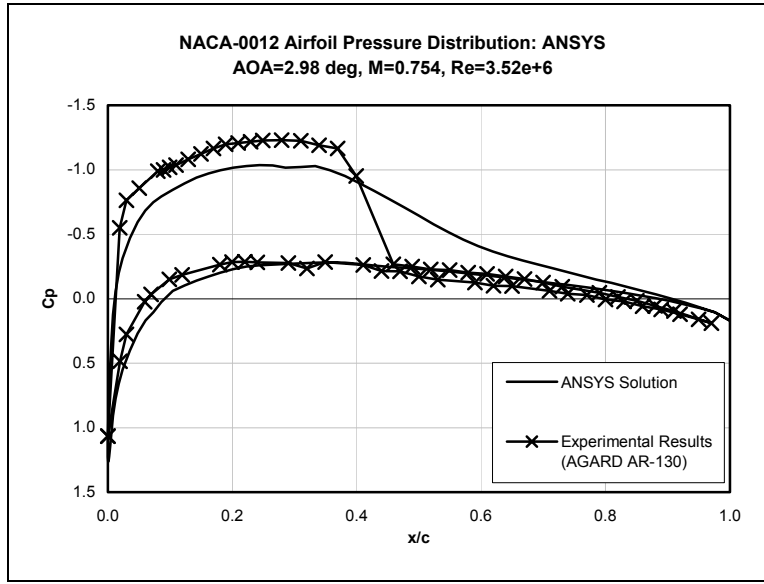


Figure 3.19: ANSYS Flotran pressure distribution for NACA=0012 airfoil in transonic flow. Experimental data is from [34].

A second problem arose while attempting to validate results from ANSYS Flotran. ANSYS Flotran uses wall functions in its modeling of the boundary layer over a surface, and the first and second grid points above the wall must lie within a specific range of y^+ values [35], [36]. The minimum and maximum y^+ values are given in Table 3.7. Therefore, to develop a feasible grid in ANSYS, one must know a good deal about the boundary layer in the flow. The boundary layer flow was solved using MSES and the Virginia Tech Boundary Layer Applets [37], and the results were used to size the first and second grid points on the ANSYS Flotran grid. Even after several iterations, satisfactory results were not obtained. Figure 3.20 shows the y^+ values of the first grid point across the surface of a NACA 65(3)-018 airfoil in a subsonic flow.

Table 3.7: ANSYS Flotran grid y^+ value requirements.

	Min. y^+ value	Max. y^+ value
First Grid Point	10	30
Second Grid Point	30	300

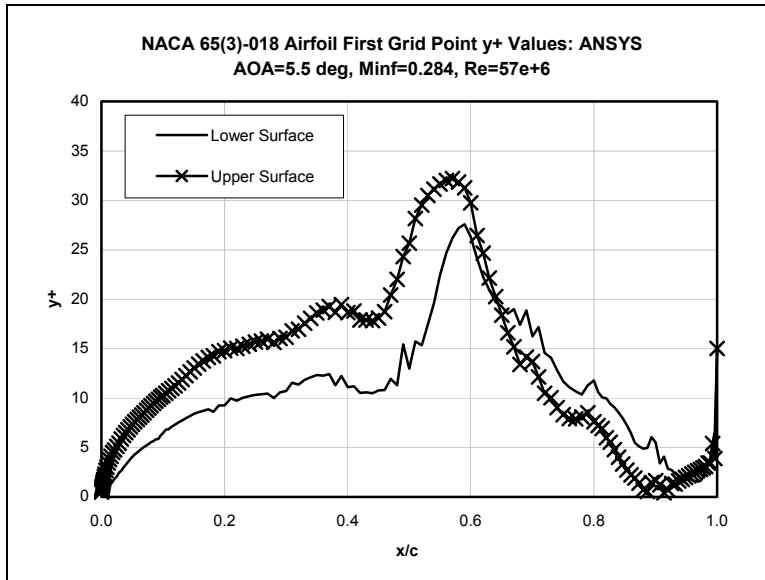


Figure 3.20: ANSYS Flotran y^+ values for first grid point on NACA 65(3)-018 airfoil.

To this point, ANSYS Flotran could not satisfactorily resolve the boundary layer or shock waves in a flow over an airfoil – and this was without the addition of the propulsor. Because we are modeling distributed propulsion at cruise, the ability to solve a flow at transonic Mach numbers (and properly predict shock waves) is absolutely necessary. Also, the goal to ‘fill in’ the wake requires that the CFD code be able to correctly resolve the boundary layer. It was concluded that an approach other than solving an airfoil flow in ANSYS Flotran needed to be considered.

3.3.2. The ANSYS Embedded Region and Transition to the Jet-Wing

A second approach using ANSYS Flotran was considered following MacLean [36] who showed success in using an ANSYS Flotran “Embedded” region. As illustrated in Figure 3.21, the flowfield around the airfoil was divided into two regions: an Upstream region, in which the full flowfield around the airfoil is solved and an Embedded region, which would be solved with ANSYS Flotran using the solution of the upstream region as inflow and boundary conditions. In the Upstream region, MSES would be used to solve the general airfoil flow, and the Virginia Tech Boundary Layer Applets [37] would be used to solve the boundary layer over the airfoil surface. These tools are proven and require only small computational costs relative to a full Navier-Stokes solution. It was assumed that the effect of the propulsor on airfoil pressure distribution would be small, and that the addition of a virtual flap to the airfoil could approximate these effects when solving in the Upstream region. (This virtual flap

approximation is explained in detail in 3.3.2.1 below.) The results in the Upstream region from MSES and the Boundary Layer Applets would then be used as boundary conditions to the Embedded region, which would be solved using ANSYS Flotran. The flap approximation in the Upstream region would then be changed to match the pressure distribution from the Embedded region. And so, the process would iterate until sufficient agreement was reached between the two regions.

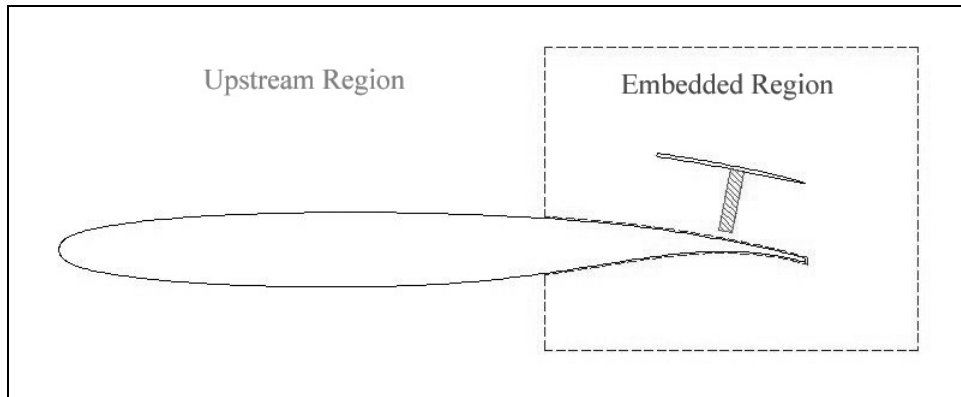


Figure 3.21: Embedded region approach used in ANSYS Flotran.

It was at about this time that our approach to applying distributed propulsion changed, moving from the ducted-engine concept to the jet-wing concept. As previously mentioned, the goal of this CFD analysis of distributed propulsion was to validate models and produce response surfaces for use in a Multidisciplinary Optimization (MDO) of the BWB [12], [24]. The progress in this greater project lead to a renewed favor of jet-wing distributed propulsion. It was thought that the ducted propulsor would help increase thrust by entraining the airflow through and around the duct [38]. However, recent studies by Presz, Reynolds, and Hunter [39] showed this only to be true at low speeds, such as at take-off and landing. Furthermore, the presence of the duct would increase drag at cruise conditions. Therefore, the jet-wing configuration won consideration over the ducted propulsor distributed propulsion configuration in the Virginia Tech MDO work. In the CFD analysis on distributed propulsion, the jet-wing approach would actually simplify the analysis. The jet exhaust would simply be modeled as boundary conditions applied to the trailing edge of the airfoil. Now, there would be no need for to model the engine cowl or actuator volume in the ANSYS Flotran Embedded region. Figure 3.22 shows the revised Embedded region approach.

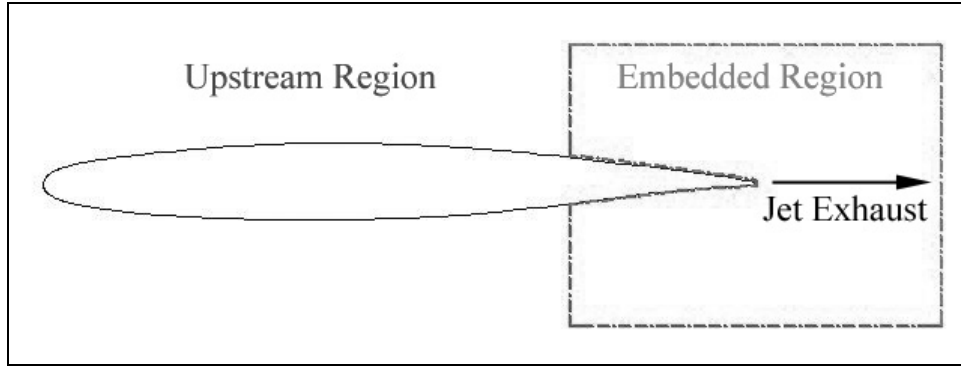


Figure 3.22: Embedded region approach with jet-wing.

3.3.2.1. Approximation of the Jet-Wing's Effect Using a Virtual Flap

The next task was to approximate the effect of the jet-wing on the flowfield around the airfoil using a flap. Yoshihara and Zonars [18] and Antinello [13] performed their studies using jet-flaps and found some analytical relations to estimate the effect of a jet-flap on an airfoil. While both the jet-flap and the jet-wing involve jet-exhaust exiting from the trailing edge of a wing, the jet-flap is typically used in high-lift applications rather than at cruise conditions like the jet-wing. Therefore, the jet-flap involves high deflection angles and high thrust. In the jet-flap studies, the jet coefficient C_J was calculated according to Equation (3.4). If it is assumed that the vehicle is self-propelled (that is, when the jet thrust exactly equals the local drag), then the jet coefficient C_J is simply equal to the local drag coefficient $C_{D_{local}}$, as in Equation (3.5).

$$C_J = \frac{m \cdot U_{jet}}{\frac{1}{2} \cdot \rho \cdot U_{\infty}^2 \cdot S} = \frac{T}{q \cdot S} \quad (3.4)$$

$$C_J = \frac{D_{local}}{q \cdot S} = C_{D_{local}} \quad (3.5)$$

The local drag coefficient computed by MSES for the Outboard 1xTE airfoil at a lift coefficient of $C_L = 0.69$ was $C_{D_{local}} = 0.0073$. Therefore, the Outboard 1xTE airfoil would require a jet coefficient of $C_J = 0.0073$ to be self-propelled. Antinello [13] and Yoshihara and Zonars [18] found a significant increase in lift for jet-flaps with a jet coefficient on the order of $C_J \approx 1.45$. Because the jet coefficient for the Outboard 1xTE airfoil is very much smaller than the $C_J \approx O(1)$ used by Antinello and Yoshihara and Zonars, it can be assumed that the jet-wing will not significantly affect either the lift or the pressure distribution. Therefore, no flap is needed to approximate the effect of the jet on airfoil in the Upstream region.

3.3.2.2. Embedded Region Boundary Conditions

The next task was to compute the boundary conditions into the Embedded region, and this proved to be more difficult than originally expected. The MSES code outputs a wide range of flow information, in several different ways. Some of the more notable output options include:

- Graphical pressure and Mach number distributions over the airfoil surface
- Contour plots the pressure, Mach number, and density throughout the flowfield
- Numerical values of lift, drag, and pitching moment
- Numerical values of the pressure distribution, Mach number, and boundary layer quantities over the surface of the airfoil

Even with all these choices of data output, some of the necessary output was not originally available: numerical flowfield pressure and velocity components; and numerical airfoil surface velocity distribution. The ANSYS embedded region requires pressure, velocity, and total temperature boundary conditions applied at the inlet, and a pressure boundary condition applied to the outlet. The Virginia Tech Boundary Layer applets require the surface pressure distribution in the form of the ratio of the local edge velocity to the freestream velocity, $\frac{U_e}{U_\infty}$.

To obtain the surface velocity distribution, Equation (3.6) [40] needed to be solved for the edge velocity ratio $\frac{U_e}{U_\infty}$ at each point along the airfoil surface using the pressure distribution from MSES (Figure 3.9).

$$C_p = \left(\frac{2}{\gamma \cdot M^2} \right) \cdot \left(\left[1 + \left(\frac{\gamma - 1}{2} \right) \cdot M^2 \cdot \left(1 - \left(\frac{U_e}{U_\infty} \right)^2 \right) \right]^{\frac{\gamma}{\gamma - 1}} - 1 \right) \quad (3.6)$$

In Equation (3.6), M is the local Mach number, C_p is the local pressure coefficient, and γ is the ratio of specific heats of air. Equation (3.6) was solved for the edge velocity distribution on the airfoil surface. Once found, the velocity distribution, along with flow properties and computational step sizes, were entered as input into the Virginia Tech Boundary Layer applet *WALZ*. *WALZ* is an integral laminar boundary layer code, based on the Thwaites-Walz method. *WALZ* can predict when the boundary layer will transition from laminar to turbulent using Michel's method. At the "point" of turbulent

transition, the *ITBL* code was run, using the results from *WALZ*. *ITBL* is a numerical, incompressible boundary layer code that can use several different turbulence models, including the mixing length, eddy viscosity, and turbulent kinetic energy (TKE) models. At first, the *ITBL* code was run with the mixing length turbulence model enabled, up to about 50% of the chord length. To give the most physically accurate results, *ITBL* was run with the TKE model enabled from the point $\frac{x}{c} \approx 50\%$ to the inlet of the Embedded region. Assuming the boundary layer does not separate, the *ITBL* applet can be stopped at any location along the airfoil. The termination point, the velocity and TKE profiles can be output across the boundary layer. Table 3.8 lists the parameters of the upper surface of the Outboard 1xTE airfoil for each boundary layer code run.

Table 3.8: Virginia Tech Boundary Layer applet parameters for Outboard 1xTE airfoil upper surface.

	<i>WALZ</i>	<i>ITBL</i>	<i>ITBL</i>
Kinematic viscosity, ν	3.770e-5 m ² /s	3.770e-5 m ² /s	3.770e-5 m ² /s
Freestream velocity, U_∞	213.86 m/s	213.86 m/s	213.86 m/s
Reference length, L	6.77 m	6.77 m	6.77 m
Surface type	2D body, rounded leading edge	--	--
Pressure gradient	specified	specified	specified
Maximum $\frac{x}{L}$	1.022	0.500	0.764
Number of x-steps	1023	523	317
Flat-plate transition Reynolds number, Re_{trans}	250,000	--	--
Starting $\frac{x}{L}$	--	0.063	0.500
Initial boundary layer thickness, δ_{ini}	--	8.399e-4 m	5.294e-2
y-step size	--	8.399e-7 m	5.294e-5 m
Number of y-steps	--	660,000	2,100
Turbulence model	--	Mixing Length	TKE
Initial velocity profile	--	Coles Profile	Coles Profile

With a little work, the output from *ITBL* can be used as an inlet boundary condition into the Embedded region. *ITBL* outputs the local boundary layer thickness δ , the local edge velocity ratio $\frac{U_e}{U_\infty}$, and the velocity component $\frac{u_{BL}}{U_e}$, $\frac{v_{BL}}{U_e}$ at each $\frac{y}{\delta}$ location across the boundary layer. Figure 3.23 illustrates the how the coordinate systems are arranged in the boundary layer. It is assumed that the edge velocity U_e is parallel to the airfoil surface, and that the velocity components inside the boundary layer u_{BL} , v_{BL} are oriented parallel and perpendicular to U_e , respectively. Therefore, a

coordinate transformation must be used to find the velocity components u , v into the Embedded region. Equation (3.7) shows that at a specified chord-wise position x , one can use ITBL and some simple transformations to find the u , v velocity components at each point y through the boundary layer. The pressure, p , and total temperature, T_0 , profiles through the boundary layer are assumed to be constant and equal to the pressure and total temperature at the edge of the boundary layer [41].

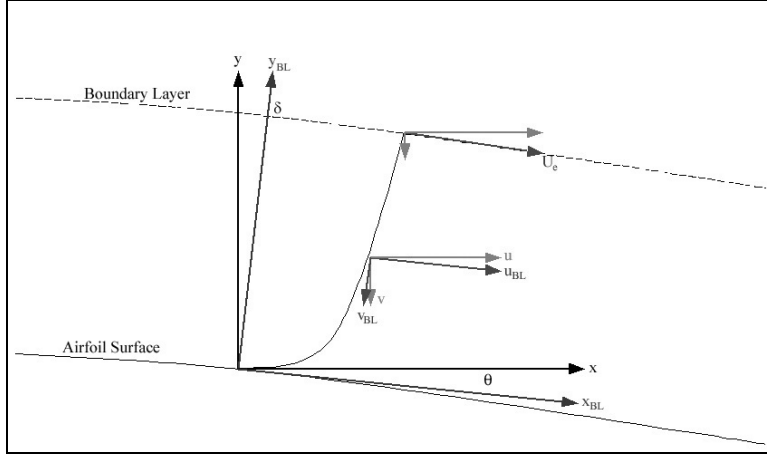


Figure 3.23: Boundary Layer velocity vector orientations.

$$y = \left(\frac{y}{\delta}\right) \cdot \delta$$

$$u = \left(\frac{u_{BL}}{U_e}\right) \cdot \left(\frac{U_e}{U_\infty}\right) \cdot U_\infty \cdot \cos(\theta) - \left(\frac{v_{BL}}{U_e}\right) \cdot \left(\frac{U_e}{U_\infty}\right) \cdot U_\infty \cdot \sin(\theta) \quad (3.7)$$

$$v = \left(\frac{u_{BL}}{U_e}\right) \cdot \left(\frac{U_e}{U_\infty}\right) \cdot U_\infty \cdot \sin(\theta) + \left(\frac{v_{BL}}{U_e}\right) \cdot \left(\frac{U_e}{U_\infty}\right) \cdot U_\infty \cdot \cos(\theta)$$

While the velocity profile through the boundary layer is important, the velocity, pressure, and total temperature profiles through the rest of flowfield span a much greater portion of the Embedded region inlet. As described earlier, MSES does not output the computed flowfield numerically. But, MSES does output flowfield quantities (including Mach number and pressure) graphically as contour plots. Therefore, MSES must compute the Mach number and pressure through the flowfield and store it somewhere. So, the question was, “How can this information be retrieved? “ Our distribution copy of MSES came in source code form, so that it could be compiled and run on a number of different computers. This made it possible to search the different output files for clues as to where the flowfield information was stored and how to retrieve it. After much effort, the correct variables were found and understood, and code was inserted into the MSES plotting routine to output the flowfield data. The exact details of this code and the MSES representation of the flowfield are outlined in Appendix B. In the end, it was possible to retrieve the velocity components u and v ,

the Mach number M , the pressure p , pressure coefficient C_p , and density ρ . The flowfield data was input into the *Tecplot* software package, where a linear interpolation was performed along the location of the inlet into the Embedded region. The velocity and pressure profiles from the flowfield were combined with the velocity and pressure profiles from the boundary layer. The total temperature T_0 , which is constant in the flow, was calculated from Equation (3.8) and equal to $T_0 = 241.7$ K. Figure 3.24, Figure 3.25, and Figure 3.26 show the u and v velocity and pressure profiles into the Embedded region inlet at $\frac{x}{c} = 0.74$. The only other necessary boundary condition applied to the Embedded region was the pressure at the exit. The pressure profile at this downstream location was also extracted from the MSES flowfield output in a manner similar to that described above. The downstream pressure profile is shown in Figure 3.27.

$$T_0 = T_\infty \cdot \left[1 + \frac{1}{2} \cdot (\gamma - 1) \cdot M_\infty^2 \right] \quad (3.8)$$

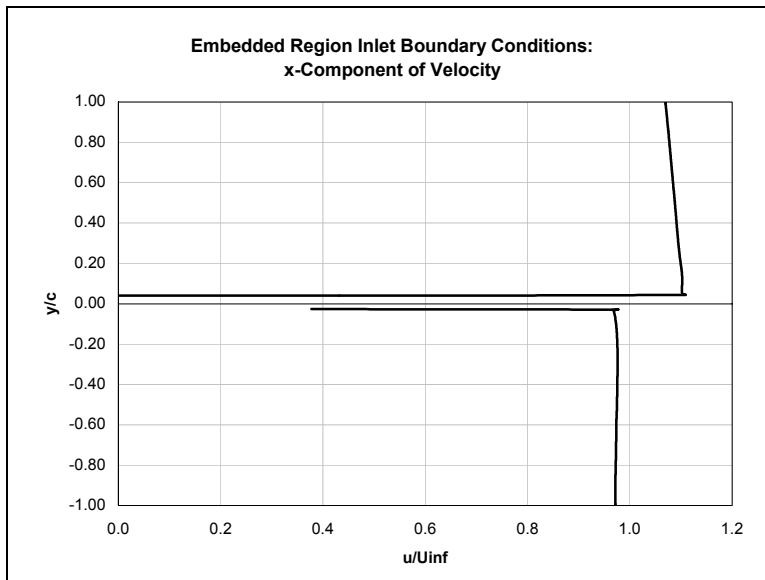


Figure 3.24: Embedded region Inlet boundary condition: x-component of velocity.

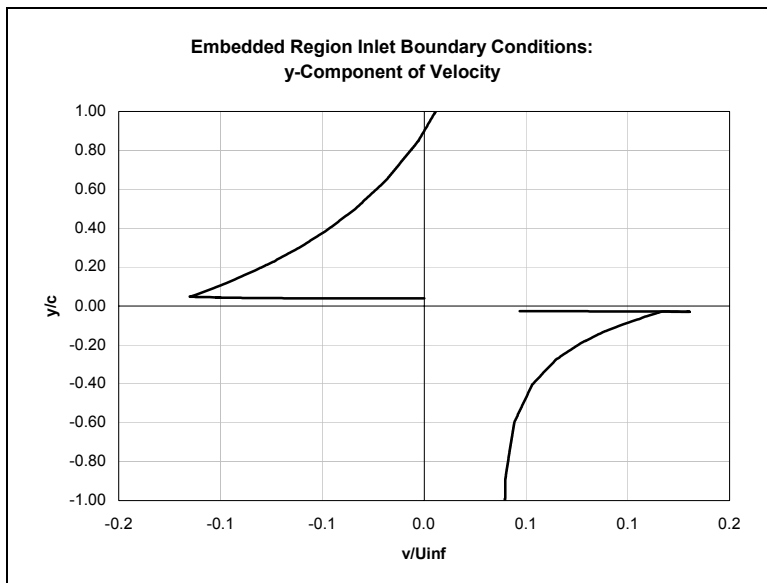


Figure 3.25: Embedded region Inlet boundary condition: y-component of velocity.

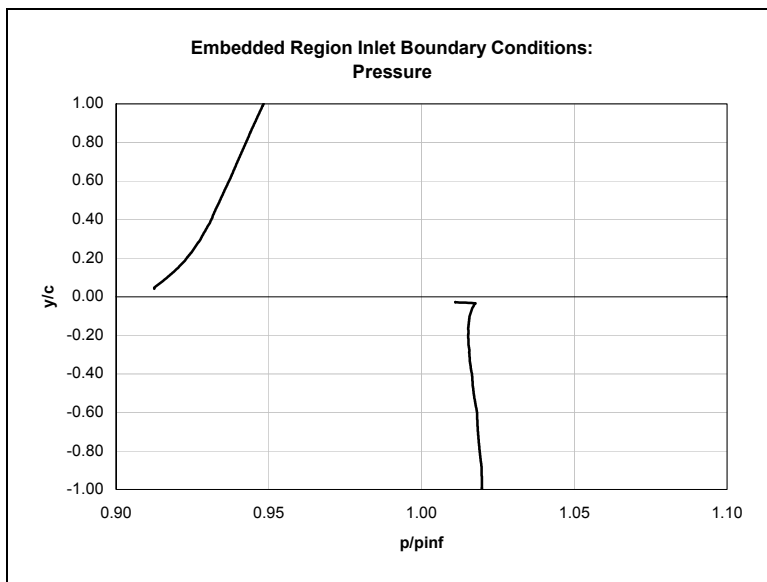


Figure 3.26: Embedded region Inlet boundary condition: pressure.

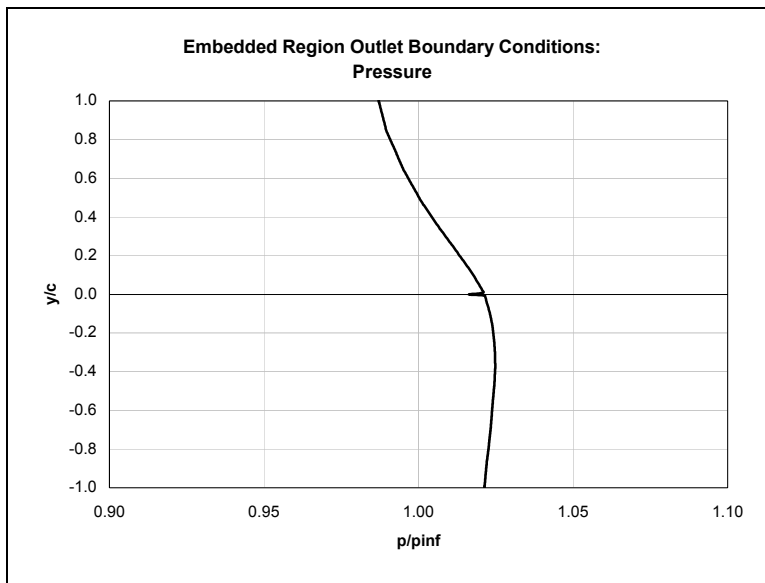


Figure 3.27: Embedded region Outlet boundary condition: pressure.

3.3.2.3. Embedded Region Grid Modeling

Once the general flow around the airfoil was solved -- including the boundary layer flow - it was time to construct the Embedded region in ANSYS Flotran. As illustrated in Figure 3.22, the Embedded region is a relatively small area around the trailing edge of the airfoil, where the jet-wing resides. How large should the embedded region be? The Embedded region should be large enough to model the flow to not incur any large interference effects, but small enough maintain the goal of low computational cost. Within this Embedded region, one important size scale is the boundary layer thickness at the trailing edge, δ_{TE} . In the boundary layer calculations, *ITBL* predicted the trailing edge boundary layer on the Outboard 1xTE airfoil to be 0.173 m thick on the upper surface, and 0.0933 m thick on the lower surface. The upper surface boundary layer thickness was selected as the reference scale for the Embedded region, as it was the larger of the two values. The boundary layer thickness of 0.173 m on the Outboard 1xTE airfoil corresponded to 2.56 % of the chord length. Initially, the Embedded region was sized as shown in Figure 3.28: the inlet of the Embedded region was positioned a distance $10 \cdot \delta_{TE}$ upstream of the trailing edge, the outlet was positioned $16 \cdot \delta_{TE}$ downstream of the trailing edge, and the upper and lower boundaries were located $5 \cdot \delta_{TE}$ away from the airfoil surface at the inlet. A grid (shown in Figure 3.29) was constructed for the Embedded region in ANSYS Flotran and the proper boundary conditions were applied. The velocity and pressure profiles shown in Figure 3.24,

Figure 3.25, and Figure 3.26 and the total temperature of $T_0 = 241.7 \text{ K}$ were applied as boundary conditions to the inlet of the Embedded region, located at $\frac{x}{c} = 0.74$ on the airfoil. At the outlet of the Embedded region, located at $\frac{x}{c} = 1.41$, the pressure profile in Figure 3.27 was applied as the boundary condition. A no-slip boundary condition was applied to the airfoil surface, including the trailing edge for preliminary studies. As a finite element method, ANSYS Flotran can handle a “free” boundary condition [35], [36] on the upper or lower surfaces of the Embedded region.

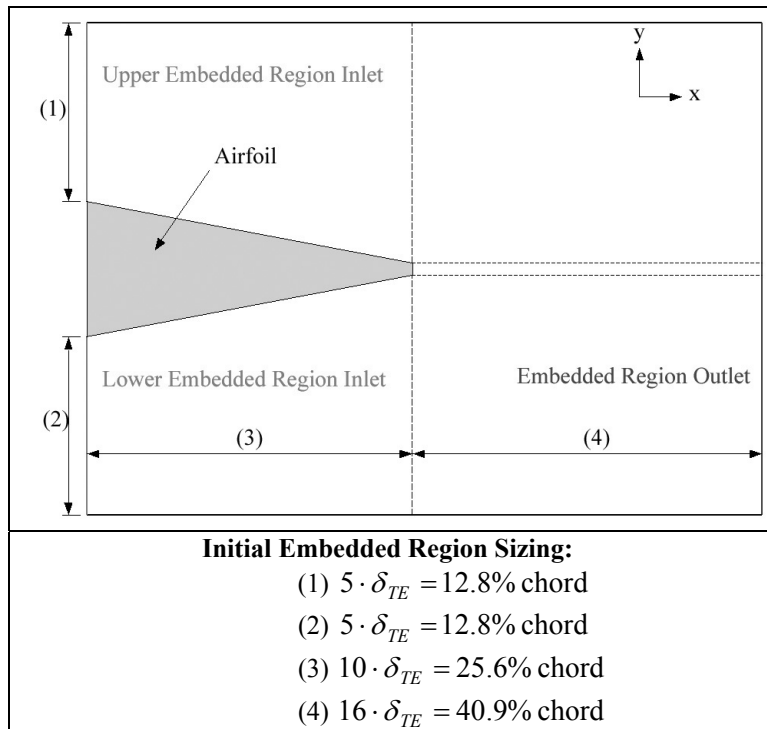


Figure 3.28: Initial sizing of Embedded region.

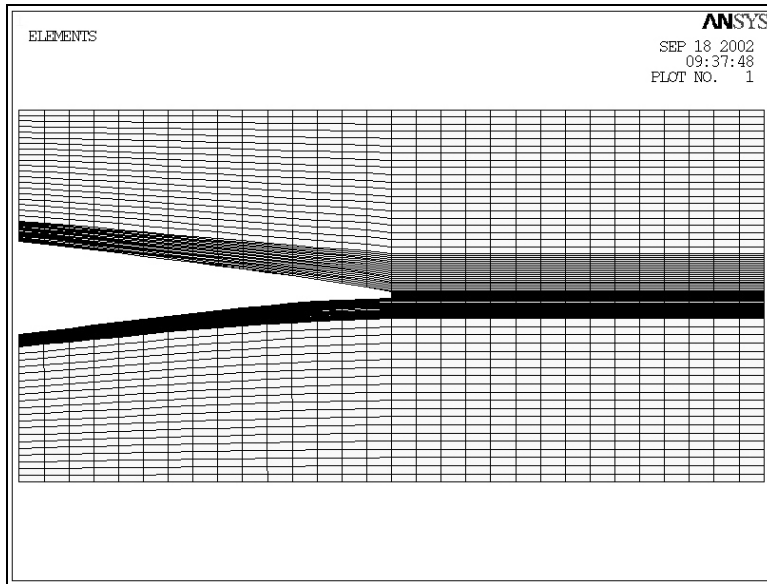


Figure 3.29: Initial ANSYS Flotran Embedded region grid.

3.3.2.4. Solving the Flow in the Embedded Region

The Embedded region was run for the Outboard 1xTE airfoil with no jet. The problem did not seem to converge, even as the number of iterations was increased. Also, the solution compared poorly with the solution predicted by MSES. The disagreement in solutions is clearly shown in the pressure distribution in Figure 3.30. Attempts were made to obtain the correct pressure distribution. The Embedded region grid was extended downstream to $24 \cdot \delta_{TE}$, or $\frac{x}{c} = 1.61$, the Embedded region upper and lower bounds were extended outwards to $15 \cdot \delta_{TE}$, or $\frac{y}{c} = 0.38$, and the pressure boundary condition applied to the Embedded region inlet was removed. The resulting pressure distributions are shown in Figure 3.31 and Figure 3.32. Unfortunately, the disagreement between the ANSYS Flotran Embedded region and MSES pressure distributions were on the order of 10-15% and greater. Because satisfactory results could not be obtained for the Outboard 1xTE airfoil with no jet, it became apparent that another method was necessary.

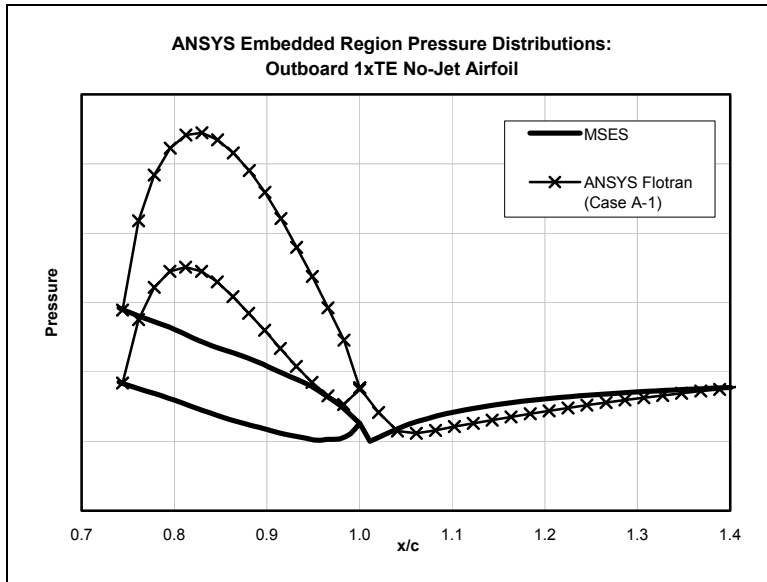
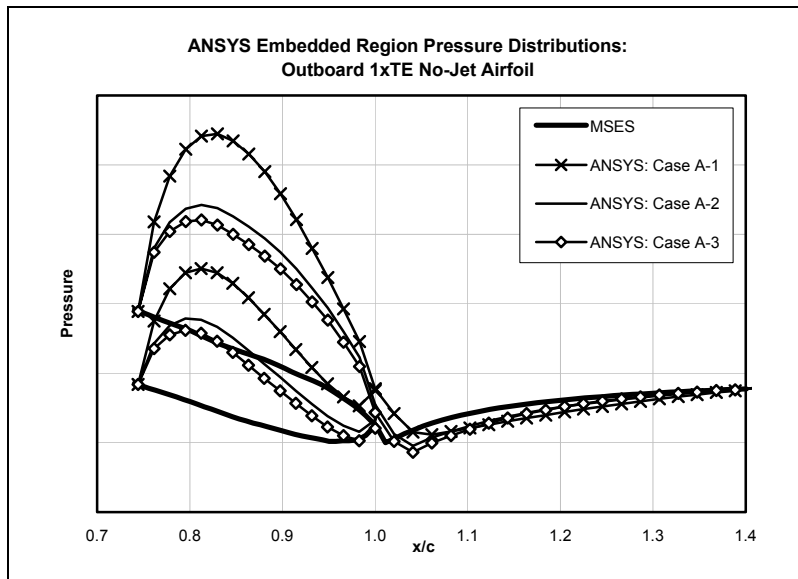


Figure 3.30: Embedded region pressure distribution.



ANSYS Case	Inlet BCs	Outlet BCs	Figure 3.28, dimensions (1) & (2)	Figure 3.28, dimension (4)
A-1	u, v, p, T_0	p	$5 \cdot \delta_{TE}$	$16 \cdot \delta_{TE}$
A-2	u, v, p, T_0	p	$10 \cdot \delta_{TE}$	$16 \cdot \delta_{TE}$
A-3	u, v, p, T_0	p	$15 \cdot \delta_{TE}$	$16 \cdot \delta_{TE}$

Figure 3.31: Embedded region pressure distribution for velocity, pressure, and total temperature inlet boundary conditions at various region sizes.

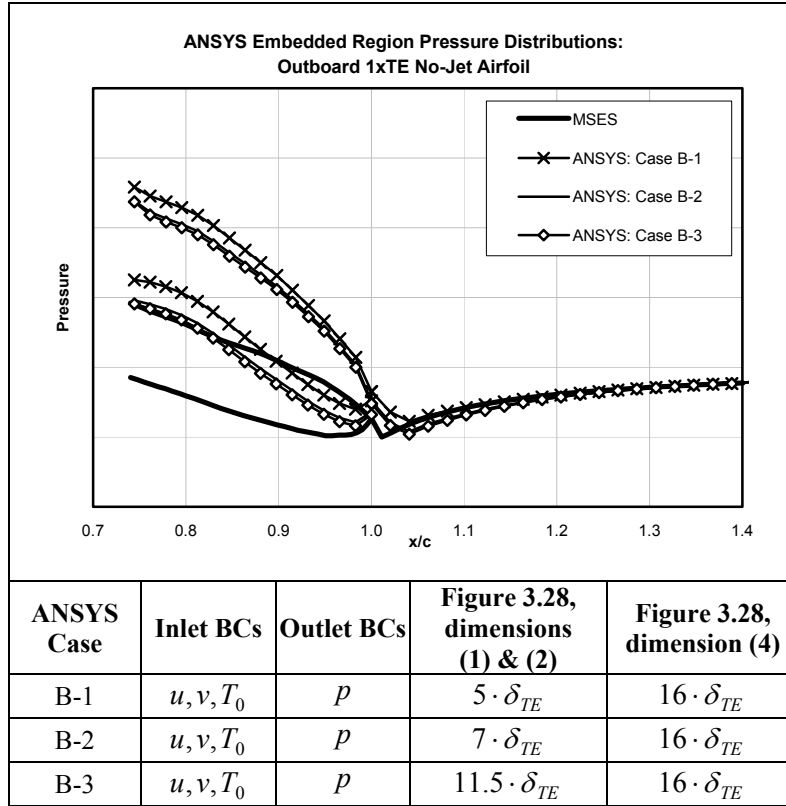


Figure 3.32: Embedded region pressure distribution for velocity and total temperature inlet boundary conditions at various region sizes.

3.4. Modeling the Jet-Wing with GASP

The Virginia Tech Aerospace and Ocean Engineering Department has a large amount of experience with the Reynolds-averaged, three-dimensional, finite-volume, Navier-Stokes code GASP [42]. Initially, GASP was not considered for modeling distributed propulsion, because the ducted propulsor configuration was adopted and GASP has no built-in actuator volume model. However, now that the jet-wing configuration was being applied to distributed propulsion, an actuator volume was not necessary and GASP could easily handle the jet-wing boundary conditions applied to the trailing edge of the airfoil.

3.4.1. Grid Generation

GASP solves the three-dimensional Navier-Stokes equations using a structured finite volume method. A structured C-grid was constructed for each airfoil model using the commercially available Gridgen Version 14 software package [43]. The grids for the three representative airfoil models were developed in Gridgen using similar parameters. Therefore, only the construction of the Outboard 1xTE airfoil grid will be discussed at

length. Differences between the grids for the Outboard 2xTE and Inboard airfoils and the Outboard 1xTE airfoil do exist and these differences will be fully explained.

3.4.1.1. Outboard 1xTE Airfoil

The Gridgen software is fast and easy to use once one has become acquainted with it. On a standard PC, these airfoil grids could be developed in less than an hour. The Outboard 1xTE airfoil grid was modeled using the full chord length of 6.77 m. The basic geometry of the C-grid is shown in Figure 3.33. Timothy Gatzke’s “Block-Structured Applications” chapter in [44] was used as a guideline for the sizing of the grid and spacing of the grid points. The grid extends 33 chord lengths downstream of the airfoil and over 25 chord lengths above and below the airfoil. Because the representative airfoils have thick trailing edges, the computational region had to be divided into two zones: one zone (the “trailing edge” zone) extending from the trailing edge to the downstream grid boundary and a second zone (the “airfoil” zone) wrapping around the airfoil and the trailing edge zone. There were 201 points along the upper surface of the airfoil, 125 points along the lower surface, and 41 points along the trailing edge surface. As observed from the MSES pressure distributions of the Outboard 1xTE airfoil in Figure 3.9, a shock is present on the upper surface of the airfoil, but not the lower surface. Therefore, a lower resolution grid could be used along the lower surface. There were 85 grid points placed along the length of the downstream zone. Grid spacing was specified at the leading edge of the airfoil and at the upper and lower corners of the trailing edge, these are listed in Table 3.9. Along each of these edges, the remaining grid points were spaced using a hyperbolic tangent spacing function built into Gridgen. The airfoil zone was extruded from the upper and lower surface edges and the shared trailing edge zone edges. A hyperbolic tangent function determined the grid spacing away from the airfoil surface, using an initial spacing of $1 \cdot 10^{-6}$ m. This initial grid spacing, determined using Equation (3.9) from [44], was chosen to locate the first grid point near a y^+ value of 1.0, while ensured that several grid points lie within the laminar sublayer.

$$\Delta y_{physical} = \left(\frac{c \cdot y^+}{\text{Re}_c} \right) \cdot \left(\frac{v_{wall}}{v_\infty} \right) \cdot \sqrt{\left(\frac{\rho_{wall}}{\rho_\infty} \right)} \cdot \frac{2}{C_f} \quad (3.9)$$

$$C_f = 0.0025 \cdot (\text{Re}_c)^{-\frac{1}{7}}$$

Figure 3.34 shows that the y^+ value of the first grid point is less than 1.0 along the upper and lower surfaces of the airfoil. In Gridgen, the grid was “extruded” away from the airfoil surface for 64 steps. It was necessary to specify several smoothing parameters as the grid was extruded; these are given in Table 3.10. In the trailing edge zone, Gridgen automatically creates a grid using the edge grid points, since they are specified on each edge. The grid that was created was a two-dimensional grid. GASP is a three-dimensional Navier-Stokes solver and requires a three-dimensional grid. Therefore, the grid was simply “extruded” a distance of one chord length along the z-direction (outward). Two grid points in the z-direction are all that are necessary for this two-dimensional airfoil model. The final grid for the Outboard 1xTE Airfoil is pictured in Figure 3.35, Figure 3.36, and Figure 3.37.

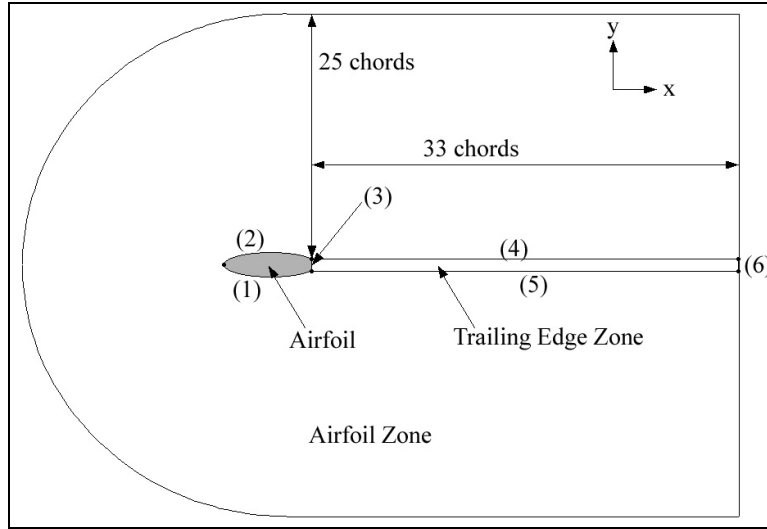


Figure 3.33: General airfoil grid geometry and nomenclature.

Table 3.9: Outboard 1xTE airfoil grid spacings (see Figure 3.33).

Gridgen Edge	Number of Grid Points	Beginning Step Size	Ending Step Size
(1) Airfoil Lower Surface	125	1e-4 m	1e-5 m
(2) Airfoil Upper Surface	201	1e-4 m	1e-5 m
(3) Airfoil Trailing Edge	41	1e-6 m	1e-6 m
(4) Trailing Edge Zone Upper Edge	85	1e-5 m	--
(5) Trailing Edge Zone Lower Edge	85	1e-5 m	--
(6) Trailing Edge Zone Outlet	41	1e-6 m	1e-6 m

Table 3.10: Outboard 1xTE airfoil Gridgen extrusion smoothing parameters for Airfoil zone.

Extrusion Step	1	2	3	4	5	6
Number of Steps	20	20	10	4	5	5
Explicit	0.5	0.5	0.5	0.5	0.5	0.5
Implicit	1.0	1.0	1.0	1.0	1.0	1.0
Volume	0.0	0.0	0.2	0.2	0.1	0.0
Kinsey-Barth	3.0	2.0	2.0	1.0	1.0	0.0
Geometric Growth Rate Factor	1.30	1.33	1.33	1.35	1.35	1.35

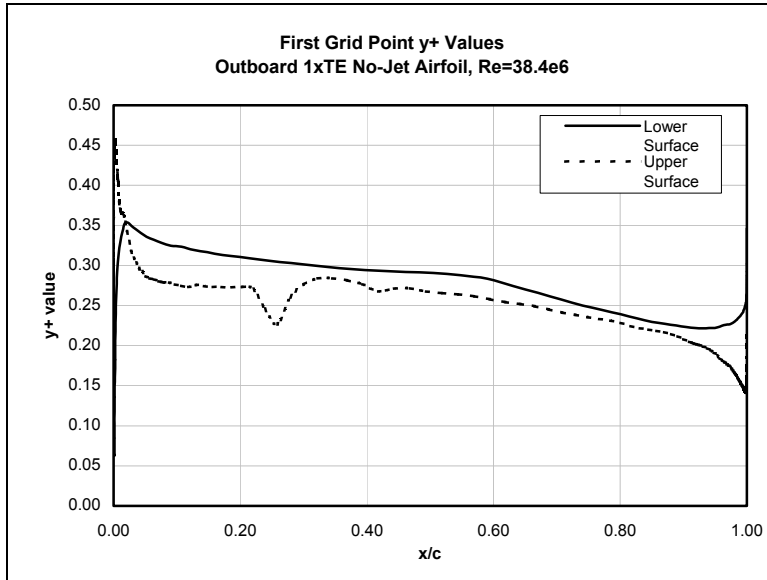


Figure 3.34: First grid point y^+ values for Outboard 1xTE no-jet airfoil.

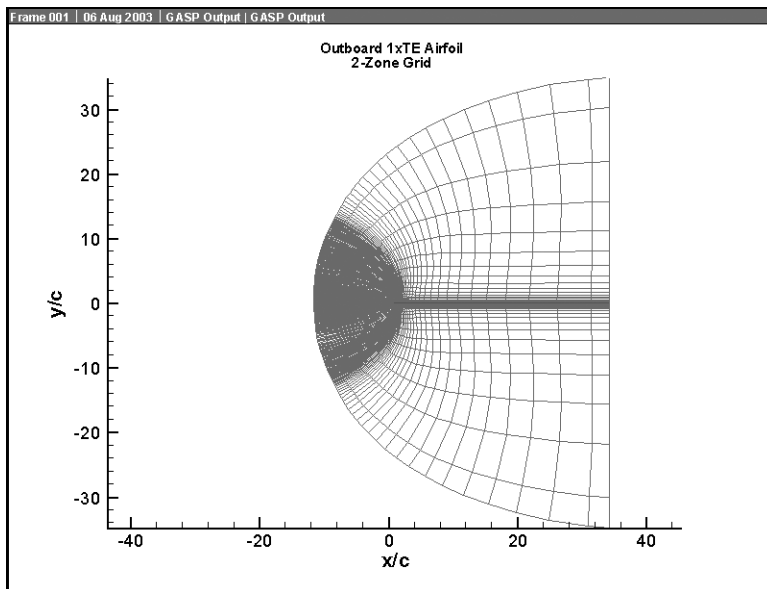


Figure 3.35: 2-zone grid of Outboard 1xTE airfoil (computational region).

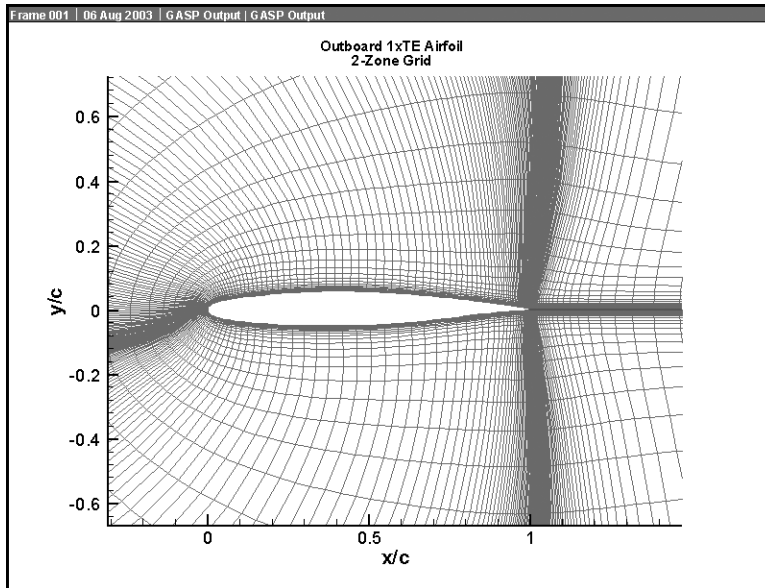


Figure 3.36: 2-zone grid of Outboard 1xTE airfoil (airfoil).

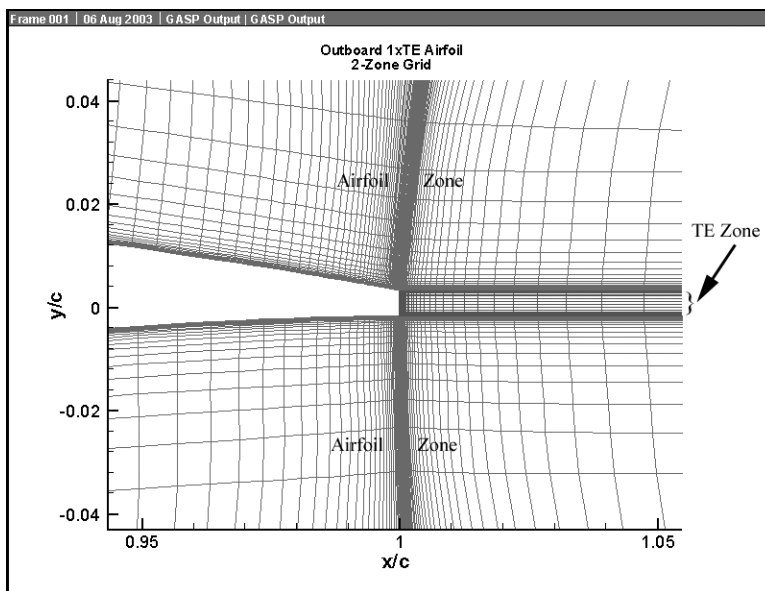


Figure 3.37: 2-zone grid of Outboard 1xTE airfoil (trailing edge).

3.4.1.1.1. Low Reynolds Number Outboard 1xTE Airfoil Cases

As the representative airfoil models were being run in GASP, a group of computations were made using a lower Reynolds number for comparison. The Outboard 1xTE airfoil was used, but with a chord length of 1.0 m. All other flow properties were kept the same. The grid spacing and smoothing parameters used are listed in Table 3.11 and Table 3.12. These computations for the Outboard 1xTE airfoil were run at a Reynolds number of 5.67 million, compared to the BWB Reynolds number

of 38.40 million. While this data cannot be applied to distributed propulsion of a BWB-sized aircraft, it can be applied to smaller, UAV-type aircraft.

Table 3.11: Low Reynolds number Outboard 1xTE airfoil grid spacings (see Figure 3.33).

Gridgen Edge	Number of Grid Points	Beginning Step Size	Ending Step Size
(1) Airfoil Lower Surface	101	1e-3 m	1e-4 m
(2) Airfoil Upper Surface	197	1e-3 m	1e-4 m
(3) Airfoil Trailing Edge	41	1e-5 m	1e-5 m
(4) Trailing Edge Zone Upper Edge	85	1e-4 m	--
(5) Trailing Edge Zone Lower Edge	85	1e-4 m	--
(6) Trailing Edge Zone Outlet	41	1e-5 m	1e-5 m

Table 3.12: Low Reynolds number Outboard 1xTE airfoil Gridgen extrusion smoothing parameters for Airfoil zone.

Extrusion Step	1	2	3
Number of Steps	40	10	14
Explicit	0.5	0.5	0.5
Implicit	1.0	1.0	1.0
Volume	0.0	0.3	0.5
Kinsey-Barth	3.0	1.0	1.0
Geometric Growth Rate Factor	1.235	1.235	1.235

3.4.1.2. Outboard 2xTE Airfoil

The grid geometry of the Outboard 2xTE airfoil differed little from the Outboard 1xTE Airfoil. The trailing edge thickness of the Outboard 2xTE airfoil was doubled over that of the Outboard 1xTE airfoil. Therefore, the number of grid points placed along the trailing edge (edges 3 and 6 in Figure 3.33) was increased from 41 points to 81 points. The trailing edge of the Outboard 2xTE airfoil is pictured in Figure 3.38.

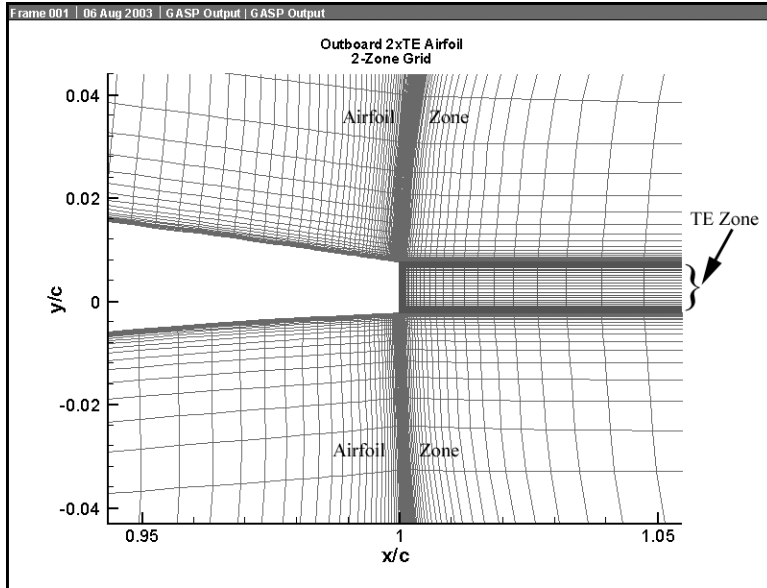


Figure 3.38: 2-zone grid of Outboard 2xTE airfoil (trailing edge).

3.4.1.3. Inboard Airfoil

The grid for the Inboard airfoil was constructed in a similar manner as the Outboard airfoils. Using Equation (3.9), the initial grid spacing in the normal direction (away from the airfoil) was chosen as $2 \cdot 10^{-6}$ m. Due to the larger chord length, 24 more points were added to the upper surface. Also, because shocks are present on both surfaces of the airfoil (see Figure 3.13) the same number of points was used on the lower surface as the upper surface. Therefore, the upper and lower surface each had 225 grid points. The trailing edge thickness was 1% of the chord, so 81 points were located across the trailing edge surface, as with the Outboard 2xTE airfoil grid. The rest of the Inboard airfoil grid spacing parameters are given in Table 3.13 and Table 3.14. The grid is shown in Figure 3.39.

Table 3.13: Inboard airfoil grid spacings (see Figure 3.33).

Gridgen Edge	Number of Grid Points	Beginning Step Size	Ending Step Size
(1) Airfoil Lower Surface	225	2e-4 m	2e-5 m
(2) Airfoil Upper Surface	225	2e-4 m	2e-5 m
(3) Airfoil Trailing Edge	81	2e-6 m	2e-6 m
(4) Trailing Edge Zone Upper Edge	85	2e-5 m	--
(5) Trailing Edge Zone Lower Edge	85	2e-5 m	--
(6) Trailing Edge Zone Outlet	81	2e-6 m	2e-6 m

Table 3.14: Inboard airfoil Gridgen extrusion smoothing parameters for Airfoil zone.

Extrusion Step	1	2	3	4	5	6
Number of Steps	20	20	10	4	5	5
Explicit	0.5	0.5	0.5	0.5	0.5	0.5
Implicit	1.0	1.0	1.0	1.0	1.0	1.0

Volume	0.0	0.0	0.2	0.3	0.3	0.5
Kinsey-Barth	3.0	2.0	1.0	1.0	0.0	0.0
Geometric Growth Rate Factor	1.35	1.35	1.35	1.35	1.35	1.35

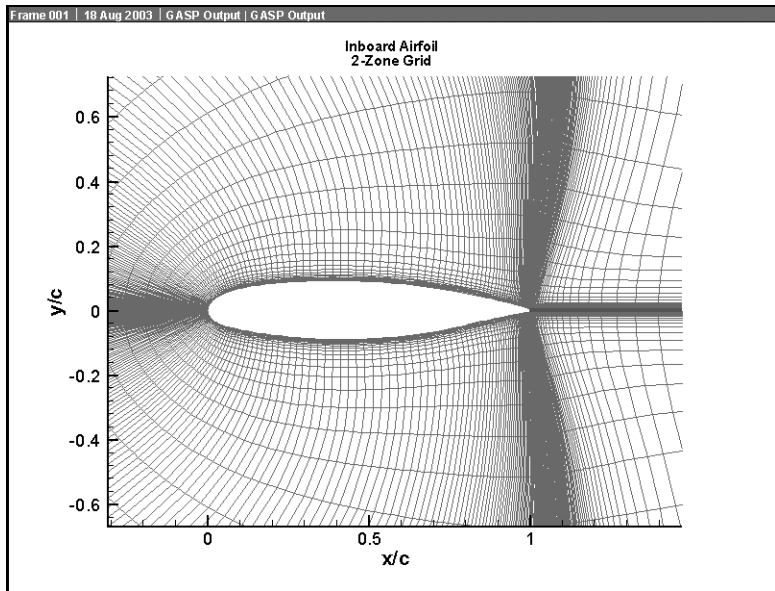


Figure 3.39: 2-zone grid of Inboard airfoil (airfoil).

3.4.2. GASP Modeling Parameters

GASP version 4.1.1 was used for the jet-wing CFD computations. As a three-dimensional Navier-Stokes code, GASP required many parameters must be set before a model was ready to be run. The more noteworthy set-up procedures are explained below.

3.4.2.1. Defining Surfaces on Computational Domain

First, it was necessary to import the airfoil grid from Gridgen into GASP. After this was complete, the surfaces of the model were named as shown in Figure 3.40. The term “Point-to-Point” surface simply means that the points on the surfaces of the two zones are linked along these surfaces and share the same properties.

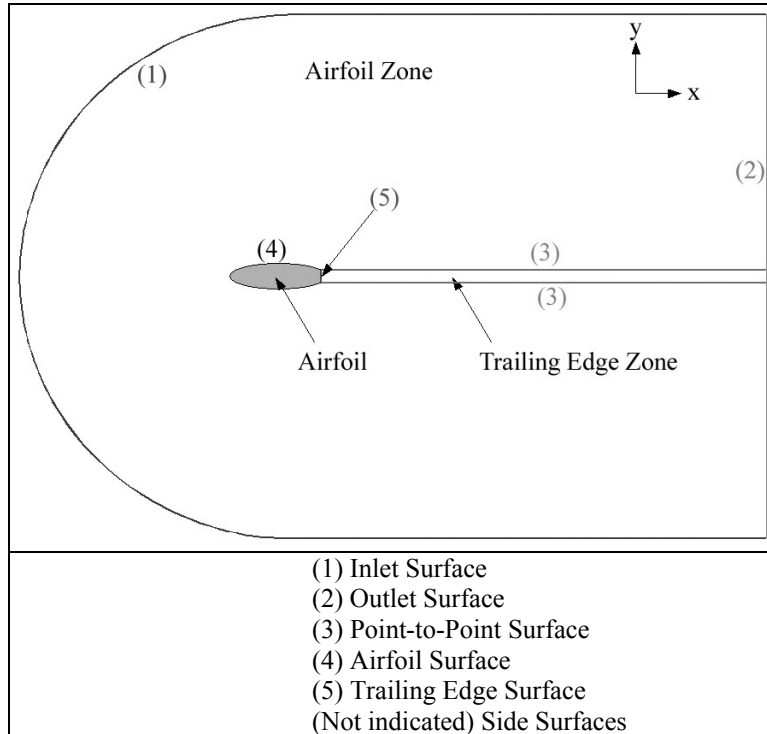


Figure 3.40: GASP surface definitions.

3.4.2.2. Grid Sequencing and Levels

Next, three different grid levels were formed: fine, medium, and coarse. The Fine grid simply used the grid constructed in Gridgen and all its points. The Medium grid level was constructed by GASP by eliminating every other i - and j -point from the Fine grid in the x - y planes. The Medium grid was therefore only half as fine as the Fine grid in each direction. The Coarse grid level further eliminated every other i - and j -point from the Medium grid in the x - y planes. The Coarse grid was only a quarter as fine as the Fine grid in each direction. The procedure was performed for each airfoil model in order to quicken the convergence. The Coarse grid only had about a sixteenth as many cells as the Fine grid and could be converged in about 13 total CPU hours. The solution was interpolated to the Medium grid and used as the initial solution. In a similar manner, the Medium grid was converged and its solution interpolated and applied to the Fine grid as the initial solution. This sequencing through Coarse, to Medium, and to Fine grids allows the solution to converge much more quickly than simply running and converging the solution on the finest grid level.

3.4.2.2.1. Special Hybrid Grid for the Inboard Airfoil

The Inboard airfoil proved more difficult to treat than the Outboard airfoils. When first run, the net lift coefficient of the Coarse and Medium grid solutions converged, but that of the Fine grid actually appeared to oscillate and diverge. This is shown in Figure 3.41. However, the Medium grid solution seemed to converge well, so that solution was investigated. Figure 3.42 shows that the first grid point y^+ values are sufficient as they are less than 1.0. The pressure distribution in Figure 3.43 shows poor resolution of the shocks on the airfoil's upper and lower surface. The sharpness of the shocks could be improved if the grid spacing along the airfoil was decreased in the regions of the shocks. Lastly, Figure 3.44 shows that separation does occur on the upper surface of the Inboard airfoil at about 90% of the chord. Therefore, the Medium grid provides enough resolution of the flow near the surface of the airfoil, but does not provide sufficient resolution of the shock waves. To remedy this problem, a grid was formed using the fine grid in the i-direction (tangent to the airfoil) and the medium grid in the j-direction (normal to the airfoil). This grid will be referred to as the "Hybrid" grid, and it is shown in Figure 3.45. As observed in Figure 3.46, the Hybrid grid solution converges better than the Fine grid solution, but oscillations in the net lift coefficient are present. This indicates that the flow could be periodic. As with the Medium grid solution, the first grid point y^+ values in Figure 3.47 are sufficiently small. Also, Figure 3.48 shows that the Hybrid grid solution models sharper shocks than the Medium grid solution. Lastly, separation occurs at about 90% of the chord for both the Medium and Hybrid grid solutions, as shown in Figure 3.49. Therefore, because the Hybrid grid solution sufficiently resolved the flow near the airfoil surface and the shock waves, the Hybrid grid was used for the Inboard no-jet and jet-wing airfoil cases.

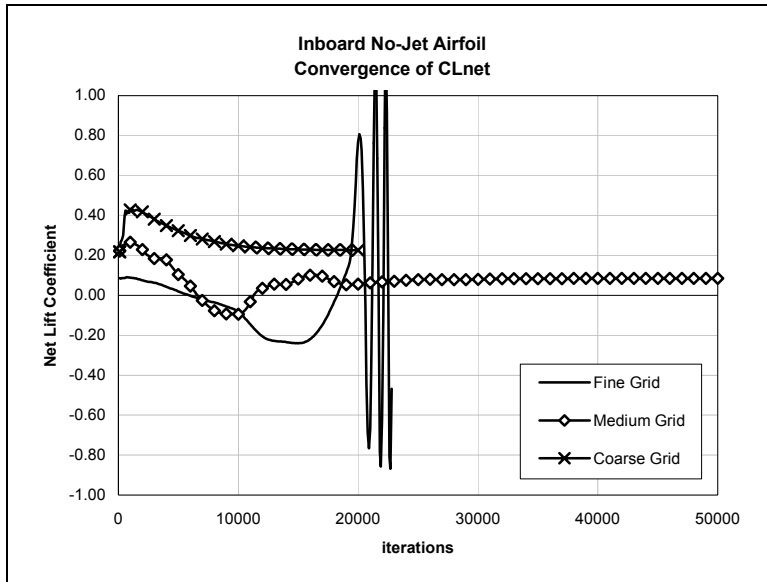


Figure 3.41: Inboard no-jet airfoil GASP grid convergence history.

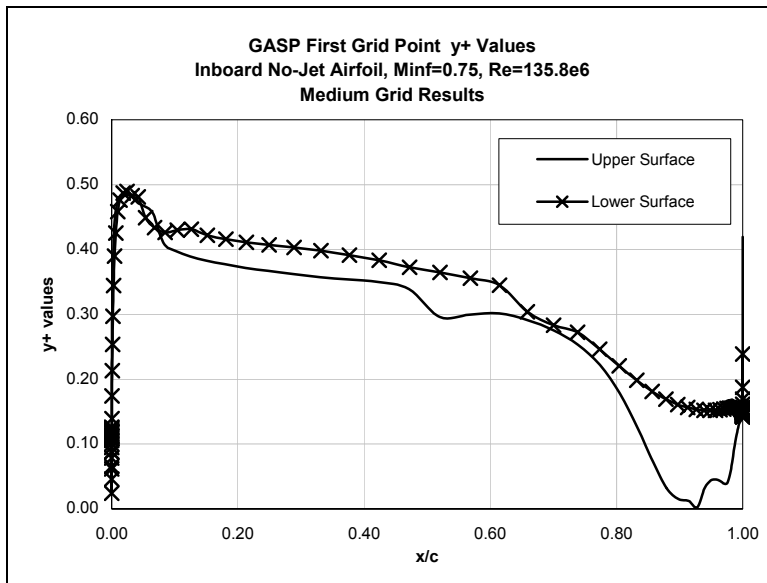


Figure 3.42: Inboard no-jet airfoil GASP first grid point y^+ value on Medium grid.

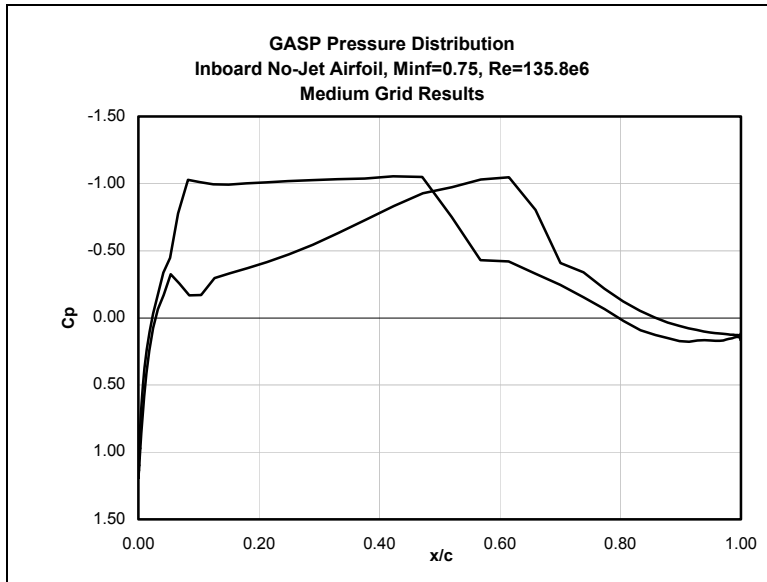


Figure 3.43: Inboard no-jet airfoil GASP pressure distribution on Medium grid.

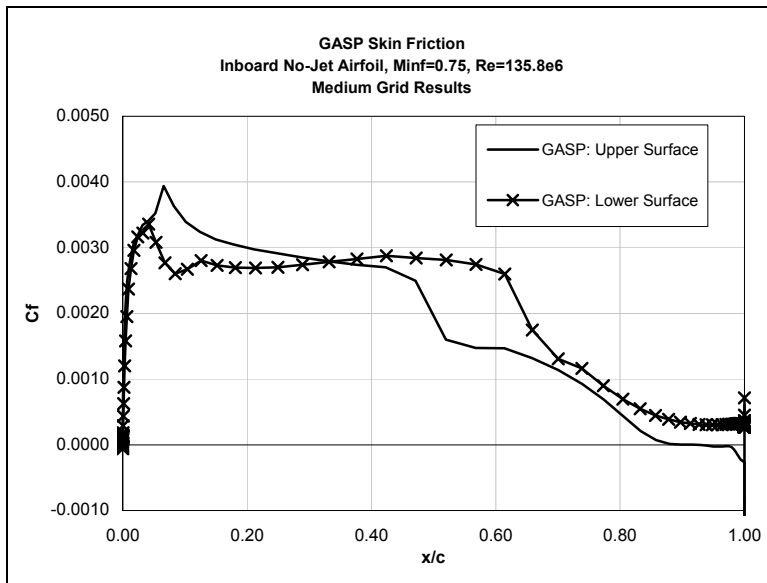


Figure 3.44: Inboard no-jet airfoil GASP skin friction on Medium grid.

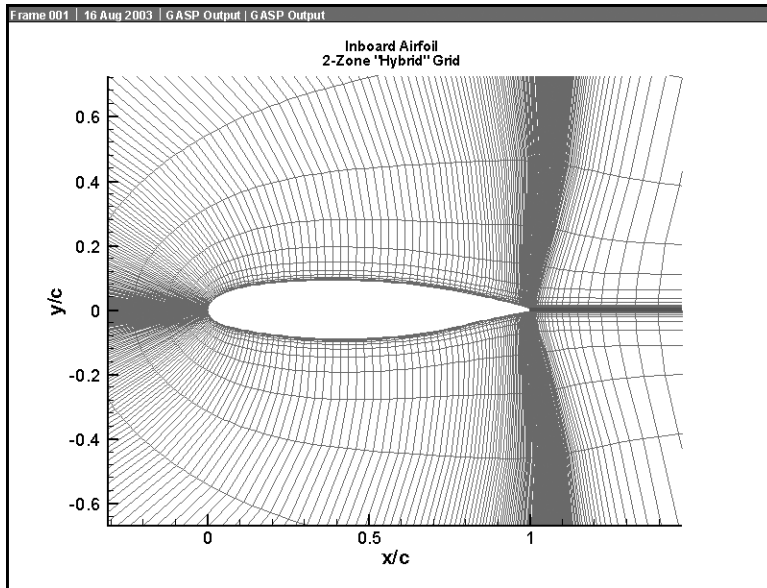


Figure 3.45: Inboard airfoil "Hybrid" grid.

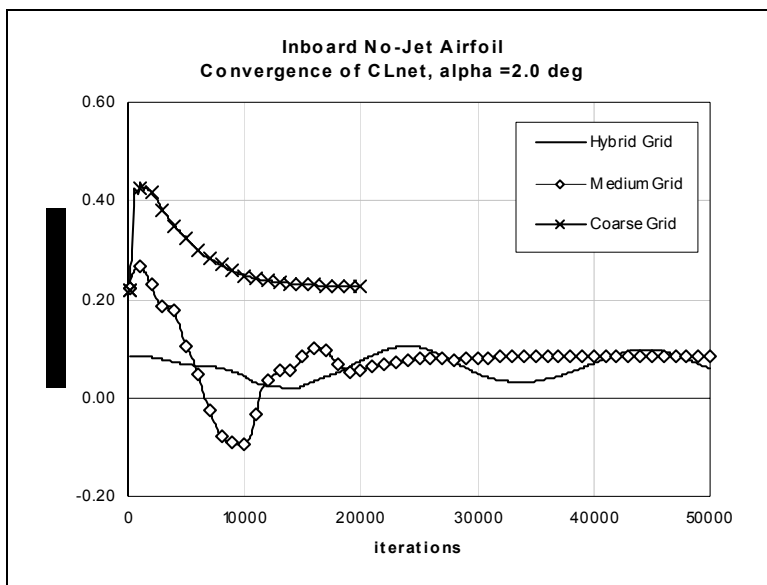


Figure 3.46: Inboard no-jet airfoil GASP grid convergence history using Hybrid grid.

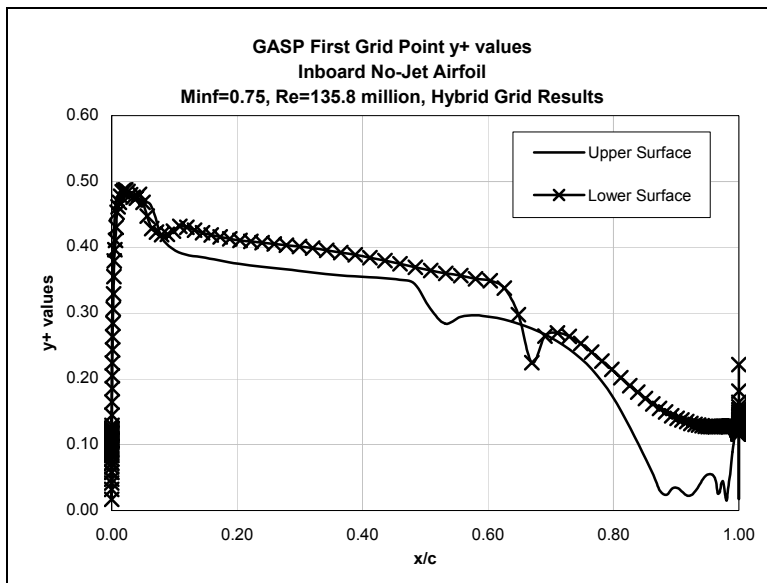


Figure 3.47: Inboard no-jet airfoil GASP first grid point y^+ value on Hybrid grid.

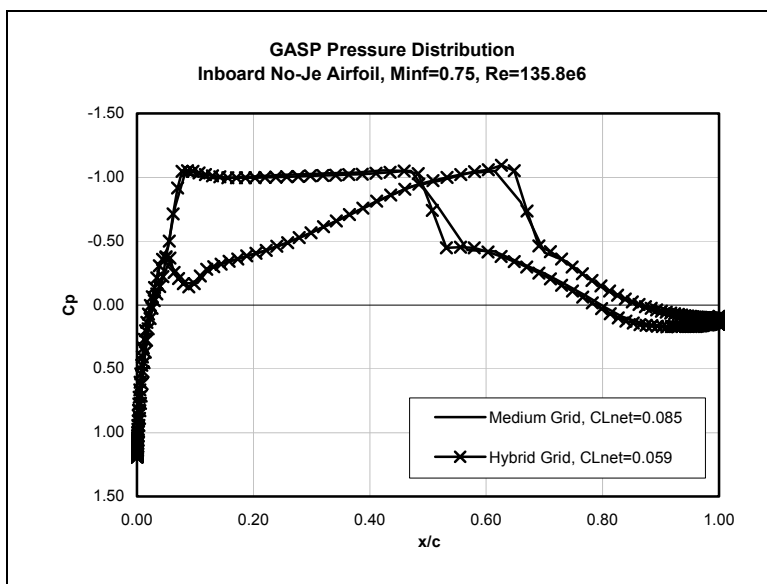


Figure 3.48: Inboard no-jet airfoil GASP pressure distribution on Hybrid and Medium grids.

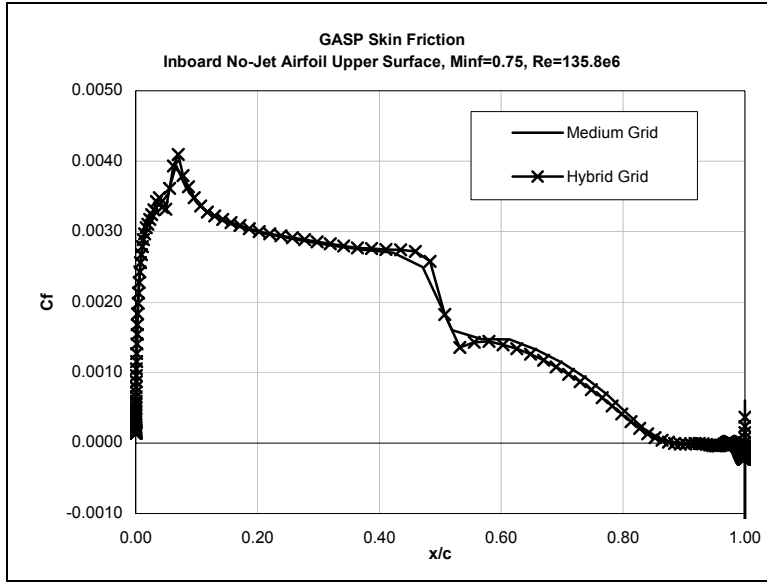


Figure 3.49: Inboard no-jet airfoil GASP skin friction on Hybrid and Medium grids.

3.4.2.3. Specifying Freestream Properties

Next, the physical properties and models were specified in GASP. These included the freestream flow properties, jet flow properties, inviscid models, viscous models, and boundary conditions. For both the freestream and jet flow properties, it was necessary to set the Mach number, density, temperature, and flow angle. The Mach number and flow temperature in the freestream were set according to Table 3.1. Since the actual airfoil chord lengths were used when constructing the grids (6.77 m for the Outboard airfoils and 23.01 m for the Inboard airfoil) no scaling of properties was necessary. The angle of attack α was used in Equation (3.10) to specify a flow direction vector. The freestream properties for the three representative airfoils (without jet-wing) are given in Table 3.15.

$$\begin{aligned}
 \hat{U}_x &= \cos(\alpha) \\
 \hat{U}_y &= \sin(\alpha) \\
 \hat{U}_z &= 0
 \end{aligned}
 \tag{3.10}$$

Table 3.15: GASP freestream properties for representative airfoil models.

	Outboard 1xTE Airfoil	Outboard 2xTE Airfoil	Inboard Airfoil
Freestream Mach Number, M_∞	0.72	0.72	0.75
Freestream Temperature, T_∞	218.93 K	218.93 K	218.93 K
Freestream Density, ρ_∞	0.3807 kg/m ³	0.3807 kg/m ³	0.3807 kg/m ³
Angle of Attack, α	2.66°	3.00°	2.00°
x-comp. of Flow Direction, \hat{U}_x	0.99892	0.998630	0.99939
y-comp. of Flow Direction, \hat{U}_y	0.046409	0.523360	0.034899
Reynolds Number, Re_c	38.40e+6	38.40e+6	135.8e+6

3.4.2.4. Specifying Jet Flow Properties

The jet flow properties were determined using the results of the no-jet airfoil cases. To simplify the modeling, it was assumed that the jet would use exhaust from the engine fan and that it would be the same temperature as the freestream. Furthermore, the pressure of the jet flow was set equal to the average of pressures on the upper and lower surfaces of the airfoil at the trailing edge. Since GASP uses the flow density, the jet flow density was calculated using the ideal gas law. Thus, the jet flow temperature T_{jet} and density ρ_{jet} were found using Equation (3.11), where R was the gas constant of air.

$$p_{jet} = \frac{1}{2} \cdot (p_{TE_{upper}} + p_{TE_{lower}}) \quad (3.11)$$

$$\rho_{jet} = \frac{p_{jet}}{R \cdot T_{jet}}$$

The jet flow Mach number M_{jet} was determined from the thrust of the jet. Since the jet-wing is locally self-propelled, the jet thrust component in the freestream direction is equal to the drag:

$$Thrust_{jet} \cdot \cos(\alpha + \tau) = D$$

$$Thrust_{jet} \cdot \cos(\alpha + \tau) = C_D \cdot \left(\frac{1}{2} \cdot \rho_\infty \cdot U_\infty^2 \cdot c \cdot b \right) \quad (3.12)$$

In Equation (3.12), τ is the jet angle relative to the chord line, D and C_D are the drag and drag coefficient, respectively, c is the chord length, and b is unit the span, which is taken 1 m. The jet thrust was found from the thrust equation:

$$Thrust_{jet} = \rho_{jet} \cdot U_{jet} \cdot h_{jet} \cdot (U_{jet} - U_\infty) + (p_{jet} - p_\infty) \cdot h_{jet} \quad (3.13)$$

In Equation (3.13), U_{jet} is the jet velocity and h_{jet} is the jet height, which is equal to the trailing edge thickness. After some manipulating, the following equation was obtained:

$$\frac{C_D \cdot \left(\frac{1}{2} \cdot \rho_\infty \cdot U_\infty^2 \cdot c \cdot b\right)}{\cos(\alpha + \tau)} = \rho_{jet} \cdot U_{jet} \cdot h_{jet} \cdot (U_{jet} - U_\infty) + (p_{jet} - p_\infty) \cdot h_{jet} \quad (3.14)$$

Equation (3.14) was solved for the jet flow velocity U_{jet} using the equation solvers in *Mathematica*. Since the jet flow temperature and freestream temperature were equal, the speed of sound was also equal in the two flows. Therefore, the jet flow Mach number was found in Equation (3.15).

$$\begin{aligned} a_{jet} &= a_\infty \\ M_{jet} &= \frac{U_{jet}}{a_{jet}} \end{aligned} \quad (3.15)$$

The jet flow properties are listed in Table 3.16.

Table 3.16: GASP jet flow properties for representative jet-wing airfoil models.

	Outboard 1xTE Airfoil	Outboard 2xTE Airfoil	Inboard Airfoil
Drag Coefficient, C_D	0.0124	0.0136	0.0384
Jet Mach Number, M_∞	1.199	1.021	1.385
Jet Temperature, T_∞	218.93 K	218.93 K	218.93 K
Jet Density (Scaled), ρ_∞	0.4054 kg/m³	0.4009 kg/m³	0.4004 kg/m³
Jet Angle, τ	0.0°	0.0°	0.0°
x-comp. of Flow Direction, \hat{U}_x	1.0	1.0	1.0
y-comp. of Flow Direction, \hat{U}_y	0.0	0.0	0.0

3.4.2.5. Boundary Conditions

It was necessary to specify boundary conditions on all the surfaces of the computational domain. These surfaces include those denoted in Figure 3.40, and the two “side” surfaces (those parallel with the paper: GASP requires finite volumes, even for two-dimensional models). Using the notation in Figure 3.40, the Inlet and Outlet surfaces use a Reimann Subsonic Inflow/Outflow boundary condition, using the freestream properties given in Table 3.15. Flux splitting is enabled along these surfaces. The “side” surfaces used a First-order Extrapolation boundary condition, with flux splitting enabled. The Airfoil surface uses a No-slip, Adiabatic boundary condition, with flux splitting disabled along the surface. When there is no trailing edge jet, the Trailing Edge surface uses the same No-slip, Adiabatic boundary condition as the Airfoil surface.

For the jet-wing cases, where there is a jet exhausting from the Trailing Edge surface, a Fixed- Q , No Turbulence boundary condition was employed, using the jet flow properties in Table 3.16. Q is defined by GASP [42] as the set of variables used to specify the flow conditions. This set of parameters includes temperature, pressure, density, velocity, laminar and turbulent viscosities, and Mach number. Therefore, Q_∞ is the set of flow parameters specifying the freestream conditions and Q_{local} is the set of flow parameters at an individual cell. Flux splitting is disabled along the surface. This boundary condition is sufficient for a supersonic jet flow ($M_{jet} > 1$) and seems to have worked for all the models (even when M_{jet} was very near 1). If the jet flow were subsonic ($M_{jet} < 1$) the “Subsonic $p_0 - T_0$ Inflow/Outflow” condition would be used as the jet flow boundary condition [42].

3.4.2.6. Inviscid, Viscous, and Thermo-Chemistry Models

The next group of parameters set in each GASP model determined the inviscid and viscous models. The inviscid fluxes used an upwind-biased third-order spatially accurate Roe flux scheme. A Van-Albada flux limiter was utilized to prevent any non-physical oscillations from occurring in the computations.

The computational solution included all the viscous terms and used Menter’s Shear Stress Transport $K - \omega$ turbulence model. A $K - \omega$ limiting factor used to prevent instability [42] was typically set to 2000 times the viscosity. Compressibility corrections were enabled, and wall functions were disabled for each computation.

GASP does have the capability to model real gas effects, including chemical reactions. Because it is assumed that the jet-wing uses the cold exhaust from the fan of a turbofan engine, the complexity of chemical modeling is unnecessary. Therefore, the computations were performed using a perfect gas chemistry model with the chemical composition frozen.

3.4.2.7. Run Settings

The steady-state solution was computed by GASP. A Gauss-Seidel implicit scheme was used. Also, the GASP solution was computed using the three grid sequences described in Section 3.4.2.1 above: the Coarse, Medium, and Fine grids. GASP first ran the Coarse grid, computed the solution, and interpolated the solution to use as initial conditions for the Medium grid. The Medium was similarly interpolated and

applied as an initial condition for the Fine grid. The convergence of the solution was based on the overall residual, which is the sum of the L^2 norm of all the governing equations solved in each cell. Typically, the solution was converged when the L^2 norm of the residuals was reduced by four to six orders of magnitude on the each grid. However, it was common for the L^2 norm of the residuals to decrease very quickly during the coarse grid sequence (11 orders or magnitude in less than 100 iterations). Therefore, it was also necessary to qualitatively monitor the lift and drag coefficients (C_L and C_D , respectively) for convergence. When the solution was converged, the lift and drag coefficients remained constant, as in Figure 3.50. Typical of the Outboard Airfoil runs, the Coarse grid was run for 10,000 iterations, using Q_∞ to determine the time step. The Medium grid was run for 10,000 iterations using Q_{local} to compute the time step, and then 10,000 more using Q_∞ . The Fine grid was run for 5,000 iterations using Q_{local} to determine the time step and then 15,000 iterations using Q_∞ . The Fine grid convergence of the Outboard 2xTE no-jet airfoil is shown in Figure 3.50. The Inboard Airfoil used a similar progression, but with a greater number of iterations as it was a more difficult case to converge. All the Outboard and Inboard Airfoil cases were run on an SGI Origin 2000 computer system with 32 processors, with jobs typically running on eight processors. Convergence of the Fine grid of the Outboard Airfoils was usually accomplished using 500 hours of total CPU time. The Inboard Airfoils cases with the Hybrid grid were completed using under 600 hours of total CPU time.

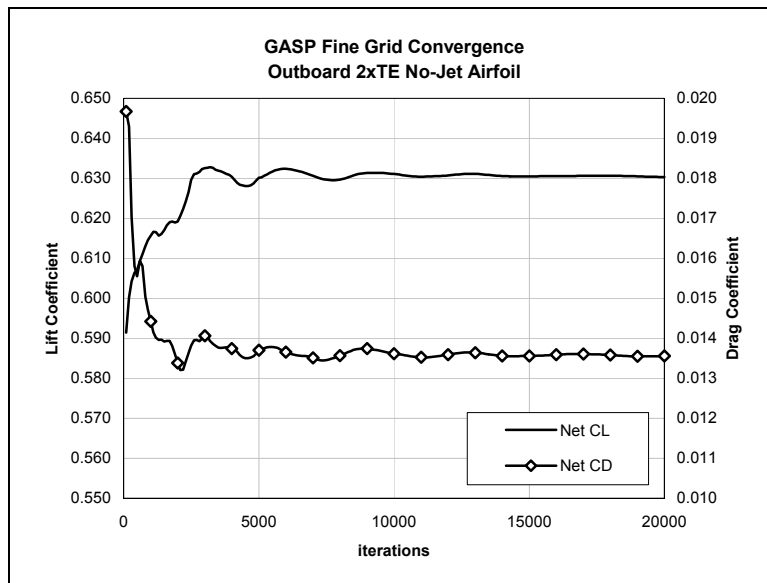


Figure 3.50: Fine grid convergence typical of outboard airfoils.

3.4.2.8. Post Processing

Two forms of data output from GASP were used during this research project: the forces and moment from the pressures and shear stresses integrated over the airfoil and trailing edge surfaces; and the flowfield properties. The integrated forces and moments on the airfoil surface and trailing edge surface (surfaces 4 and 5 in Figure 3.40) were output every 100 iterations. The forces and moments written to the output file included:

- Fx_Total , Fy_Total : the summation of pressure and viscous forces in the x- and y-directions
- Fx_Inv , Fy_Inv : the summation of pressure forces in the x- and y-directions
- Fx_Vis , Fy_Vis : the summation of viscous forces in the x- and y-directions
- $Thrust_x$, $Thrust_y$: the summation of the pressure, viscous, and momentum flux forces in the x- and y-directions
- Mz_Total : the moment due to pressure and viscous forces about $\frac{x}{c} = 25\%$
- Mz_Inv : the moment due to pressure forces about $\frac{x}{c} = 25\%$
- Mz_Vis : the moment due to viscous forces about $\frac{x}{c} = 25\%$
- Mz_Thrust : the moment due to pressure, viscous, and momentum flux forces about $\frac{x}{c} = 25\%$

Writing the forces and moments to the output files every 100 iterations made it possible to track the convergence of a solution in GASP. The procedure used to compute the

force and moment coefficients is explained later. The flowfield properties were also output from GASP every 100 iterations. At each grid point, GASP output the following quantities:

- x, y : the grid point coordinates
- M : the Mach number
- u, v : the velocity components
- p, T, ρ, C_p : the pressure, temperature, density, and pressure coefficient
- TKE : the turbulent kinetic energy
- ω : the turbulence frequency

The flowfield data was loaded into *Tecplot* to be further analyzed. From *Tecplot*, data such as the surface pressure distribution or the wake velocity profile could be extracted. Furthermore, contour plots and streamline plots could also be made.

3.4.3. Calculating Force Coefficients

When performing a CFD analysis on an airfoil or a two-dimensional jet-wing in GASP, the problem is set-up as shown in Figure 3.51. The airfoil chord line is oriented in a horizontal direction; it is aligned with the x-axis of the grid coordinate system. The freestream flow is applied as a velocity vector U_∞ , oriented at an angle α , which is the angle of attack. The jet, when applied, exits the trailing edge at an angle τ with respect to the chord line, at a velocity U_{jet} . When the lift and drag are calculated, they are aligned with a coordinate system rotated by an angle equal to α from the x- and y-axes of the grid coordinate system.

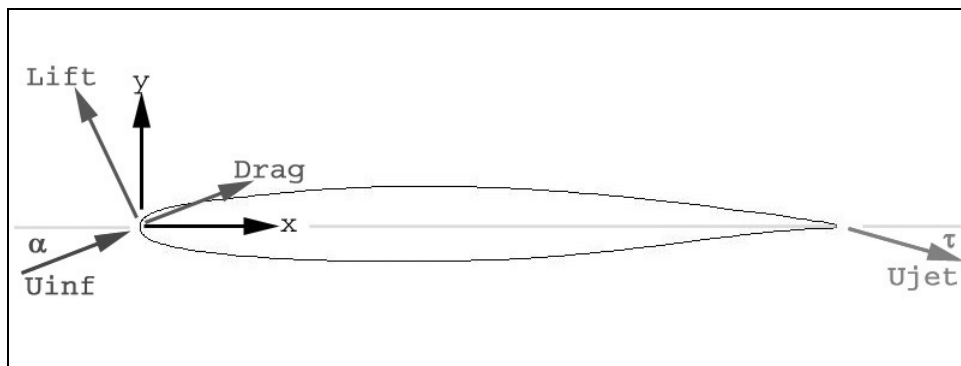


Figure 3.51: Orientation of jet-wing in GASP.

A two-zone C-grid (illustrated in Figure 3.33) was used to model this airfoil because of the thick trailing edge. One zone includes the thin area extending

downstream of the thick trailing edge, and the second zone includes the rest of the computational domain. When the forces are computed for these two zones, the “TE” subscript will denote forces on the blunt trailing edge (such as base drag), and “Surf” subscript will denote forces on the rest of the airfoil surface.

The postprocessor of GASP can compute force quantities integrated over a defined surface. The four force quantities of interest are Fx_Total , Fy_Total , $Thrust_x$, and $Thrust_y$, which are computed from the pressure and viscous forces integrated over the element faces on the surface of the airfoil and trailing edge. The Fx_Total and Fy_Total forces are simply the x- and y-components of sum of all the pressure and viscous forces. This can be written in the following set of equations:

$$\begin{aligned} Fx_Total &= \sum \left[\left(\vec{F}_{pressure} + \vec{F}_{viscous} \right) \cdot \hat{i} \right] \\ Fy_Total &= \sum \left[\left(\vec{F}_{pressure} + \vec{F}_{viscous} \right) \cdot \hat{j} \right] \end{aligned} \quad (3.16)$$

The vectors \hat{i} and \hat{j} are unit vectors in the x- and y-directions, respectively. The $Thrust_x$ and $Thrust_y$ forces, in addition to including the summed pressure and viscous force, also included forces due to momentum flux if there is a flow through the surface, as with a jet.

$$\begin{aligned} Thrust_x &= \sum \left[\left(\vec{F}_{pressure} + \vec{F}_{viscous} + \vec{F}_{momentumflux} \right) \cdot \hat{i} \right] \\ Thrust_y &= \sum \left[\left(\vec{F}_{pressure} + \vec{F}_{viscous} + \vec{F}_{momentumflux} \right) \cdot \hat{j} \right] \end{aligned} \quad (3.17)$$

In most of the computational domain, $Thrust_x$ and $Thrust_y$ are equal to Fx_Total and Fy_Total , respectively. The only place that these forces due to momentum flux do appear is wherever a jet is present. A jet can be placed at the trailing edge or any other surface along the airfoil. The jet adds mass and momentum to the flow, and this creates a force at the trailing edge surface. Thus, the thrust from the jet, as given by GASP, is:

$$Thrust_{GASP} = \sqrt{\left[(Thrust_x_{surf} - Fx_Total_{surf}) + (Thrust_x_{TE} - Fx_Total_{TE}) \right]^2 + \left[(Thrust_y_{surf} - Fy_Total_{surf}) + (Thrust_y_{TE} - Fy_Total_{TE}) \right]^2} \quad (3.18)$$

However, this calculation of jet thrust is not entirely complete. It is well known that the thrust from a jet is given by the equation:

$$Thrust_{jet} = \dot{m}_{jet} \cdot (U_{jet} - U_{\infty}) + (p_{jet} - p_{\infty}) \cdot (b_{jet} \cdot h_{jet}) \quad (3.19)$$

In Equation (3.19), b_{jet} is the span of the jet. The thrust in Equation (3.19) depends on the jet velocity, U_{jet} , and the inlet velocity, which is typically the freestream velocity,

U_∞ . In the CFD jet-wing model, GASP calculates the thrust as $\dot{m}_{jet} \cdot U_{jet}$. With the $\dot{m}_{jet} \cdot U_\infty$ term missing, the jet becomes a rocket. To account for the missing information, this term must be included in the thrust calculated by GASP:

$$\begin{aligned} \dot{m}_{jet} \cdot U_\infty &= b_{jet} \cdot h_{jet} \cdot \rho_{jet} \cdot U_{jet} \cdot U_\infty \\ Thrust_{jet} &= Thrust_{GASP} - b_{jet} \cdot h_{jet} \cdot \rho_{jet} \cdot U_{jet} \cdot U_\infty \end{aligned} \quad (3.20)$$

Two sets of lift and drag forces can be calculated: one set due to the airfoil alone, without the jet; and one set due to the airfoil and the jet. The lift and drag forces from the airfoil alone are calculated as follows:

$$\begin{aligned} L &= -(Fx_{Total_{surf}} + Fx_{Total_{TE}}) \cdot \sin(\alpha) + (Fy_{Total_{surf}} + Fy_{Total_{TE}}) \cdot \cos(\alpha) \\ D &= (Fx_{Total_{surf}} + Fx_{Total_{TE}}) \cdot \cos(\alpha) + (Fy_{Total_{surf}} + Fy_{Total_{TE}}) \cdot \sin(\alpha) \end{aligned} \quad (3.21)$$

The respective coefficients are then calculated:

$$\begin{aligned} C_L &= \frac{L}{\frac{1}{2} \cdot \rho_\infty \cdot U_\infty^2 \cdot c \cdot b} \\ C_D &= \frac{D}{\frac{1}{2} \cdot \rho_\infty \cdot U_\infty^2 \cdot c \cdot b} \end{aligned} \quad (3.22)$$

The lift and drag forces which include the jet thrust are computed:

$$\begin{aligned} L_{Net} &= -(Thrust_{x_{surf}} + Thrust_{x_{TE}}) \cdot \sin(\alpha) + (Thrust_{y_{surf}} + Thrust_{y_{TE}}) \cdot \cos(\alpha) \dots \\ &\quad + (b_{jet} \cdot h_{jet} \cdot \rho_{jet} \cdot U_{jet} \cdot U_\infty) \cdot \sin(\alpha + \tau) \\ D_{Net} &= (Thrust_{x_{surf}} + Thrust_{x_{TE}}) \cdot \cos(\alpha) + (Thrust_{y_{surf}} + Thrust_{y_{TE}}) \cdot \sin(\alpha) \dots \\ &\quad + (b_{jet} \cdot h_{jet} \cdot \rho_{jet} \cdot U_{jet} \cdot U_\infty) \cdot \cos(\alpha + \tau) \end{aligned} \quad (3.23)$$

A negative D_{Net} term indicates a positive thrust into the freestream flow. For a self-propelled jet-wing, D_{Net} equals zero. Note that the $b_{jet} \cdot h_{jet} \cdot \rho_{jet} \cdot U_{jet} \cdot U_\infty$ term has been included in Equation (3.23) to give the correct thrust. The total lift coefficient, $C_{L_{Net}}$, and the net drag coefficient, $C_{D_{Net}}$, are computed from:

$$\begin{aligned} C_{L_{Net}} &= \frac{L_{Net}}{\frac{1}{2} \cdot \rho_\infty \cdot U_\infty^2 \cdot c \cdot b} \\ C_{D_{Net}} &= \frac{D_{Net}}{\frac{1}{2} \cdot \rho_\infty \cdot U_\infty^2 \cdot c \cdot b} \end{aligned} \quad (3.24)$$

Chapter 4. Computational Results

Two sets of results for the CFD study will be presented. First, results will be presented for representative airfoil models at simulated BWB cruise Mach number and Reynolds number conditions. All three airfoil models - Outboard 1xTE, Outboard 2xTE, and Inboard - were modeled at these conditions, with and without the jet-wing. Second, a set of computations was completed for the Outboard 1xTE at a lower Reynolds number, $Re_c = 5.67e6$. These results, while they cannot be applied to a BWB at cruise, could be applied to typical UAV-size aircraft.

4.1. Jet-Wing Studies for BWB at Cruise

As the CFD simulations were run, one of the first “problems” encountered was that the lift coefficient from the GASP model did not closely match the lift coefficient from MSES at the same angle of attack. This was indeed a problem because it meant that MSES could not be used to predict the GASP results with a high degree of accuracy. And, it would be favorable to be able to use MSES to design airfoils for the GASP studies within some small amount of error, because it takes less than 5 minutes to run an airfoil case in MSES on an SGI O2 machine, while it takes two to three days to run an airfoil case in GASP on an SGI Origin 2000 machine using eight processors. As per Table 3.2, the design lift coefficient was $C_L = 0.69$ for the Outboard airfoils. MSES predicted that an angle of attack of $\alpha = 2.66^\circ$ would result in this lift coefficient for the Outboard 1xTE airfoil. When this airfoil was run in GASP with $\alpha = 2.66^\circ$, the resulting lift coefficient of $C_L = 0.628$ was 9% lower than design. This difference in the lift can be observed in the pressure distributions shown in Figure 4.1, primarily in the difference in predicted shock locations. However, when both MSES and GASP are run for the same lift coefficient, $C_L = 0.628$, the pressure distributions differ by only a small amount, as seen in Figure

4.2. Because these are only representative models being used for parametric studies to predict trends when modeling jet-wings, it was concluded that the lift coefficient of $C_L = 0.628$ was close enough. For the Inboard airfoil, the target lift coefficient was $C_L = 0.30$ (see Table 3.2). While the GASP solution of the Inboard jet-wing airfoil at $C_{L_{Net}} = 0.269$ came close to the target lift coefficient of $C_L = 0.30$, the GASP solution of the Inboard no-jet airfoil of $C_L = 0.069$ was much lower than the target of $C_L = 0.30$.

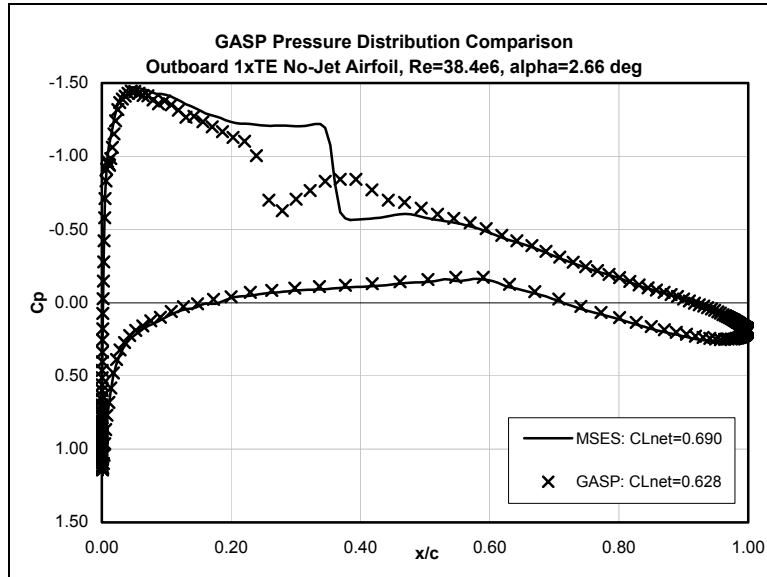


Figure 4.1: Comparison of GASP and MSES pressure distributions for Outboard 1xTE airfoil at $\alpha = 2.66^\circ$.

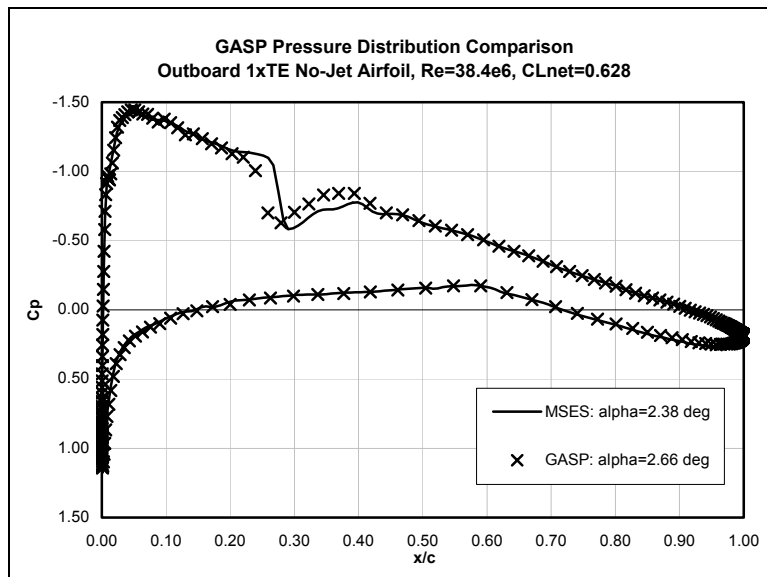


Figure 4.2: Comparison of GASP and MSES pressure distributions for Outboard 1xTE airfoil at $C_L = 0.628$.

4.1.1. Outboard 1xTE Jet-Wing Airfoil Results

First, the Outboard 1xTE airfoil was run in GASP without a jet. The resulting drag coefficient, $C_D = 0.0124$, and pressure at the trailing edge, $p_{TE} = 25474 \frac{\text{N}}{\text{m}^2}$, were then used to predict the jet flow Mach number, $M_{jet} = 1.199$, and density, $\rho_{jet} = 0.4054 \frac{\text{kg}}{\text{m}^3}$, required to produce a self-propelled jet-wing. Using Equation (4.1), the propulsive efficiency of the Outboard 1xTE jet-wing airfoil is $\eta_P = 75.1\%$.

$$\eta_P = \frac{2}{1 + \frac{U_{jet}}{U_\infty}} \quad (4.1)$$

It was found necessary to increase the angle of attack to $\alpha = 2.75^\circ$ to obtain the net lift coefficient. The resulting force coefficients and pressure distributions for the no-jet and jet-wing Outboard 1xTE airfoil are shown in Table 4.1 and Figure 4.3, respectively. It should be noted that it was necessary to increase the angle of attack by a small amount in order to compare the no-jet and jet-wing airfoils at the same net lift coefficient. As can be observed in the Figure 4.3, the pressure distributions for the no-jet and jet-wing case at the same lift coefficient are nearly identical, even at the shock. Figure 4.4 shows the velocity profile 1% downstream of the airfoil. This helps to show why the propulsive efficiency is a bit low ($\eta_P = 75.1\%$) compared to typical high-bypass-ratio turbofan engine aircraft ($\eta_{P_{typical}} = 80\%$). The jet is rather thin ($\frac{h_{jet}}{c} = 0.49\%$) and does not do a good job of 'filling in' the wake behind the airfoil, and the jet velocity is much greater than the freestream velocity. Figure 4.5 shows the streamlines at the trailing edge of the Outboard 1xTE no-jet airfoil. It can be seen that a complex vortex forms on the trailing edge base when no jet is present. The flowfield at the trailing edge of the Outboard 1xTE jet-wing airfoil is pictured in Figure 4.6. The jet-wing fills in the flow on the trailing edge base, and no vortex is present. Looking at the pressure contours at the trailing edge in Figure 4.7, it can be seen that weak shocks and expansions do form in the jet. Therefore, it may be necessary further iterate and try to better match the pressure of the jet and with that of the flow at the trailing edge. Still, it can be said that this is one of those rare cases when adding something to a flow problem actually simplifies the flowfield.

Table 4.1: Outboard 1xTE no-jet and jet-wing airfoil results for $C_{L_{Net}} = 0.628$.

Airfoil	Outboard 1xTE, no-jet	Outboard 1xTE, jet-wing
Angle-of-attack, α	2.66°	2.75°
Jet Mach number, M_{jet}	0.000	1.199
Propulsive efficiency, η_P	--	75.1%
Lift coefficient, C_L	0.6276	0.6208
Drag coefficient, C_D	0.0124	0.0117
Jet coefficient, C_J	0.0000	0.0115
Net lift coefficient, $C_{L_{Net}}$	0.6276	0.6230
Net drag coefficient, $C_{D_{Net}}$	0.0124	0.0002

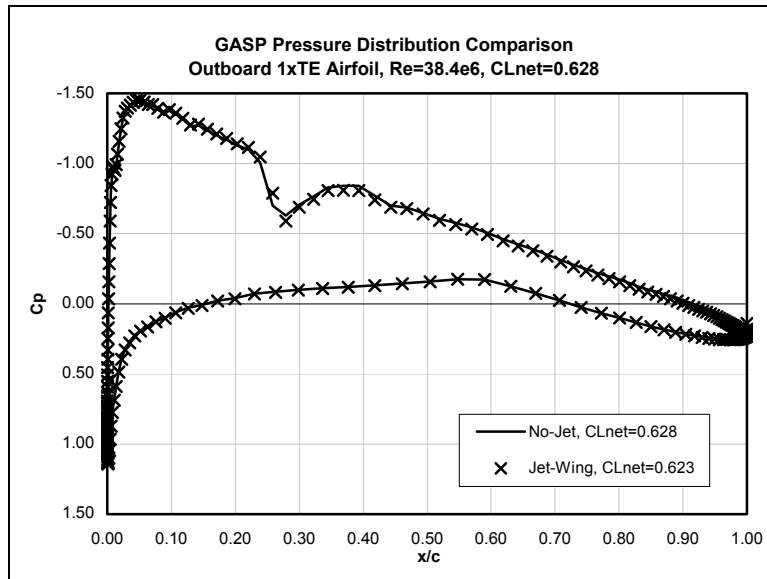


Figure 4.3: Outboard 1xTE no-jet and jet-wing airfoil pressure distributions for $C_{L_{Net}} = 0.628$.

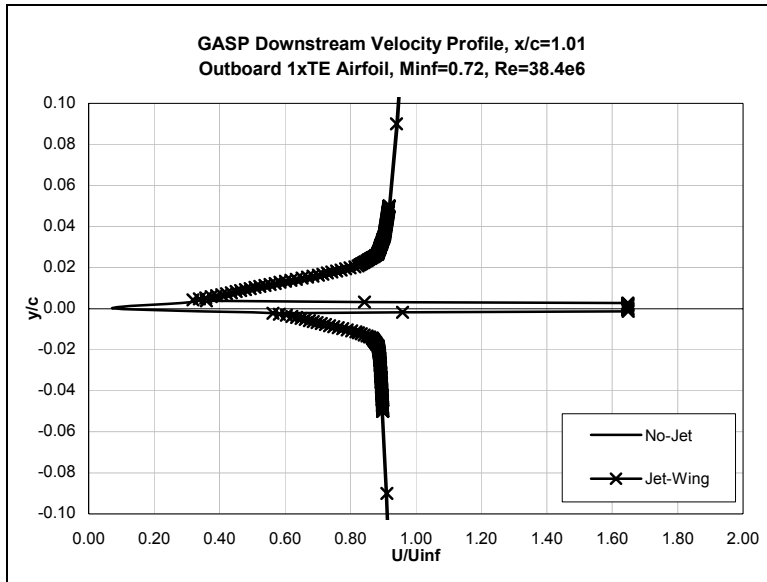


Figure 4.4: Velocity profile downstream of Outboard 1xTE no-jet and jet-wing airfoils, $x/c=1.01$.

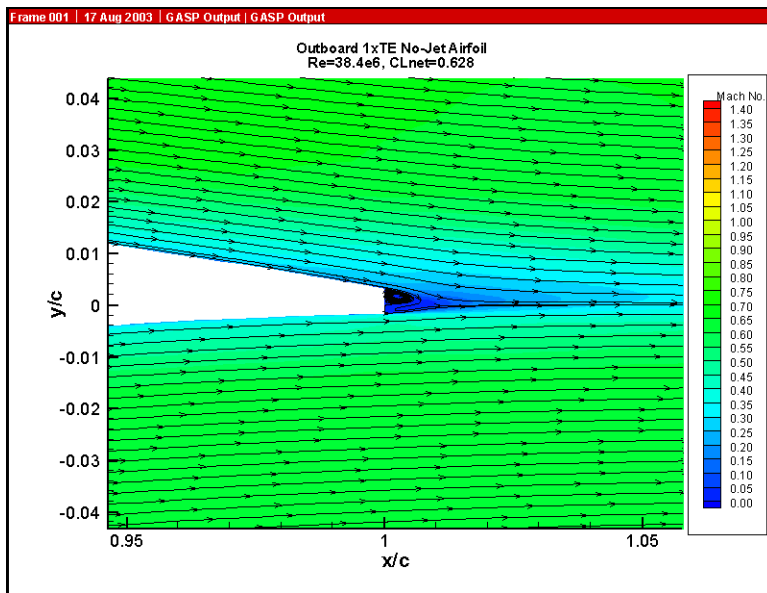


Figure 4.5: Streamlines and Mach number contours at trailing edge of Outboard 1xTE no-jet airfoil.

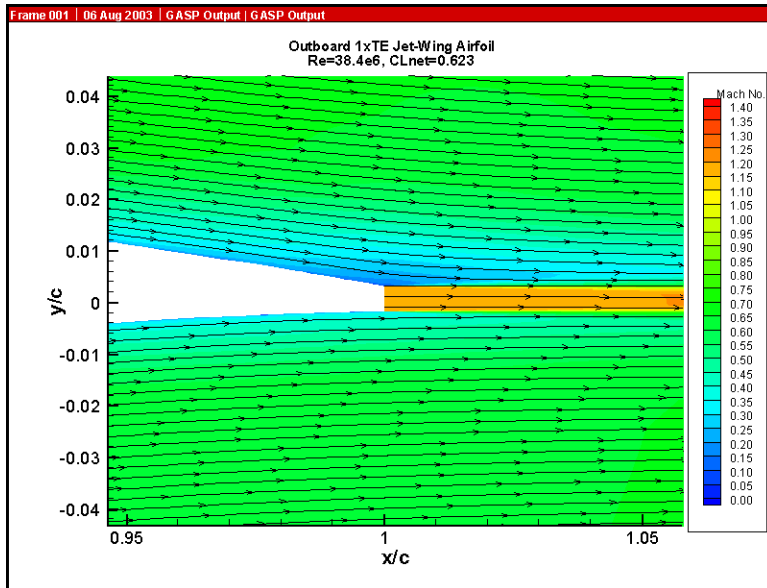


Figure 4.6: Streamlines and Mach number contours at trailing edge of Outboard 1xTE jet-wing airfoil.

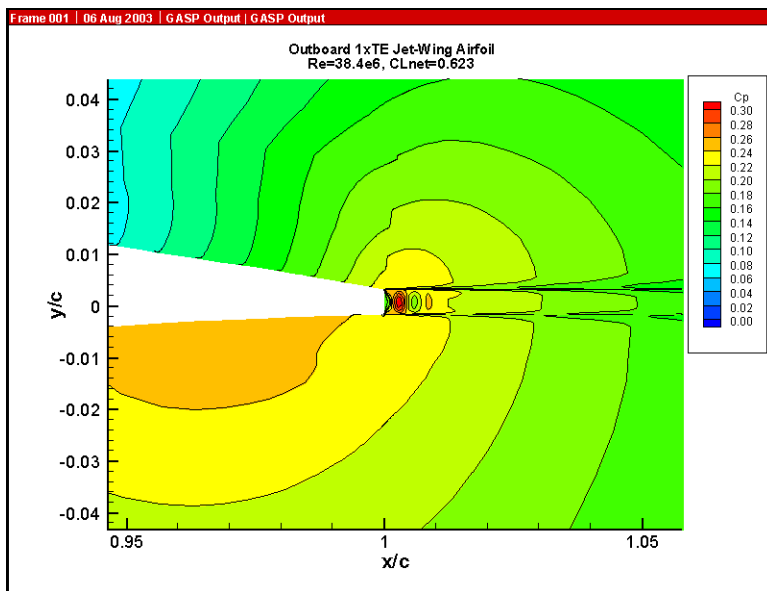


Figure 4.7: Pressure contours at the trailing edge of the Outboard 1xTE jet-wing airfoil.

4.1.2. Outboard 2xTE No-Jet Airfoil Results

The next airfoil case studied was the Outboard 2xTE no-jet airfoil. It is important to determine how this expanded trailing edge performs. To acquire a lift coefficient similar to the Outboard 1xTE no-jet lift coefficient of $C_{L_{Net}} = 0.628$, it was necessary to increase the angle of attack of the Outboard 2xTE no-jet airfoil to $\alpha = 3.0^\circ$. The resulting lift coefficient of $C_{L_{Net}} = 0.6303$ is within 0.4% of the test lift coefficient. From a comparison of the force coefficients presented in Table 4.2, it is noted that the drag of the

Outboard 2xTE airfoil increases by 9.7% over the Outboard 1xTE airfoil. Although the net lift coefficients vary by only a small amount, the pressure distribution of the Outboard 2xTE airfoil, plotted in Figure 4.8, differs significantly from that of the Outboard 1xTE airfoil. It is observed that the shock forms at about $\frac{x}{c} = 28\%$, which is nearly 4% aft where the shock forms on the Outboard 1xTE no-jet airfoil. Also, the pressures at the trailing edge differ by a small amount. The flowfield near the trailing edge of the Outboard 2xTE no-jet airfoil is pictured in Figure 4.9. When compared to the flowfield at the trailing edge of the Outboard 1xTE no-jet airfoil in Figure 4.5, it is noted that much larger vortex structures form on the trailing edge base of the Outboard 2xTE airfoil.

Table 4.2: Outboard 1xTE and Outboard 2xTE no-jet airfoil results for $C_{L_{Net}} = 0.628$.

Airfoil	Outboard 1xTE, no-jet	Outboard 2xTE, No-jet
Angle-of-attack, α	2.66°	3.00°
Lift coefficient, C_L	0.6276	0.6303
Drag coefficient, C_D	0.0124	0.0136
Net lift coefficient, $C_{L_{Net}}$	0.6276	0.6303

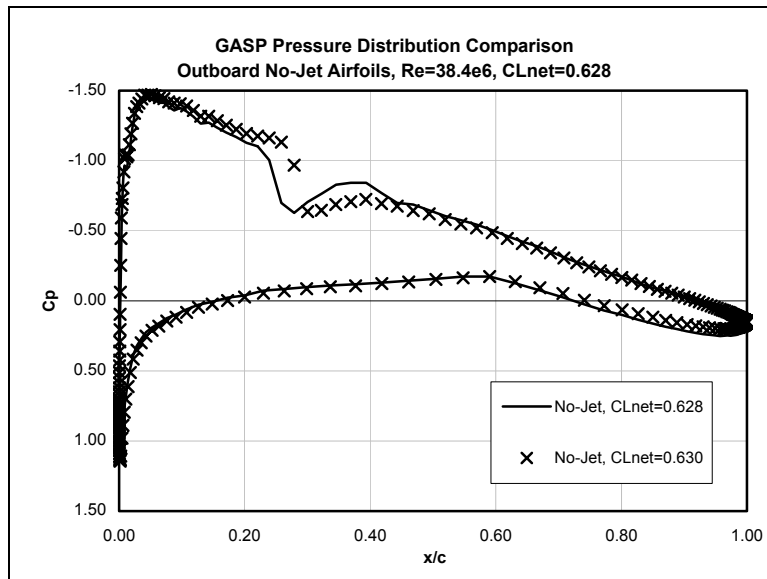


Figure 4.8: Outboard 1xTE and Outboard 2xTE no-jet airfoil pressure distributions for $C_{L_{Net}} = 0.628$.

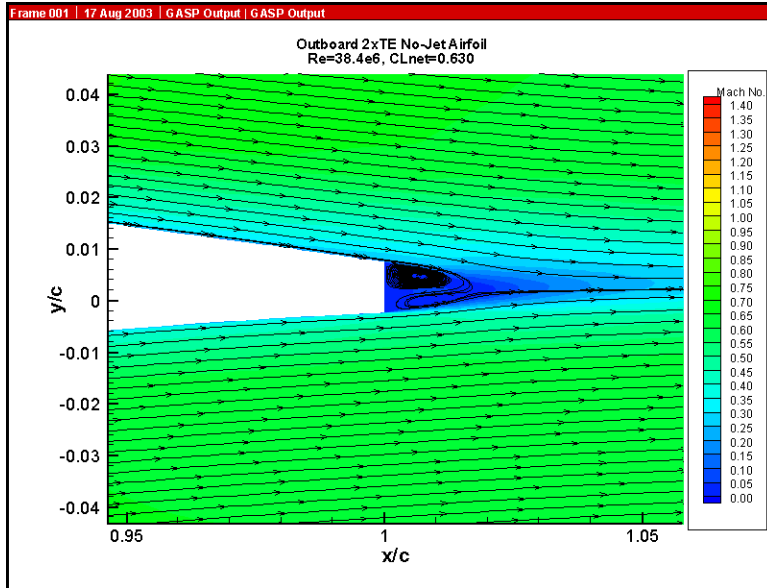


Figure 4.9: Streamlines and Mach number contours at trailing edge of Outboard 2xTE no-jet airfoil.

The question arises, “Why is the drag of the Outboard 2xTE airfoil nearly 10% larger than that of the Outboard 1xTE airfoil?” The breakdown of the individual drag components for the Outboard 1xTE and 2xTE airfoils is presented in Table 4.3. It is observed that the viscous drag components are equal and the difference in drag is from the inviscid drag components: $\Delta C_{D_{inv}} = 0.0011$. One might suppose that this drag difference can be found on the larger trailing edge base of the Outboard 2xTE. However the inviscid drag force on the trailing edge base of both airfoils is actually a thrust force, and this thrust force is significantly larger on the Outboard 2xTE airfoil. This thrust is confirmed by the positive pressure coefficient C_p throughout the pressure distribution on the trailing edge base of both airfoils, as shown in Figure 4.10. Integrating over the trailing edge, the average values of pressure on the trailing edge bases are found to be $(p_{TE})_{1xTE} = 25508 \text{ N/m}^2$ and $(p_{TE})_{2xTE} = 25214 \text{ N/m}^2$. With trailing edge heights of $(h_{TE})_{1xTE} = 0.0332 \text{ m}$ and $(h_{TE})_{2xTE} = 0.0663 \text{ m}$, and a span of $b = 6.77 \text{ m}$, Equation (4.2) is used to find the force acting upon the trailing edge base of each airfoil.

$$F_{TE} = p_{TE} \cdot h_{TE} \cdot b \cdot \cos(\alpha)$$

$$C_{F_{TE}} = \frac{F_{TE}}{\frac{1}{2} \cdot (h_{TE} \cdot b) \cdot \rho_{\infty} \cdot U_{\infty}^2} \quad (4.2)$$

Since the pressure is acting *into* the trailing edge base of each airfoil, the resulting force acts in the direction of thrust, and not the direction of drag. The resulting drag

coefficients due to inviscid forces on the trailing edge are $(C_{D_{inv}})_{TE_{1xTE}} = -0.0143$ and $(C_{D_{inv}})_{TE_{2xTE}} = -0.0284$ for the Outboard 1xTE and 2xTE airfoils. These values are exactly what GASP calculated, which should come as no surprise. The key to the higher inviscid drag of the Outboard 2xTE airfoil is that the thicker trailing edge influences the circulation around the entire airfoil and gives the airfoil a higher overall form drag (note the larger value of the inviscid drag on the airfoil surface in Table 4.3). This larger form drag is observed in downstream velocity profiles, which are compared in Figure 4.11. The Outboard 2xTE no-jet airfoil has a significantly larger wake than the Outboard 1xTE no-jet airfoil, which translates to a larger momentum deficit and increased drag. So, it can be concluded it is possible to expand the trailing edge of an airfoil in an attempt to increase propulsive efficiency in a jet-wing configuration, however there is a significant drag penalty for this expanding trailing edge airfoil.

Table 4.3: Outboard 1xTE and Outboard 2xTE no-jet airfoil drag breakdown.

Airfoil	Outboard 1xTE, no-jet	Outboard 2xTE, No-jet
Total drag coefficient, C_D	0.0124	0.0136
Drag coefficient from viscous forces, $C_{D_{vis}}$	0.0050	0.0050
Drag coefficient from inviscid forces (pressure, wave), $C_{D_{inv}}$	0.0075	0.0086
Drag coefficient from inviscid forces on trailing edge, $(C_{D_{inv}})_{TE}$	-0.0143	-0.0284
Drag coefficient from inviscid forces on airfoil not including trailing edge, $(C_{D_{inv}})_{surf}$	0.0218	0.0370

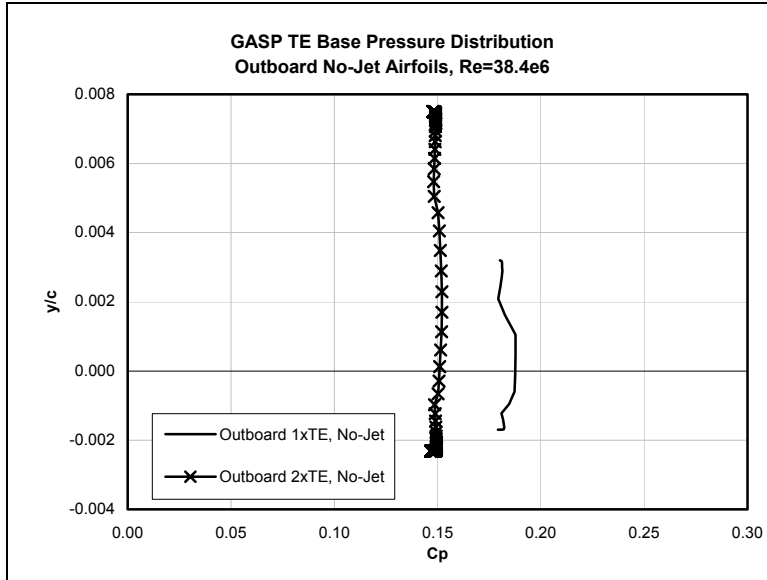


Figure 4.10: Comparison of GASP pressure distribution on trailing edge base of Outboard 1xTE and 2xTE no-jet airfoils.

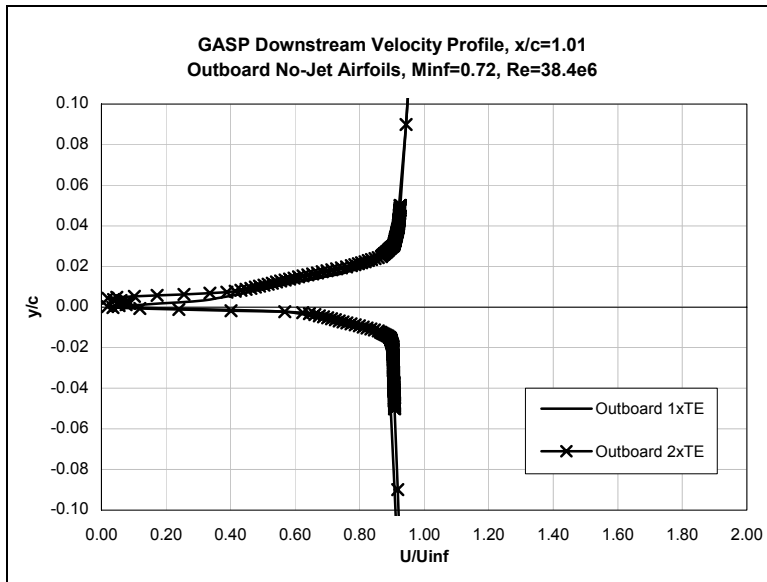


Figure 4.11: Velocity profile downstream of Outboard 1xTE and Outboard 2xTE no-jet airfoils.

4.1.3. Outboard 2xTE Jet-Wing Airfoil Results

Using the drag coefficient $C_D = 0.0136$ and the averaged pressure at the trailing edge, $p_{TE} = 25191 \text{ N/m}^2$ from the Outboard 2xTE no-jet airfoil, a jet flow Mach number of $M_{jet} = 1.021$, and density of $\rho_{jet} = 0.4009 \text{ kg/m}^3$ were calculated to produce a self-propelled jet-wing. The propulsive efficiency of this Outboard 2xTE jet-wing airfoil, calculated by Equation (4.1), is $\eta_p = 82.8\%$. As with the Outboard 1xTE jet-wing airfoil,

it was necessary to increase the angle of attack of the Outboard 2xTE jet-wing airfoil a small amount to $\alpha = 3.13^\circ$ to produce the same net lift. The resulting force coefficients are found in Table 4.4. The pressure distribution is pictured in Figure 4.12. As with the Outboard 1xTE airfoil, the presence of the jet-wing has a minimal effect on the pressure distribution, moving the shock aft by about 1% of the chord. The downstream velocity profiles in Figure 4.13 and Figure 4.14 help to visually show why the propulsive efficiency has been increased. The Outboard 2xTE jet-wing is thicker ($\frac{h_{jet}}{c} = 0.98\%$) and has a lower speed than the Outboard 1xTE jet-wing, thus allowing it to better ‘fill in’ the wake behind the airfoil. The complex double-vortex structure on the trailing edge base of the Outboard 2xTE no-jet airfoil (see Figure 4.9) is eliminated by the jet, which is shown in Figure 4.15. Furthermore, Figure 4.16 shows that the Outboard 2xTE jet-wing airfoil does not suffer the same shock and expansion structure as the Outboard 1xTE jet-wing airfoil (Figure 4.7).

Table 4.4: Outboard 2xTE no-jet and jet-wing airfoil results for $C_{L_{Net}} = 0.628$.

Airfoil	Outboard 2xTE, no-jet	Outboard 2xTE, jet-wing
Angle-of-attack, α	3.00°	3.13°
Jet Mach number, M_{jet}	0.000	1.021
Propulsive efficiency, η_p	--	82.8%
Lift coefficient, C_L	0.6276	0.6350
Drag coefficient, C_D	0.0136	0.0121
Jet coefficient, C_J	0.0000	0.122
Net lift coefficient, $C_{L_{Net}}$	0.6276	0.6389
Net drag coefficient, $C_{D_{Net}}$	0.0124	0.0000

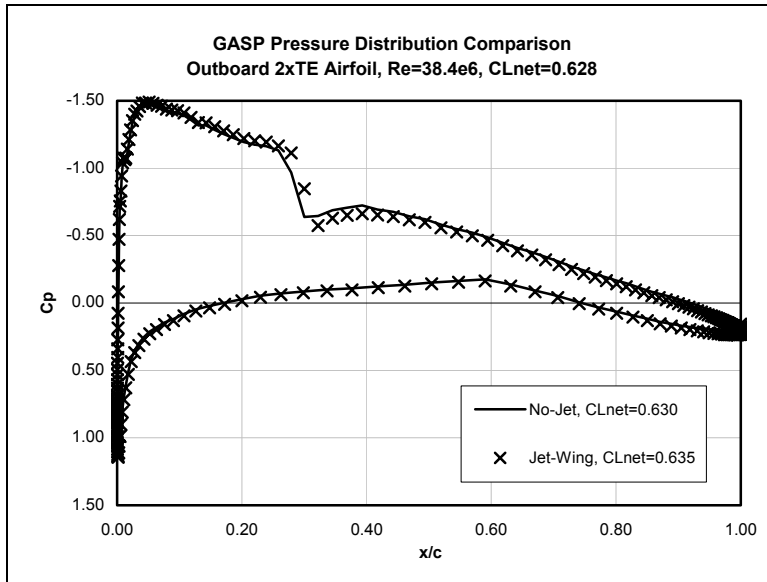


Figure 4.12: Outboard 2xTE no-jet and jet-wing airfoil pressure distributions for $C_{L_{Net}} = 0.628$.

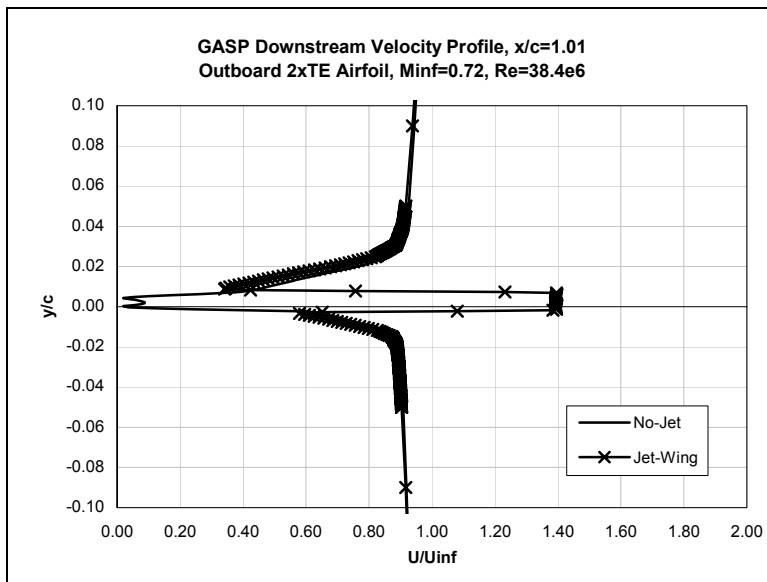


Figure 4.13: Velocity profile downstream of Outboard 2xTE no-jet and jet-wing airfoils.

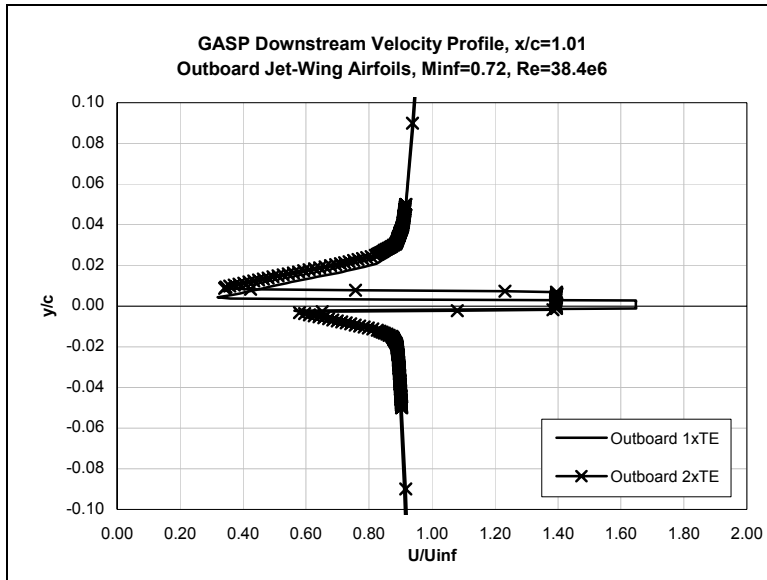


Figure 4.14: Velocity profile downstream of Outboard 1xTE and Outboard 2xTE jet-wing airfoils.

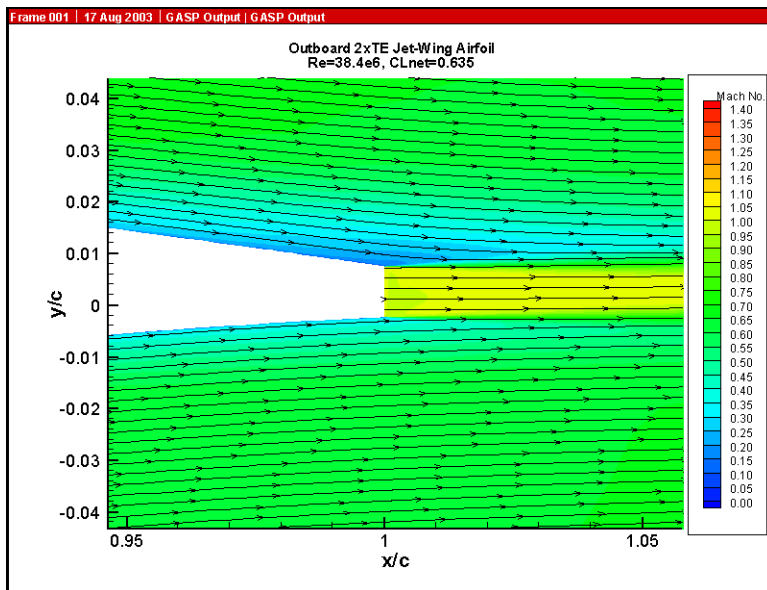


Figure 4.15: Streamlines and Mach number contours at trailing edge of Outboard 2xTE jet-wing airfoil.

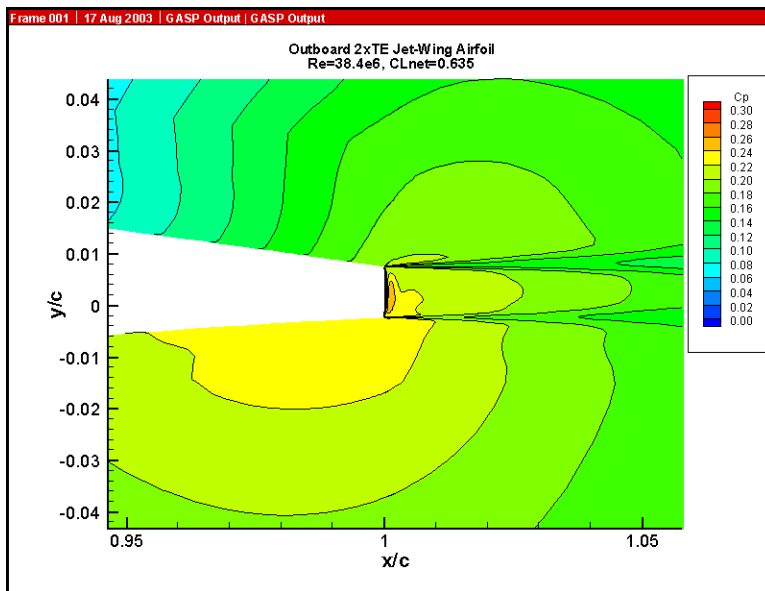


Figure 4.16: Pressure contours at the trailing edge of the Outboard 2xTE jet-wing airfoil.

For an airfoil of moderate thickness, when the trailing edge (and jet height) is expanded by a factor of two, the propulsive efficiency increases by 7.5%. Furthermore, the propulsive efficiency of $\eta_p = 82.8\%$ is greater than that of typical high-bypass ratio turbofan aircraft ($\eta_{p_{typical}} = 80\%$). However, the drag on the airfoil for the no-jet cases also increases substantially (nearly 10%) when the trailing edge thickness is doubled. This would be a problem for an engine-out situation. Therefore, expanding the trailing edge height cannot simply be done arbitrarily, and the cost of the increased drag when the jet-wing is off must outweigh the performance gains of increased propulsive efficiency.

4.1.4. Inboard No-Jet Airfoil Results

The Inboard airfoil cases were more difficult to converge than the Outboard airfoil cases. Using the Hybrid grid, an apparently periodic solution was found for the Inboard no-jet airfoil. As can be seen in Figure 4.17, the net lift coefficient oscillates between $C_{L_{Net}} = 0.032$ and $C_{L_{Net}} = 0.106$. Two approaches that could be used to eliminate the oscillations include running the solution until the oscillations in the net lift coefficient damp out, and computing the time-accurate solution of the Inboard airfoil problem. While either of these approaches could work, it was determined not to proceed with them because each presented its own problems. The first approach could be very computationally expensive, even if the oscillations ever damp out. The latter approach is beyond the scope of this parametric study, which is just trying to find performance trends associated with jet-wing distributed propulsion. Therefore, the

apparently periodic solution of the Inboard no-jet airfoil will be analyzed by looking at the solutions at the “peaks” and “valleys” of the lift coefficient convergence history (Figure 4.17).

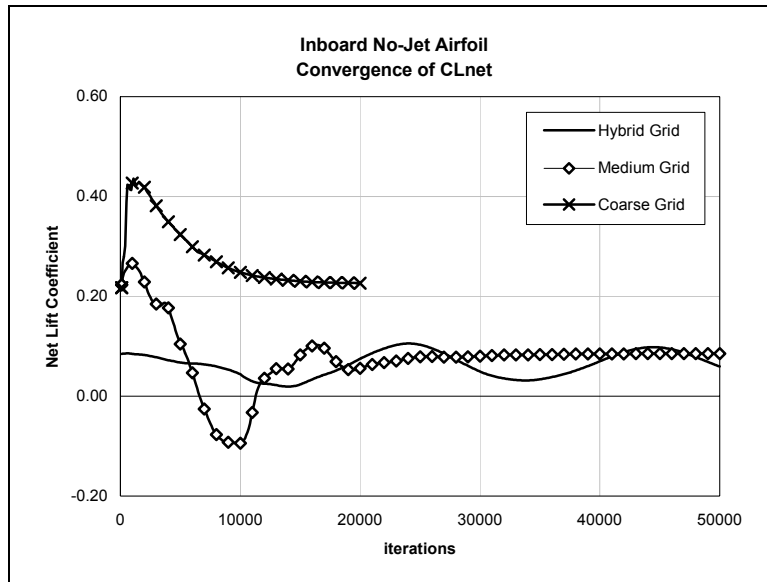


Figure 4.17: Inboard no-jet airfoil convergence history using Hybrid Grid.

The force coefficients of the peak and valley solutions are tabulated in Table 4.5. It is quickly noted that the average lift coefficient of $C_L = 0.069$ is 77% less the target lift coefficient of $C_L = 0.30$. The reason can be observed in the pressure distributions plotted in Figure 4.18. Both GASP solutions predict the lower surface shock over 10% further aft and the upper surface shock about 7% further forward than the MSES solution, and this results in a negative lift (or down force) acting on the aft 50% of the airfoil. One reason that the GASP pressure distributions and lift coefficients are so much different than the those of the MSES solution is because the GASP solutions predict a significant region of separated flow on the aft portion of the airfoil. The plot of the upper surface skin friction in Figure 4.19, shows that the GASP solutions predict negative values of skin friction (and therefore separation) at $\frac{x}{c} = 88\%$, while the MSES solution predicts that the flow will remain attached over the entire airfoil. For the GASP peak and valley solutions, the flow over the airfoil is shown in Figure 4.20. The region of separated flow is observed in Figure 4.21.

Table 4.5: Inboard no-jet airfoil results.

Airfoil	Inboard no-jet "Peak"	Inboard no-jet "Valley"	Inboard no-jet Average
Angle-of-attack, α	2.00°	2.00°	2.00°
Lift coefficient, C_L	0.1056	0.0315	0.0685
Drag coefficient, C_D	0.0277	0.0269	0.0273
Net lift coefficient, $C_{L_{Net}}$	0.1056	0.0315	0.0685

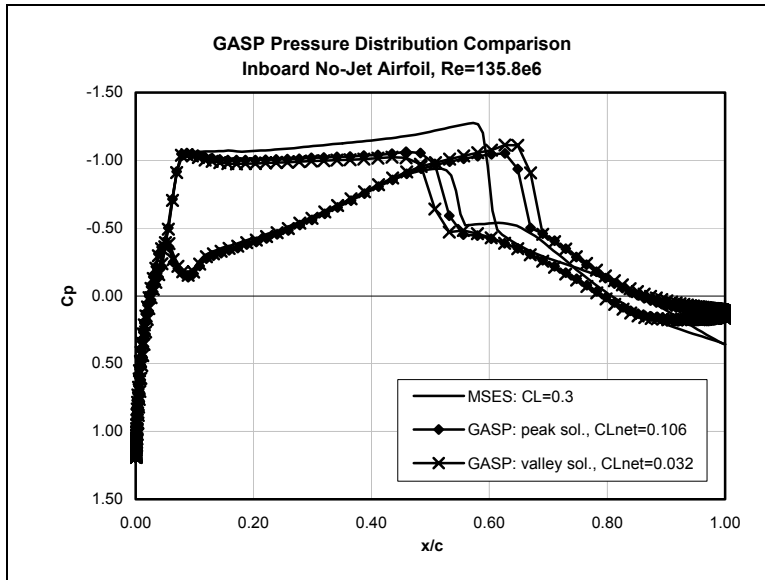


Figure 4.18: Inboard no-jet airfoil GASP "peak" and "valley" and MSES solutions of pressure distributions.

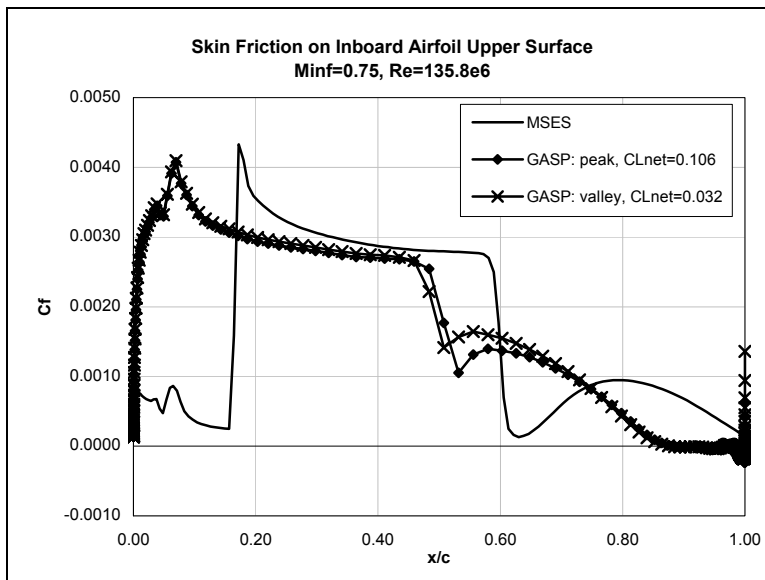


Figure 4.19: Inboard no-jet airfoil GASP "peak" and "valley" and MSES solutions of upper surface skin friction.

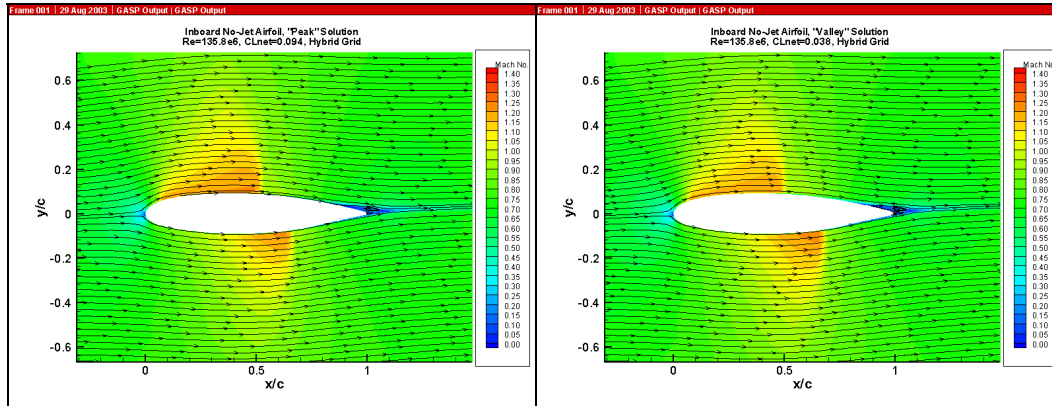


Figure 4.20: Streamlines and Mach number contours around Inboard no-jet airfoil.

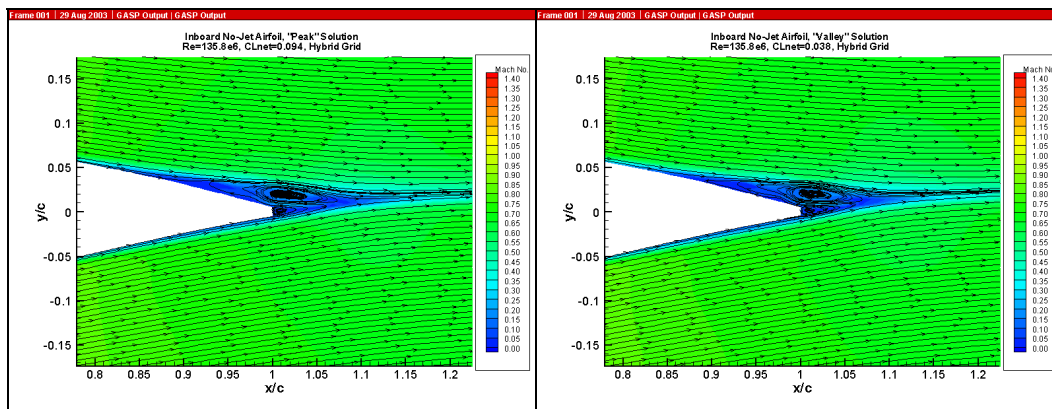


Figure 4.21: Streamlines and Mach number contours near trailing edge of Inboard no-jet airfoil. Note region of separated flow.

The variance in the results from the Inboard no-jet airfoil case shows that this is a rather complex flow and that the Inboard airfoil may be a poor design. First, the presence of shocks on both surfaces of the airfoil and the prediction of a region of separated flow by GASP (but not by MSES) show that the flow around the thicker Inboard airfoil is more complex than the flow around the Outboard airfoils, for which GASP and MSES predicted a shock only on the upper surface and no region of separated flow. The low lift-to-drag ratio predicted by GASP ($\frac{L}{D} = 2.5$) and the region of separated flow predicted by GASP, but not MSES, indicate a poor design of the Inboard airfoil. More design iterations are probably necessary to develop a good Inboard airfoil design, and each iterative cycle requires a substantial amount of time.

4.1.5. Inboard Jet-Wing Airfoil Results

The Inboard jet-wing airfoil was run using results from the Hybrid grid solution of the Inboard no-jet airfoil. Two iterations were required to obtain a self-propelled jet-

wing vehicle. First, using the average drag coefficient from the Inboard no-jet airfoil case, $C_D = 0.0273$, the jet flow Mach number was calculated to be $M_{jet} = 1.29$ and the jet flow density was calculated as $\rho_{jet} = 0.4004 \frac{kg}{m^3}$. However, when this jet-wing case was run, the vehicle was not self-propelled, as shown by the force coefficients in Table 4.6. The difference between the drag coefficient and the jet coefficient produced a net drag of $C_{D_{Net}} = 0.0081$. A new jet flow Mach number was computed as $M_{jet} = 1.39$ using the drag coefficient of $C_D = 0.0384$. This high drag and high jet flow Mach number result in a rather low propulsive efficiency of $\eta_p = 70.3\%$. The Inboard jet-wing airfoil case was run again with the new jet flow Mach number in an attempt to produce a self-propelled vehicle. The final force coefficient values are tabulated in Table 4.7 and it can be seen that the vehicle is still not quite self-propelled, as the net drag coefficient is $C_{D_{Net}} = 0.0024$. Still, the net drag was reduced from 24% to 7% of the airfoil drag. When the Inboard jet-wing airfoil cases were run, one of the first observations was that they converged better than the Inboard no-jet airfoil case, as shown in Figure 4.22. In fact, the Inboard jet-wing airfoil case converged to a lift coefficient of $C_{L_{Net}} = 0.277$, which is within 8% of the design lift coefficient of $C_L = 0.3$. The pressure distribution of the Inboard jet-wing airfoil is compared to the no-jet "peak" case in Figure 4.23. This shows that the jet-wing moves the lower surface shock forward by 9% of the chord and the upper surface shock aft by 5% of the chord. This reduces the negative lift on the aft 50% of the airfoil and allows the airfoil to approach the target lift coefficient of $C_L = 0.3$. Because the pressures on the Inboard jet-wing upper and lower surfaces cross over twice in Figure 4.23, the region of negative lift is reduced to from near 50% of the chord to 27% of the chord. Also, there is a significant difference in the upper and lower surface pressures at the trailing edge. The pressure coefficient on the upper surface is nearly 0.25 less than that on the lower surface. The upper surface skin friction, plotted in Figure 4.24, shows that the flow in the jet-wing case separates at $\frac{x}{c} = 81\%$, 7% of the chord and earlier than the separation point on the no-jet case. The flowfield around the Inboard jet-wing airfoil is shown Figure 4.25. Figure 4.26 shows that the region of separation significantly affects the jet by creating a zone of low pressure and pulling the jet flow upwards. The suction effect of the separation vortex is also observed in the area

of low pressure at the trailing edge of the airfoil in Figure 4.27. Lastly, the velocity profiles downstream of the Inboard no-jet and jet-wing airfoils are plotted in Figure 4.28. The region of separation on the no-jet airfoil increases the size of the wake that a jet must ‘fill in.’ However, since the jet-wing airfoil also experiences a region of separation, the jet does not do a good job of ‘filling in’ the wake downstream of the vehicle.

Table 4.6: Inboard no-jet and first iteration jet-wing airfoil results.

Airfoil	Inboard, no-jet	Inboard, jet-wing (first iteration)
Angle-of-attack, α	2.00°	2.00°
Jet Mach number, M_{jet}	0.000	1.290
Propulsive efficiency, η_P	--	73.6%
Lift coefficient, C_L	0.0685	0.2652
Drag coefficient, C_D	0.0273	0.0342
Jet coefficient, C_J	0.0000	0.0261
Net lift coefficient, $C_{L_{Net}}$	0.0685	0.2687
Net drag coefficient, $C_{D_{Net}}$	0.0273	0.0081

Table 4.7: Inboard no-jet and (final) jet-wing airfoil results.

Airfoil	Inboard, no-jet	Inboard, jet-wing (final)
Angle-of-attack, α	2.00°	2.00°
Jet Mach number, M_{jet}	0.000	1.385
Propulsive efficiency, η_P	--	70.3%
Lift coefficient, C_L	0.0685	0.2728
Drag coefficient, C_D	0.0273	0.0353
Jet coefficient, C_J	0.0000	0.0329
Net lift coefficient, $C_{L_{Net}}$	0.0685	0.2767
Net drag coefficient, $C_{D_{Net}}$	0.0273	0.0024

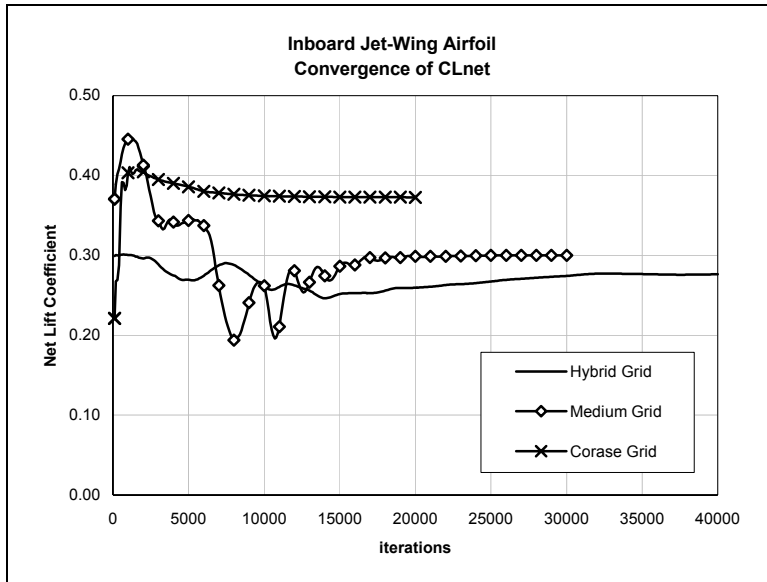


Figure 4.22: Inboard jet-wing airfoil GASP grid convergence history.

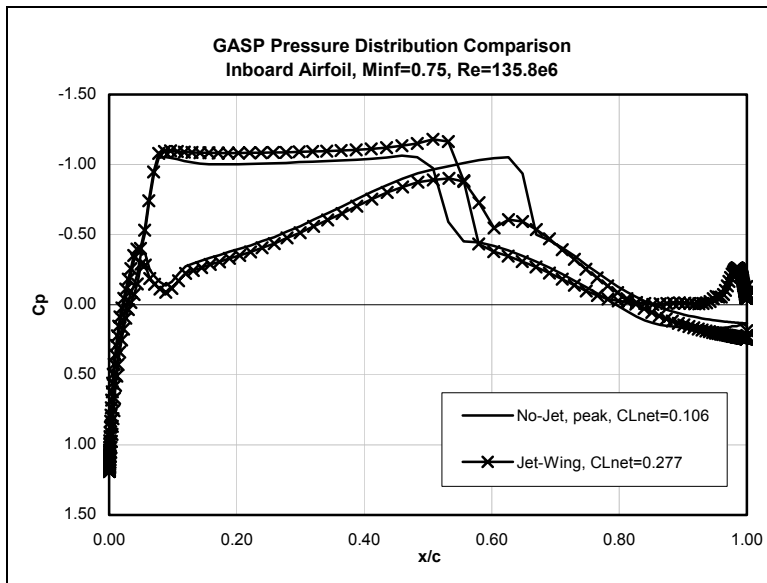


Figure 4.23: Inboard no-jet and jet-wing airfoil GASP pressure distributions.

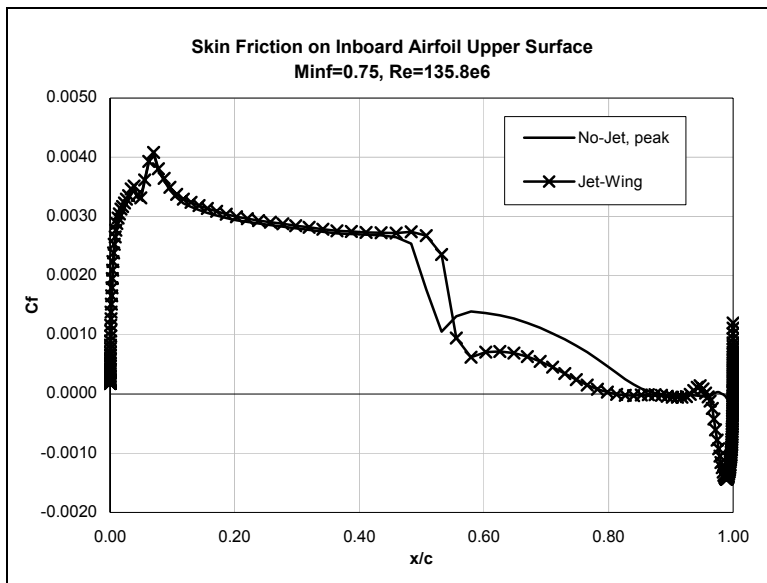


Figure 4.24: Inboard no-jet and jet-wing airfoil GASP upper surface skin friction.

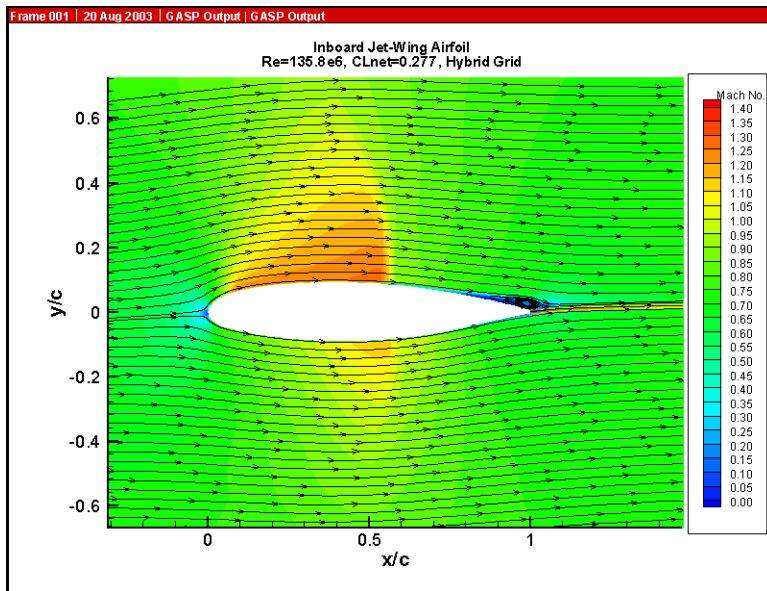


Figure 4.25: Streamlines and Mach number contours around Inboard jet-wing airfoil.

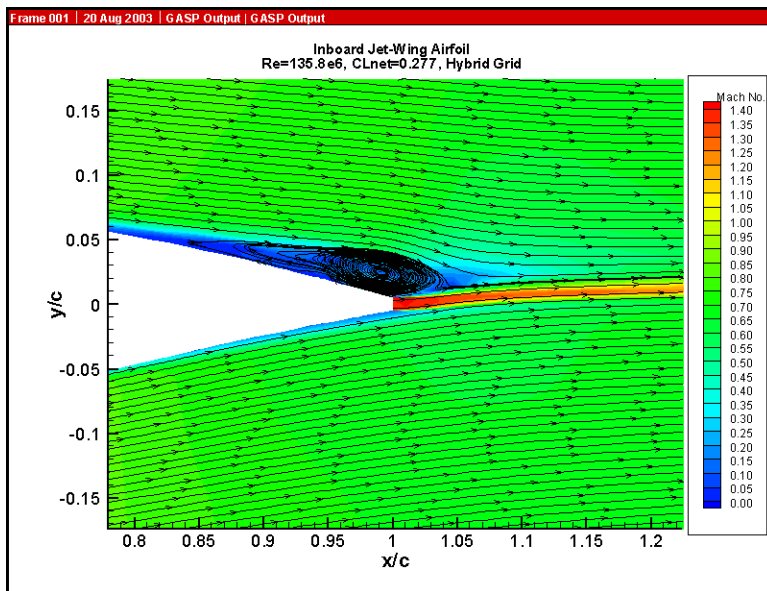


Figure 4.26: Streamlines and Mach number contours near trailing edge of Inboard jet-wing airfoil. Note region of separated flow.

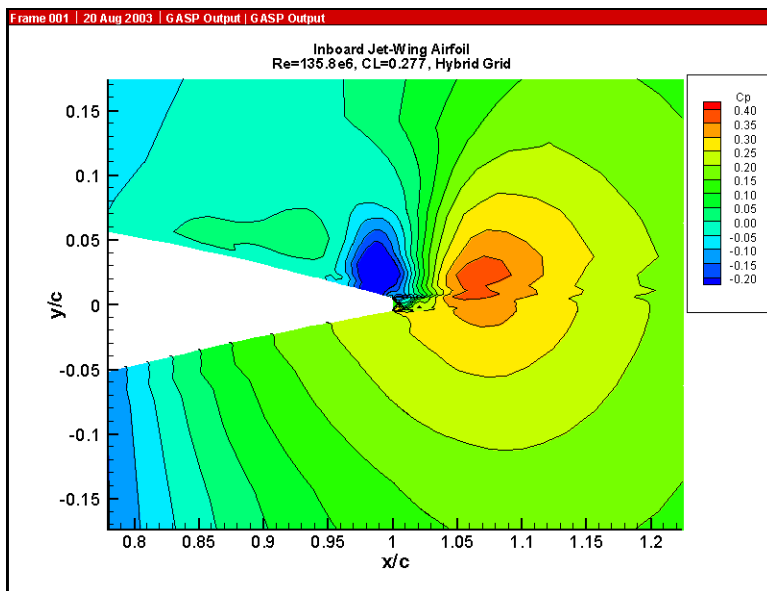


Figure 4.27: Pressure contours at the trailing edge of Inboard jet-wing airfoil.

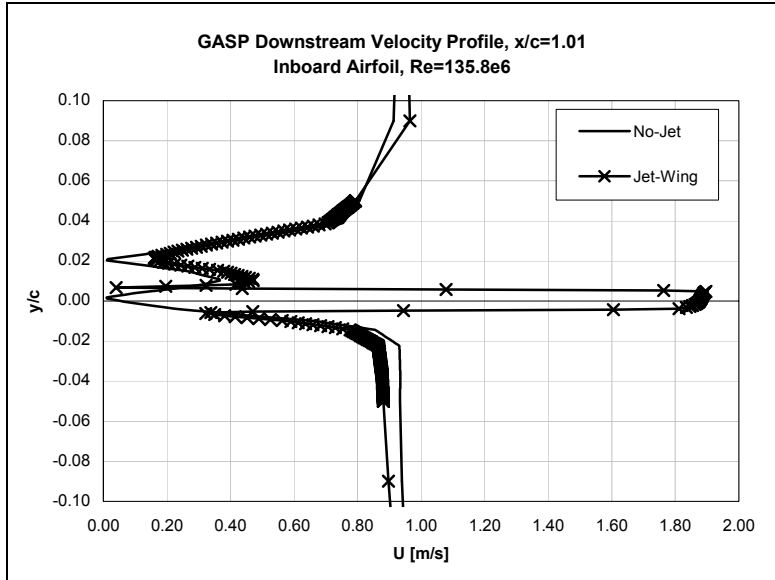


Figure 4.28: Velocity profile downstream Inboard no-jet and jet-wing airfoils.

Overall, the Inboard jet-wing airfoil exhibits more favorable results than the Inboard no-jet airfoil, particularly with respect to the lift coefficient, because it is much closer to the target of $C_L = 0.3$ than the Inboard no-jet airfoil. However, the inboard jet-wing airfoil still suffers a large region of separation (19% of the chord). While one might think that the jet-wing could entrain flow near the trailing edge and reduce the size of the region of separated flow, this is not the case. In fact, the region of separated flow grows larger with the presence of the jet-wing. This large region of separated flow causes a large value of drag and a large wake that the jet-wing must ‘fill in.’ Therefore, the propulsive efficiency is rather low at $\eta_p = 70.3\%$. A better design of the Inboard airfoil could be found, not only to reduce the drag and increase the propulsive efficiency when the jet-wing is applied, but also to give better performance when no jet is present.

4.2. Jet-Wing Studies for Low Reynolds Number Vehicles

The next set of cases that were examined includes jet-wing configurations of the Outboard 1xTE airfoil at a lower Reynolds number, $Re_c = 5.67e6$. The results show the effectiveness of the distributed propulsion jet-wing configuration when applied to smaller vehicles, such as UAVs. In addition to the baseline jet-wing configuration, in which the jet deflection angle is $\tau = 0.0^\circ$, jet-flaps were also studied, with jet deflection angles of $\tau = -2.66^\circ$, $\tau = 5.0^\circ$, $\tau = 10.0^\circ$.

4.2.1. Outboard 1xTE No-Jet Airfoil Results at Low Reynolds Number

Before studying the effects of the jet-wing at the lower Reynolds number, it is important to see how the Outboard 1xTE airfoil performs at the lower Reynolds number compared with the same airfoil at the design Reynolds number of $Re_c = 38.4e6$. The lift and drag coefficients for the two cases are presented in Table 4.8. At the same angle of attack $\alpha = 2.66$ deg, the lift coefficient of the low Reynolds number case is 2.7% smaller than that of the design Reynolds number case, and the drag coefficient of the low Reynolds number case is 3.2% larger. The pressure distributions of the design and low Reynolds number cases are pictured in Figure 4.29. It can be observed that the shockwave moves about 1% of the chord farther forward in the low Reynolds number case when compared to the design Reynolds number case. Even before the jet-wing case is run, it can be realized that the low Reynolds number jet-wing will require a slightly higher jet velocity than the design Reynolds number case, thereby reducing the propulsive efficiency by a small amount.

Table 4.8: Outboard 1xTE no-jet airfoil results for design and lower Reynolds numbers

Case	Design Re_c	Low Re_c
Reynolds Number, Re_c	38.4e+6	5.67e+6
Angle-of-attack, α	2.66°	2.66°
Lift coefficient, C_L	0.6276	0.6106
Drag coefficient, C_D	0.0124	0.0128

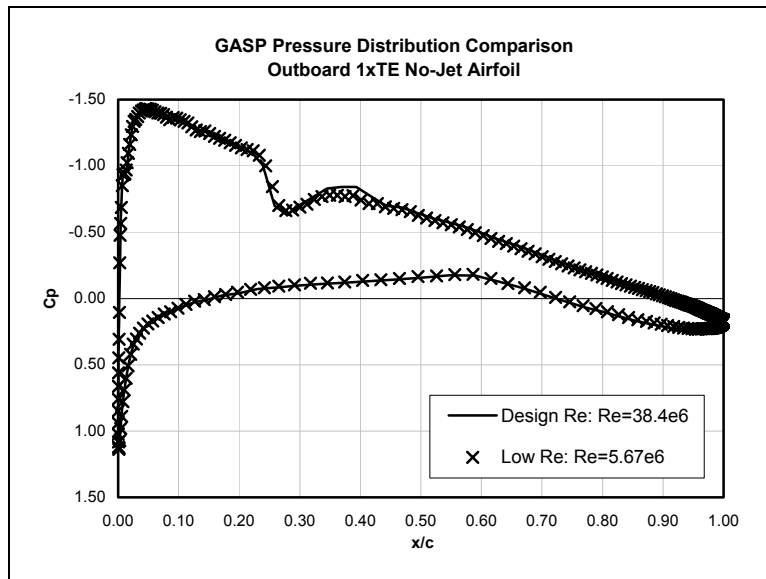


Figure 4.29: Comparison of GASP pressure distribution for Outboard 1xTE no-jet airfoil at design and low Reynolds numbers.

4.2.2. Outboard 1xTE Jet-Wing Airfoil Results at Low Reynolds Number

Using the drag coefficient of $C_D = 0.0128$ and the trailing edge pressure of $p_{TE} = 25365 \text{ N/m}^2$ from the no-jet airfoil, the jet flow Mach number, $M_{jet} = 1.22$, and jet flow density, $\rho_{jet} = 0.4038 \text{ kg/m}^3$, were calculated for the jet-wing case. The propulsive efficiency was found to be $\eta_p = 74.3\%$, as which is slightly lower than that of the design Reynolds number case, $\eta_p = 75.1\%$. The Outboard 1xTE jet-wing airfoil was run in GASP at the lower Reynolds number, and the resulting force coefficients are presented in Table 4.9. The lift coefficient of the jet-wing airfoil was within 0.7% of that of the no-jet airfoil, so increasing the angle of attack was not be necessary. Also noteworthy is the fact that the drag decreases only 4% with the jet-wing applied for the low Reynolds number case. Referring to Table 4.1, this decrease in drag is comparable to the 5.6% drag decreases of the design Reynolds number case. The pressure distribution for the jet-wing and no-jet airfoils are shown in Figure 4.30. The velocity profiles downstream of the no-jet and jet-wing airfoils are shown in Figure 4.31. Figure 4.32 compares the downstream velocity profiles of the design Reynolds number and the low Reynolds number jet-wing cases. The two jet velocities are comparable.

Table 4.9: Outboard 1xTE no-jet and jet-wing airfoil results for $Re_c = 5.67e6$.

Airfoil	Outboard 1xTE, no-jet	Outboard 1xTE, jet-wing
Angle-of-attack, α	2.66°	2.66°
Jet Mach number, M_{jet}	0.000	1.220
Propulsive efficiency, η_p	--	74.3%
Lift coefficient, C_L	0.6106	0.6045
Drag coefficient, C_D	0.0128	0.0123
Jet coefficient, C_J	0.0000	0.122
Net lift coefficient, $C_{L_{Net}}$	0.6106	0.6067
Net drag coefficient, $C_{D_{Net}}$	0.0128	0.0001

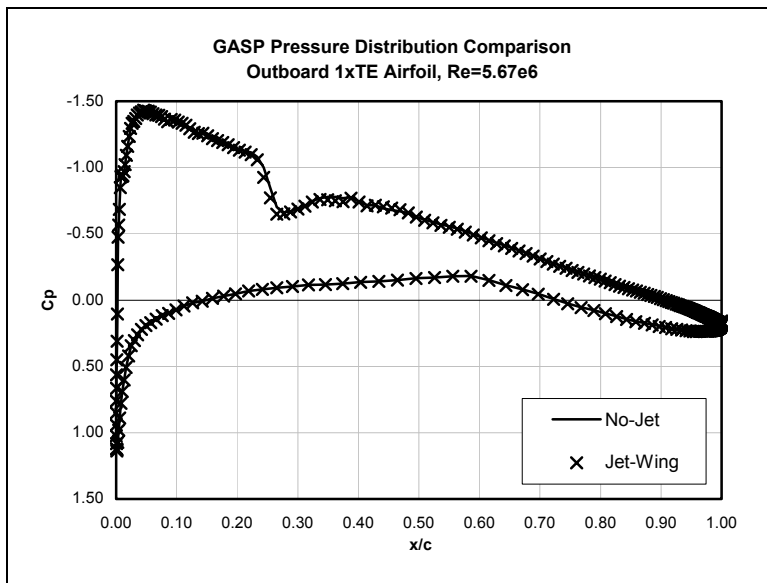


Figure 4.30: Outboard 1xTE no-jet and jet-wing airfoil pressure distribution at low Reynolds number.

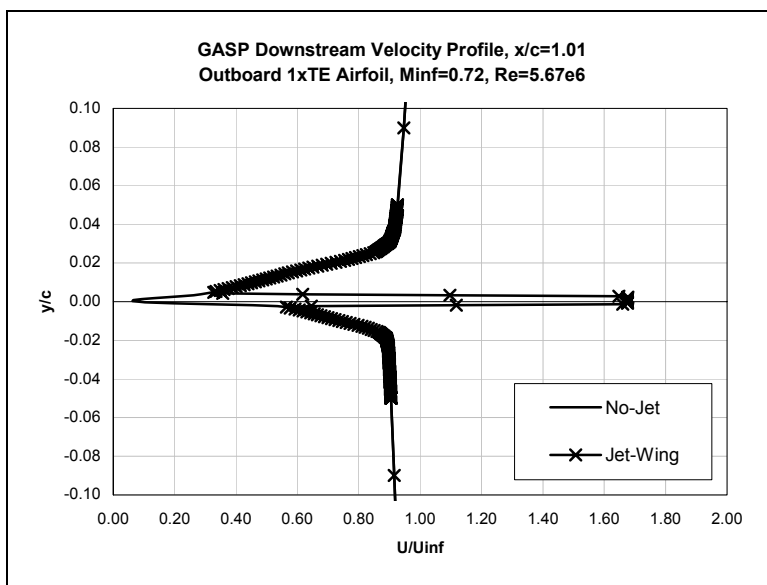


Figure 4.31: Velocity profile downstream of Outboard 1xTE no-jet and jet-wing airfoils at low Reynolds number.

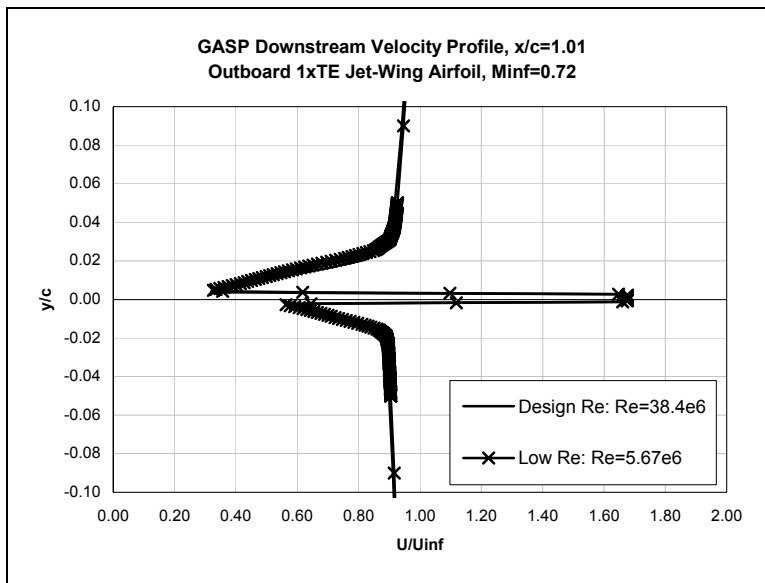


Figure 4.32: Velocity profile downstream of Outboard jet-wing airfoils at design and low Reynolds numbers.

4.2.3. Outboard 1xTE Airfoil Jet-Flap Studies at Low Reynolds Number

In addition to the usual jet-wing studies, several jet-flap cases were run at the lower Reynolds number to see how the jet influences the vehicle's performance when deflected to different angles. Antinello [13] and Yoshihara [18] both studied high deflection angle (e.g. $\tau = 80^\circ$) jet-flaps applied to high-lift situations. The jet-flap cases examined in this study used small jet deflection angles ($\tau = -2.66^\circ$, $\tau = 5.0^\circ$, and $\tau = 10.0^\circ$) applied to the Outboard 1xTE airfoil at cruise conditions and an angle of attack of $\alpha = 2.66^\circ$. Because the vehicle was modeled to be self-propelled, the jet coefficient was moderate and on the order of $C_j = 0.14$.

When running these cases, it must be mentioned that deflecting the jet and producing a self-propelled jet-flap airfoil was not straightforward and required several iterations. In fact, more iterations were required as the jet deflection angle increased. For this reason, the additional complexity of maintaining a constant lift was not considered. The performance results of jet-flap cases are shown in Table 4.10 for the three jet deflection angles. Note that the jet deflection angle of $\tau = -2.66^\circ$ aligns the jet with the freestream flow. In Table 4.10 and Figure 4.33, it is observed that as the jet deflection angle τ is increased even a small amount, the net lift increases significantly (by up to 31% for $\tau = 10^\circ$). As indicated in Figure 4.33, the pitching moment also increases as the jet deflection angle increases, by 100% for a jet deflection angle of $\tau = 10^\circ$. But, the increased lift and pitching moment performance do come at a cost of

increased drag and decreased propulsive efficiency. The drag increases by 19% for the $\tau = 10^\circ$ case. In addition to overcoming the increased drag at the higher jet deflection angles, the jet flow velocity must increase more to produce a sufficient component of thrust in the direction parallel to the drag (and parallel to the freestream). For a self-propelled vehicle, the required jet coefficient is given in Equation (4.3).

$$C_J = \frac{C_{D_{net}}}{\cos(\alpha + \tau)} \quad (4.3)$$

Table 4.10: Outboard 1xTE jet-wing and jet-flap airfoil results for $Re_c = 5.67e6$.

Airfoil	Jet-Wing	Jet-Flap 1	Jet-Flap 2	Jet-Flap 3
Angle-of-attack, α	2.66°	2.66°	2.66°	2.66°
Jet angle, τ	0.0°	-2.66°	5.0°	10.0°
Jet Mach number, M_{jet}	1.220	1.220	1.280	1.340
Propulsive efficiency, η_P	74.3%	74.3%	72.1%	70.0%
Lift coefficient, C_L	0.6045	0.5642	0.6935	0.7877
Drag coefficient, C_D	0.0123	0.0122	0.0132	0.0152
Jet coefficient, C_J	0.122	0.121	0.142	0.160
Net lift coefficient, $C_{L_{Net}}$	0.6067	0.5642	0.7003	0.7996
Net drag coefficient, $C_{D_{Net}}$	0.0001	0.0001	-0.0009	-0.0005
Net pitching moment coefficient, $C_{m_{net}}$	0.0341	0.0268	0.0505	0.0702

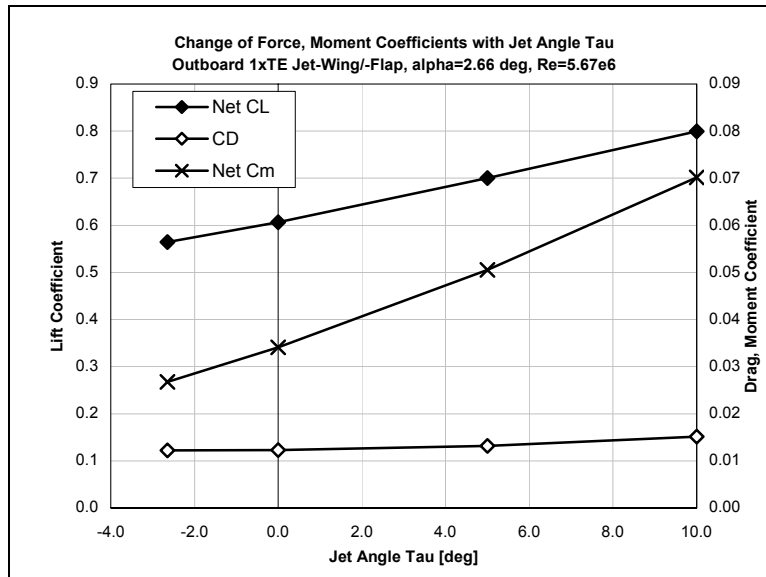


Figure 4.33: Trends in lift, drag, pitching moment with jet deflection angle constant angle of attack and low Reynolds number.

The deflected jet produces some interesting effects on the flow around the airfoil. The pressure distributions for the jet-wing and jet-flap airfoils are compared in Figure

4.34. Compared to the baseline jet-wing ($\tau = 0^\circ$), deflecting the jet-flap downward moves the shock aft, while deflecting the jet-flap upward moves the shock forward. This helps explain the changes in lift produced by the jet-flap, as seen in Table 4.10. Furthermore, the jet-flap alters the pressure at the trailing edge, as shown in Figure 4.35. Whereas airfoils and even the jet-wings presented in this study typically experience equal pressures on both the upper and lower surfaces at the trailing edge, when the jet is deflected, the upper and lower surface pressures at the trailing edge diverge. For negative jet deflection angles, the pressure of the lower surface at the trailing edge is actually less than the pressure on the upper surface at the trailing edge. Meanwhile, for positive jet deflection angles, the pressure distribution at the trailing edge spreads out. This phenomena was also observed by Yoshihara [18]. Figure 4.36 shows the flow field near the trailing edge of the jet-wing and jet-flap airfoils at the low Reynolds number. Figure 4.37 shows that in the $\tau = 5^\circ$ and $\tau = 10^\circ$ jet-flap cases, a series of oblique shocks and expansions appear to form inside the core jet flow as it turns and aligns with the surrounding flow. Again, because of the large jet deflection angles examined in his study, Yoshihara observed similar flow structures [18].

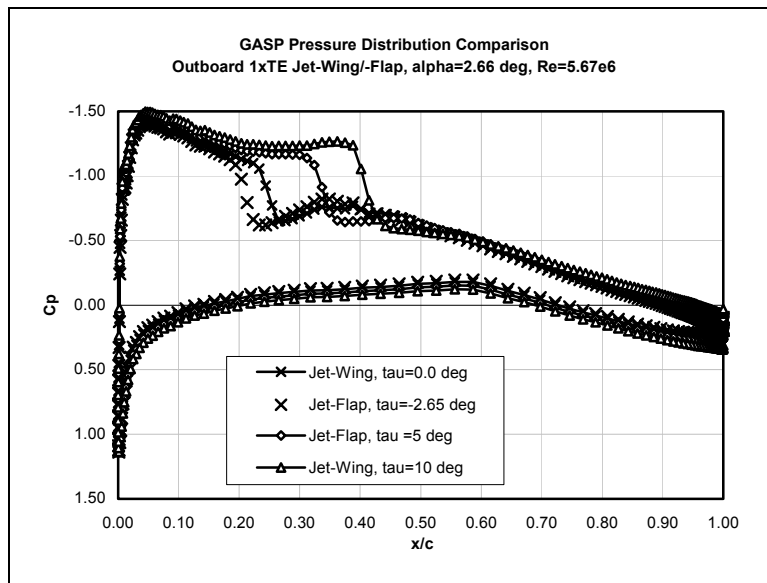


Figure 4.34: Comparison of GASP pressure distributions for Outboard 1xTE jet-wing/-flap airfoil at constant angle of attack and low Reynolds number.

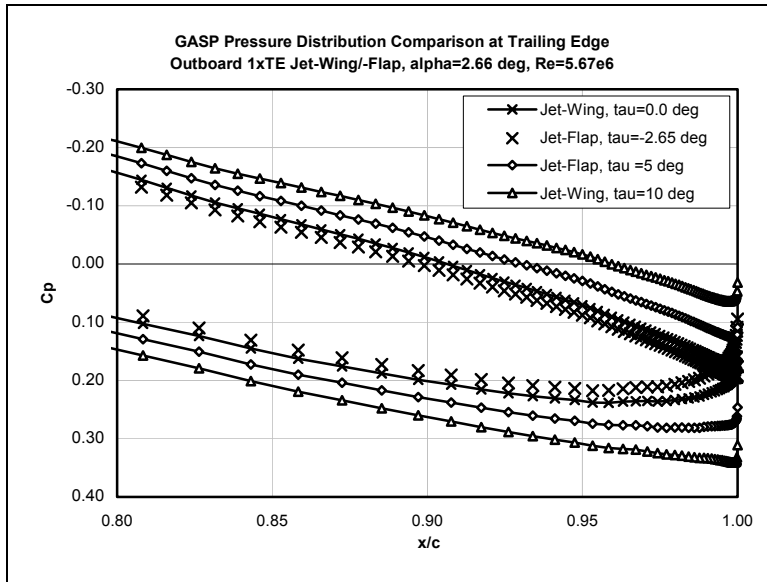


Figure 4.35: Comparison of GASP pressure distribution near the trailing edge of the Outboard 1xTE jet-wing/-flap airfoils at low Reynolds number.

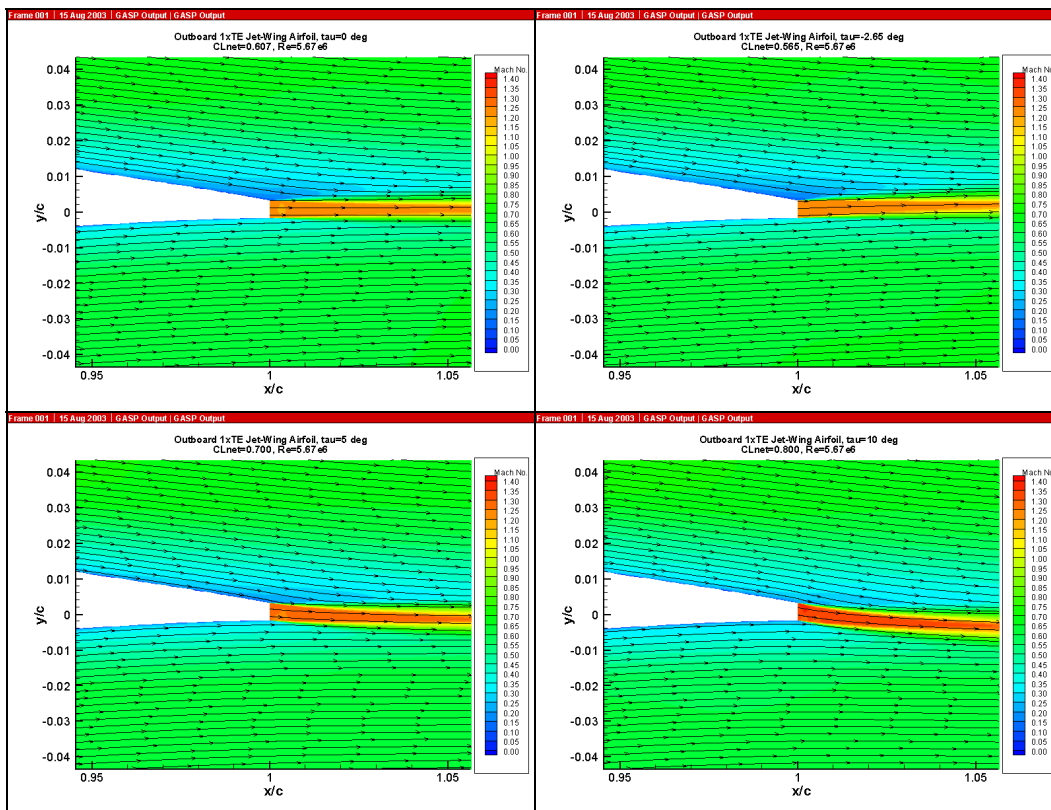


Figure 4.36: Streamlines and Mach number contours at trailing edge of Outboard 1xTE jet-wing/-flap airfoils at Low Reynolds number.

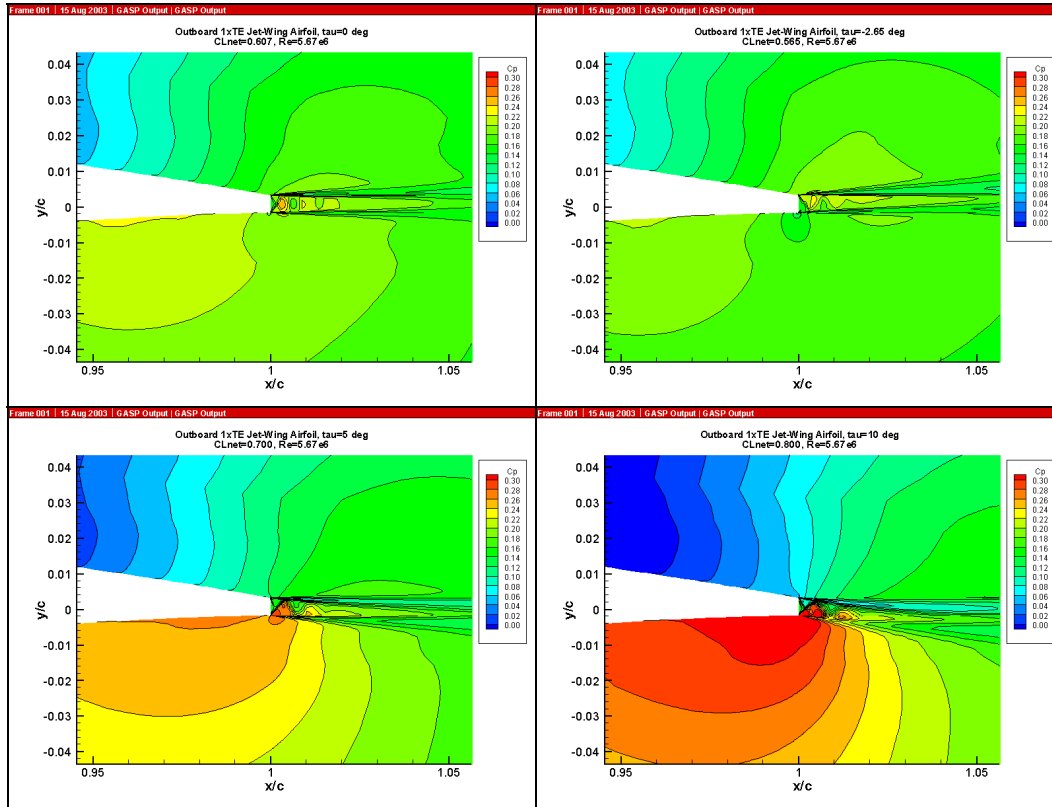


Figure 4.37: Pressure contours at trailing edge of Outboard jet-flap airfoils at Low Reynolds number.

The jet-flap studies show that at a constant angle of attack, a jet deflected at even a small angle can significantly increase (or decrease, if negative jet deflection) the lift and pitching moment of a jet-wing vehicle. However, there is also a drag penalty associated with positive jet deflection angles. To remain self-propelled, the jet flow velocity must be increased, thereby decreasing the propulsive efficiency. One additional CFD jet-flap study that could be performed would examine the effect of different jet deflection angles when maintaining a constant lift. The jet-flaps examined in this study only varied one parameter set: the jet flow conditions. This further study would also require an additional degree of complexity, as the airfoil angle of attack would also need to be varied.

Chapter 5. Conclusions

In this research endeavor, parametric CFD analyses were performed on two-dimensional jet-wing airfoils. The goal of these studies was to assess the performance of the jet-wing and apply the results to an MDO framework for distributed propulsion on a BWB aircraft. It has been suggested that distributed propulsion can increase propulsive efficiency beyond the $\eta_p = 80\%$ typical of the most efficient modern turbofan-powered aircraft [23]. This research effort attempted to validate this performance benefit of distributed propulsion and assess any negative consequences.

First, an airfoil was developed that was representative of the wing sections at an outboard span location of the BWB. The jet-wing was applied to the Outboard 1xTE airfoil and the resulting propulsive efficiency was $\eta_p = 75\%$. This is slightly less than the 80% propulsive efficiency typical of most efficient aircraft. Because the height of the jet was only 0.5% of the airfoil's chord and the wake had a height of about 4% of the chord, the jet did a poor job of 'filling in' the wake.

The trailing edge thickness - and thus the jet height - was then expanded to 1% of the chord. When the jet-wing was applied, the propulsive efficiency increased to about $\eta_p = 83\%$. While this is a 3% increase over the propulsive efficiency of modern high-bypass-ratio aircraft, it must be remembered that the jet-wing is part of a hybrid distributed propulsion system, and the entire system's propulsive efficiency must be taken into account. The drag of the Outboard 2xTE airfoil increased by nearly 10% over the drag of the Outboard 1xTE airfoil. While the increase in propulsive efficiency is favorable, the drag penalty is not. The increase in drag is particularly a problem during the engine-out condition. This study shows that there are limits to expanding the jet height to increase propulsive efficiency. With a jet-wing, one cannot simply expand the

jet height to a length approaching the size of the wake without negative aerodynamic consequences.

Performing CFD analyses on the Inboard airfoil proved more complicated than analyses on the representative outboard airfoils. The Inboard airfoil showed evidence of a periodic flow and lacked true steady-state convergence, at least without becoming too computationally expensive. This caused problems when applying the jet-wing. When the jet-wing was applied, the vehicle was not quite self-propelled. It is estimated that a 9% increase in the jet flow velocity is required to make the Inboard jet-wing airfoil self-propelled. The resulting propulsive efficiency would be $\eta_p = 79\%$, which is a bit less than the most efficient modern aircraft, and the Outboard 1xTE jet-wing airfoil. However, it should be noted that the jet height of the Inboard airfoil was only 1% of the chord. Unfortunately, the changes in lift and, in particular, drag could not be assessed for the Inboard airfoil, because the solution of the no-jet case was very much different from both the design and the jet-wing case. It can be concluded that the Inboard airfoil used may not be a good design and that a better design should be used for future parametric CFD studies. The Inboard airfoil exhibits a more complex flowfield than the Outboard airfoil. This includes shocks on both surfaces and a region of separated flow that interact with each other and the jet-wing, when applied. The detailed design of an efficient jet-wing for inboard sections of the BWB represents a significant challenge that requires and deserves a concentrated effort.

The jet-wing was applied to the Outboard airfoil for a lower Reynolds number, one that could be found on to a UAV. This study showed that the propulsive efficiency decreases as the Reynolds number decreases. Jet-flaps were also studied at this lower Reynolds number and showed that the lift, drag, and pitching moment all vary linearly as the jet-angle is varied (maintaining a constant angle of attack).

5.1. Recommended Further Studies:

In light of the conclusions and what this work did study, several recommendations can be made for future jet-wing distributed propulsion assessment work. First, the Inboard airfoil exhibited an unsteady flow and the solutions of the no-jet and jet-wing cases could not be compared because they were so different. Therefore, it is recommended that a better Inboard airfoil design be developed. A better

performing Inboard airfoil would allow more confidence to be placed in the results of parametric CFD jet-wing studies.

Second, these studies only observed the jet flow as it exited the jet-wing. It is recommended that the internal flow of the jet-wing also be examined to gauge the losses and difficulties of ducting the engine for exhaust in such a way.

For the forward-thinker, one could look at designing airfoils with jet-wing propulsion in mind: airfoils with thicker trailing edges, but with low drag at cruise. One possible idea is a morphing wing, in which the aft portion can open and close, similar to many jet nozzles. When open, the trailing edge “nozzle” would provide high propulsive efficiency. During engine-out or when the engine thrust is not needed, the trailing edge would close to reduce drag.

These CFD studies were performed on two-dimensional models only, whereas distributed propulsion would ultimately be applied to a three-dimensional aircraft (be it a BWB or a conventional airliner) with a three-dimensional wing and three-dimensional flows. Therefore, it is recommended that CFD studies of jet-wing distributed propulsion be applied to a three-dimensional wing. As with all CFD analyses, these studies should begin low in complexity, i.e. a finite wing of simple taper and sweep with a jet-wing applied to the trailing edge. A three-dimensional analysis would allow an even better understanding of the performance benefits and consequences and the associated flowfield of jet-wing distributed propulsion.

Next, in addition to a three-dimensional analysis, one could look at the performance of the entire hybrid distributed propulsion system. The jet-wing configuration is meant only to overcome the drag due to pressure and viscous forces. The hybrid distributed propulsion system also uses part of the exhaust from the turbofan engines to overcome the induced drag of the aircraft. The performance of the entire system should be investigated.

Last, the control effectiveness of a jet-wing with deflected jets needs to be studied in detail with a view to eliminating flaps and slats and their associated noise.

References

- [1] Callaghan, J. T., and Liebeck, R. H., "Some Thoughts on the Design of Subsonic Transport Aircraft for the 21st Century," SAE Paper No. 901987, October 1990.
- [2] Liebeck, R. H., Page, M. A., Rawdon, B. K., Scott, P. W., and Wright, R. A., "Concepts for Advanced Subsonic Transports" NASA CR 4624, Sept. 1994.
- [3] Liebeck, R. H., Page, M. A., Rawdon, B. K., Girvin, R. R., Scott, P. W., Potsdam, M. A., Bird, R. S., Wakayama, S., Hawley, A. V., Rowland, G. T., "Blended-Wing-Body Configuration Control Document (1-26-96) CCD-2," McDonnell Douglas Aerospace, Long Beach, CA, Jan., 1996
- [4] Liebeck, R. H., Page, M. A., Rawdon, B. K., "Blended-Wing-Body Subsonic Commercial Transport," 36th Aerospace Sciences Meeting & Exhibit, AIAA-98-0438, Reno, NV, Jan. 12-15, 1998.
- [5] Liebeck, R., "Design of the Blended-Wing-Body Subsonic Transport," 40th Aerospace Sciences Meeting & Exhibit, AIAA-2002-0002, Reno, NV, Jan. 14-17, 2002.
- [6] Wakayama, S., "Blended-Wing-Body Optimization Problem Setup," 8th AIAA/USAF/NASA/ISSMO Symposium on Multidisciplinary Analysis and Optimization, AIAA-2000-4740, Long Beach, CA, Jan. 6-8, 2000.
- [7] Wakayama, S. and Kroo, I., "The Challenge and Promise of Blended-Wing-Body Optimization," 7th AIAA/USAF/NASA/ISSMO Symposium on Multidisciplinary Analysis and Optimization, AIAA 98-4736, St. Louis, MO, Sept. 2-4, 1998.
- [8] Wakayama, S., "Multidisciplinary Design Optimization of the Blended-Wing-Body," 7th AIAA/NASA/ISSMO Symposium on Multidisciplinary Analysis and Optimization, AIAA-98-4938, St. Louis, MO, Sept. 2-4, 1998.
- [9] Anonymous, "Blended-Wing-Body (BWB) ... A New Approach to Tomorrow's Challenges," BWB technology concept flyer.
- [10] *NASA Aeronautics Blueprint: Toward a Bold New Era in Aviation*, NASA, http://www.aerospace.nasa.gov/aero_blueprint/cover.html
- [11] Guynn, M. D., Olson, E. D., "Evaluation of an Aircraft Concept with Over-Wing, Hydrogen-Fueled Engines for Reduced Noise and Emissions," NASA TM-2002-211926, September 2002.

- [12] Ko, Y.-Y. A, "The Multidisciplinary Design Optimization of a Distributed Propulsion Blended-Wing-Body Aircraft," Ph.D. Dissertation, Virginia Polytechnic Institute & State University, April, 2003.
- [13] Attinello, J. S., "The Jet Wing," IAS Preprint No. 703, IAS 25th Annual meeting, Jan. 28-31, 1957.
- [14] Kuchemann, D., *The Aerodynamic Design of Aircraft*, Pergamon Press, New York, 1978, pp. 229.
- [15] Hagendorn, H. and Ruden, P., "Wind Tunnel Investigation of a Wing with Junkers Slotted Flap and the Effect of Blowing Through the Trailing Edge of the Main Surface Over the Flap," Report by Institut fur Aeromachanik and Flugtechnik der Technischen Hochschule, Hannover LGL Bericht A64 (1938). Available as R.A.E. Translation No. 422, December, 1953.
- [16] Spence, D. A., "The Lift Coefficient of a Thin, Jet-Flapped Wing," *Proceedings of the Royal Society of London, Series A, Mathematical and Physical Sciences*, Volume 238, Issue 112, Dec., 1956, pp 46-68.
- [17] Ives, D. C., and Melnik, R. E., "Numerical Calculation of the Compressible Flow over an Airfoil with a Jet Flap," 7th AIAA Fluid and Plasma Dynamics Conference, AIAA-74-542, Palo Alto, CA, June 17-19, 1974.
- [18] Yoshihara, H., Zonars, D., "The Transonic Jet Flap: A Review of Recent Results." ASE-751089, National Aerospace and Manufacturing Meeting, November 1975.
- [19] Kimberlin, R. D., "Performance Flight Test Evaluation of the Ball-Bartoe JW-1 JetWing STOL Research Aircraft," *Flight Testing in the Eighties: 11th Annual Symposium Proceedings of the Society of Flight Test Engineers*, Aug 27-29, 1980.
- [20] Kimberlain, R. D., "An Investigation of a Thrust Augmenting Ejector on the Performance and Handling Qualities of an Upper Surface Blown Research Aircraft," *Proceedings of Flight Test Engineers Thirteenth Annual Symposium*, New York, NY, September 1982.
- [21] "Jetwing from Colorado," *Air International*, Vol. 14, No. 2, pp 69-71, February 1978.
- [22] *Marine Engineering*, Vol. 1, Society of Naval Architects & Marine Engineers, Ed. Herbert Lee Seward, pp. 10-11.
- [23] Hill, P. and Peterson, C., *Mechanics and Thermodynamics of Propulsion*, 2nd Ed., Addison-Wesley, New York, 1992.

- [24] Ko, A., Schetz, J. A., Mason, W. H., "Assessment of the Potential Advantages of Distributed-Propulsion for Aircraft," XVth International Symposium on Air Breathing Engines (ISABE), Cleveland, OH, Paper 2003-1094, Aug. 31 - Sept. 5, 2003.
- [25] Bertin, J. J. and Smith, M. L., *Aerodynamics for Engineers*, 3rd Ed., Prentice Hall, New Jersey, 1998.
- [26] Harris, C. D., "NASA Supercritical Airfoils: A Matrix of Family Related Airfoils," NASA TP 2969, March 1990.
- [27] Drela, M., "A User's Guide to MSES 2.95," MIT Computational Aerospace Sciences Laboratory, Sept., 1996.
- [28] Drela, M., "MSES Multi-element Airfoil Design/Analysis Software - Summary," <http://raphael.mit.edu/projects%26research.html>, Massachusetts Institute of Technology, MA, May, 1994.
- [29] Ko, A., Mason, W. H., Grossman, B., Schetz, J. A., "A-7 Strut Braced Concept Transonic Wing Design," Virginia Tech Department of Aerospace and Ocean Engineering Report AOE-275, July 12, 2002.
- [30] Pambajo, T. E., Nakahashi, K., Obayashi, S., and Matsushima, K., "Aerodynamic Design of A Medium Size Blended-Wing-Body Airplane," 39th AIAA Aerospace Sciences and Exhibit Meeting, AIAA-2001-0129, Reno, NV, Jan. 8-11, 2001.
- [31] Roman, D., Allen, J. B., and Leibek, R. H., "Aerodynamic Challenges of the Blended-Wing-Body Subsonic Transport," 18th AIAA Applied Aerodynamics Conference, AIAA-2000-4335, Denver, CO, Aug. 14-17, 2000.
- [32] Mason, W. H., *Applied Computational Aerodynamics Text/Notes*, Appendix E, Utility Codes, E.5, Bump, http://www.aoe.vt.edu/~mason/Mason_f/CAtxtAppE.html
- [33] Mason, W. H., *Foilgen*, Virginia Polytechnic Institute and State University, 1990.
- [34] AGARD Advisory Report No. 138, "Experimental Data Base for Computer Program Assessment," May, 1979.
- [35] *ANSYS 6.1 Documentation*, ANSYS, Inc, 2002.
- [36] MacLean, M., "A Numerical Study of Internal Flow Effects on Skin Friction Gages," Ph.D. Dissertation, Virginia Polytechnic Institute & State University, April, 2002.

- [37] Devenport, W., Kapania, R., Rojiani, K., and Sigh, K., *Java Applets For Engineers*, <http://www.engapplets.vt.edu>.
- [38] Yaros, S. F., Sextone, M. G., Huebner, L. D., Lamar, J. E., McKinley, Jr., R. E., Torres, A. O., Burley, C. L., Scott, R. C., Small, W. J., "Synergistic Airframe-Propulsion Interactions and Integrations," NASA TM-1998-207644, March 1998.
- [39] Presz, Jr., W., Reynolds, G., and Hunter, C., "Thrust Augmentation with Mixer/Ejector Systems," 40th Aerospace Sciences Meeting & Exhibit, AIAA-2002-0230, Reno, NV, Jan. 14-17, 2002.
- [40] Liepman, H. W. and Roshko, A., *Elements of Gasdynamics*, Dover Publications, New York, 1985.
- [41] Schetz, J. A., *Boundary Layer Analysis*, Prentice Hall, New Jersey, 1993.
- [42] *GASP Version 4.1.1 Reference Guide*, Aerosoft, Inc, Blacksburg, VA.
- [43] *Gridgen Version 14 User Manual*, Pointwise, 2002.
- [44] Thompson, J. F., ed., Bharat, K. S., ed., and Weatherhill, N. P., ed., *The Handbook of Grid Generation*, CRC Press, Washington, DC, 1999.

Appendix A. Tabulated Airfoil Coordinates

A.1. Outboard 1xTE Airfoil Coordinates

Lower Surface			
x/c	y/c	x/c	y/c
0.00000	0.00000	0.24377	-0.04757
0.00023	-0.00257	0.25130	-0.04785
0.00100	-0.00541	0.25882	-0.04810
0.00234	-0.00819	0.26635	-0.04833
0.00424	-0.01078	0.27389	-0.04854
0.00677	-0.01319	0.28142	-0.04874
0.00990	-0.01544	0.28895	-0.04891
0.01355	-0.01761	0.29649	-0.04907
0.01771	-0.01970	0.30403	-0.04921
0.02239	-0.02165	0.31158	-0.04932
0.02760	-0.02346	0.31913	-0.04942
0.03327	-0.02515	0.32668	-0.04950
0.03934	-0.02674	0.33423	-0.04956
0.04574	-0.02821	0.34179	-0.04961
0.05241	-0.02958	0.34935	-0.04965
0.05928	-0.03087	0.35691	-0.04968
0.06628	-0.03209	0.36447	-0.04970
0.07341	-0.03323	0.37203	-0.04970
0.08061	-0.03429	0.37959	-0.04968
0.08788	-0.03531	0.38715	-0.04965
0.09519	-0.03629	0.39471	-0.04960
0.10251	-0.03721	0.40227	-0.04954
0.10986	-0.03808	0.40983	-0.04947
0.11721	-0.03890	0.41740	-0.04938
0.12458	-0.03967	0.42496	-0.04929
0.13197	-0.04038	0.43253	-0.04918
0.13937	-0.04104	0.44009	-0.04906
0.14676	-0.04170	0.44764	-0.04893
0.15416	-0.04234	0.45520	-0.04878
0.16157	-0.04292	0.46275	-0.04862
0.16899	-0.04343	0.47030	-0.04844
0.17643	-0.04394	0.47785	-0.04824
0.18387	-0.04446	0.48539	-0.04803
0.19133	-0.04496	0.49294	-0.04779
0.19879	-0.04543	0.50048	-0.04754
0.20626	-0.04586	0.50802	-0.04728
0.21374	-0.04625	0.51556	-0.04701
0.22123	-0.04661	0.52309	-0.04672
0.22874	-0.04695	0.53060	-0.04640
0.23625	-0.04727	0.53811	-0.04606

Lower Surface (Continued)

x/c	y/c	x/c	y/c
0.54561	-0.04569	0.84602	-0.01386
0.55312	-0.04529	0.85352	-0.01298
0.56061	-0.04487	0.86102	-0.01211
0.56810	-0.04443	0.86852	-0.01127
0.57557	-0.04396	0.87601	-0.01045
0.58304	-0.04345	0.88349	-0.00964
0.59050	-0.04290	0.89098	-0.00886
0.59796	-0.04232	0.89846	-0.00810
0.60542	-0.04171	0.90593	-0.00736
0.61289	-0.04104	0.91339	-0.00665
0.62037	-0.04034	0.92084	-0.00597
0.62787	-0.03963	0.92828	-0.00533
0.63537	-0.03891	0.93569	-0.00473
0.64288	-0.03817	0.94307	-0.00416
0.65038	-0.03741	0.95040	-0.00364
0.65788	-0.03663	0.95766	-0.00319
0.66537	-0.03583	0.96479	-0.00281
0.67286	-0.03502	0.97173	-0.00247
0.68036	-0.03418	0.97834	-0.00218
0.68785	-0.03332	0.98449	-0.00198
0.69535	-0.03244	0.99011	-0.00185
0.70286	-0.03154	0.99520	-0.00176
0.71037	-0.03063	1.00000	-0.00170
0.71789	-0.02970		
0.72542	-0.02877		
0.73296	-0.02784		
0.74051	-0.02690		
0.74805	-0.02596		
0.75560	-0.02503		
0.76315	-0.02409		
0.77069	-0.02316		
0.77824	-0.02222		
0.78579	-0.02128		
0.79333	-0.02034		
0.80088	-0.01940		
0.80841	-0.01846		
0.81595	-0.01752		
0.82347	-0.01659		
0.83099	-0.01567		
0.83851	-0.01476		

Upper Surface

x/c	y/c	x/c	y/c
0.00000	0.00000	0.24467	0.05209
0.00001	0.00038	0.25239	0.05264
0.00039	0.00337	0.26012	0.05318
0.00136	0.00630	0.26785	0.05368
0.00291	0.00908	0.27557	0.05416
0.00505	0.01165	0.28331	0.05461
0.00780	0.01399	0.29104	0.05503
0.01109	0.01619	0.29877	0.05543
0.01488	0.01832	0.30649	0.05581
0.01917	0.02036	0.31421	0.05616
0.02400	0.02226	0.32193	0.05649
0.02934	0.02402	0.32965	0.05678
0.03517	0.02570	0.33737	0.05702
0.04142	0.02730	0.34509	0.05723
0.04803	0.02878	0.35282	0.05741
0.05490	0.03019	0.36055	0.05757
0.06199	0.03154	0.36829	0.05771
0.06922	0.03283	0.37603	0.05784
0.07655	0.03403	0.38377	0.05794
0.08395	0.03519	0.39151	0.05800
0.09139	0.03631	0.39925	0.05803
0.09889	0.03733	0.40699	0.05803
0.10644	0.03830	0.41474	0.05800
0.11402	0.03924	0.42249	0.05795
0.12161	0.04016	0.43026	0.05789
0.12922	0.04108	0.43803	0.05781
0.13683	0.04198	0.44578	0.05772
0.14446	0.04282	0.45354	0.05761
0.15210	0.04363	0.46128	0.05747
0.15977	0.04444	0.46903	0.05730
0.16746	0.04524	0.47677	0.05711
0.17517	0.04602	0.48451	0.05688
0.18289	0.04676	0.49226	0.05662
0.19061	0.04750	0.50001	0.05635
0.19834	0.04822	0.50776	0.05606
0.20606	0.04894	0.51552	0.05575
0.21379	0.04963	0.52328	0.05543
0.22151	0.05029	0.53104	0.05508
0.22923	0.05091	0.53879	0.05472
0.23695	0.05151	0.54654	0.05433
0.24467	0.05209	0.55429	0.05393

Upper Surface (Continued)

x/c	y/c	x/c	y/c
0.55429	0.05393	0.86393	0.02296
0.56202	0.05350	0.87166	0.02198
0.56976	0.05304	0.87939	0.02099
0.57749	0.05256	0.88711	0.01998
0.58522	0.05206	0.89482	0.01896
0.59296	0.05152	0.90253	0.01791
0.60070	0.05097	0.91023	0.01686
0.60844	0.05039	0.91792	0.01580
0.61619	0.04979	0.92559	0.01476
0.62393	0.04918	0.93325	0.01371
0.63168	0.04855	0.94088	0.01265
0.63943	0.04791	0.94846	0.01156
0.64717	0.04726	0.95595	0.01044
0.65491	0.04658	0.96333	0.00931
0.66264	0.04588	0.97052	0.00821
0.67037	0.04516	0.97741	0.00712
0.67810	0.04442	0.98387	0.00606
0.68583	0.04365	0.98978	0.00504
0.69356	0.04287	0.99506	0.00410
0.70130	0.04207	1.00000	0.00320
0.70905	0.04125		
0.71680	0.04043		
0.72455	0.03959		
0.73231	0.03875		
0.74006	0.03789		
0.74782	0.03703		
0.75557	0.03615		
0.76333	0.03527		
0.77108	0.03438		
0.77882	0.03348		
0.78656	0.03258		
0.79429	0.03166		
0.80202	0.03072		
0.80975	0.02977		
0.81748	0.02880		
0.82521	0.02782		
0.83295	0.02685		
0.84070	0.02588		
0.84845	0.02491		
0.85619	0.02394		

A.2. Outboard 2xTE Airfoil Coordinates

Lower Surface			
x/c	y/c	x/c	y/c
0.00000	0.00000	0.24457	-0.04750
0.00026	-0.00230	0.25206	-0.04777
0.00105	-0.00512	0.25956	-0.04802
0.00226	-0.00796	0.26706	-0.04826
0.00414	-0.01061	0.27456	-0.04847
0.00669	-0.01307	0.28207	-0.04866
0.00987	-0.01538	0.28957	-0.04884
0.01361	-0.01758	0.29708	-0.04900
0.01788	-0.01972	0.30459	-0.04914
0.02270	-0.02172	0.31210	-0.04926
0.02804	-0.02355	0.31961	-0.04936
0.03383	-0.02526	0.32712	-0.04944
0.04000	-0.02685	0.33464	-0.04951
0.04647	-0.02833	0.34217	-0.04956
0.05319	-0.02969	0.34969	-0.04960
0.06008	-0.03097	0.35722	-0.04963
0.06710	-0.03218	0.36475	-0.04965
0.07423	-0.03331	0.37228	-0.04966
0.08143	-0.03436	0.37981	-0.04965
0.08869	-0.03537	0.38733	-0.04963
0.09598	-0.03633	0.39486	-0.04959
0.10329	-0.03724	0.40238	-0.04955
0.11061	-0.03810	0.40991	-0.04948
0.11796	-0.03891	0.41744	-0.04941
0.12533	-0.03967	0.42497	-0.04932
0.13272	-0.04038	0.43250	-0.04922
0.14012	-0.04105	0.44002	-0.04910
0.14754	-0.04169	0.44755	-0.04898
0.15497	-0.04230	0.45508	-0.04884
0.16241	-0.04288	0.46260	-0.04869
0.16986	-0.04343	0.47012	-0.04853
0.17732	-0.04395	0.47764	-0.04835
0.18478	-0.04444	0.48516	-0.04816
0.19225	-0.04492	0.49267	-0.04795
0.19972	-0.04537	0.50018	-0.04772
0.20718	-0.04579	0.50769	-0.04748
0.21465	-0.04618	0.51520	-0.04722
0.22213	-0.04655	0.52270	-0.04694
0.22960	-0.04689	0.53020	-0.04665
0.23709	-0.04721	0.53769	-0.04633

Lower Surface (Continued)

x/c	y/c	x/c	y/c
0.54518	-0.04600	0.84456	-0.01622
0.55267	-0.04565	0.85205	-0.01534
0.56014	-0.04527	0.85954	-0.01447
0.56761	-0.04487	0.86702	-0.01362
0.57507	-0.04444	0.87449	-0.01279
0.58253	-0.04398	0.88196	-0.01197
0.58998	-0.04350	0.88943	-0.01117
0.59743	-0.04298	0.89690	-0.01038
0.60488	-0.04242	0.90437	-0.00962
0.61233	-0.04184	0.91183	-0.00887
0.61978	-0.04122	0.91928	-0.00814
0.62723	-0.04058	0.92673	-0.00744
0.63469	-0.03992	0.93417	-0.00676
0.64216	-0.03923	0.94158	-0.00611
0.64964	-0.03852	0.94896	-0.00549
0.65711	-0.03779	0.95628	-0.00491
0.66458	-0.03706	0.96350	-0.00438
0.67206	-0.03630	0.97056	-0.00388
0.67953	-0.03553	0.97737	-0.00345
0.68701	-0.03474	0.98380	-0.00309
0.69448	-0.03393	0.98971	-0.00279
0.70195	-0.03310	0.99503	-0.00254
0.70943	-0.03226	1.00000	-0.00232
0.71691	-0.03140		
0.72439	-0.03053		
0.73189	-0.02964		
0.73939	-0.02876		
0.74689	-0.02786		
0.75440	-0.02696		
0.76191	-0.02607		
0.76943	-0.02517		
0.77695	-0.02427		
0.78447	-0.02337		
0.79198	-0.02247		
0.79950	-0.02157		
0.80702	-0.02068		
0.81453	-0.01978		
0.82205	-0.01889		
0.82956	-0.01799		
0.83706	-0.01710		

Upper Surface

x/c	y/c	x/c	y/c
0.00000	0.00000	0.24583	0.05205
0.00004	0.00064	0.25352	0.05260
0.00056	0.00360	0.26121	0.05312
0.00157	0.00654	0.26890	0.05362
0.00310	0.00939	0.27659	0.05409
0.00539	0.01194	0.28429	0.05454
0.00823	0.01428	0.29198	0.05496
0.01160	0.01647	0.29968	0.05535
0.01548	0.01861	0.30737	0.05573
0.01990	0.02064	0.31507	0.05607
0.02486	0.02254	0.32275	0.05640
0.03033	0.02431	0.33044	0.05668
0.03626	0.02599	0.33812	0.05693
0.04260	0.02755	0.34581	0.05715
0.04926	0.02903	0.35351	0.05735
0.05617	0.03042	0.36121	0.05751
0.06328	0.03175	0.36892	0.05766
0.07053	0.03302	0.37662	0.05778
0.07787	0.03421	0.38432	0.05788
0.08528	0.03537	0.39202	0.05795
0.09274	0.03645	0.39973	0.05798
0.10024	0.03746	0.40745	0.05799
0.10779	0.03843	0.41517	0.05799
0.11537	0.03936	0.42289	0.05797
0.12299	0.04028	0.43062	0.05793
0.13062	0.04119	0.43834	0.05786
0.13826	0.04208	0.44606	0.05777
0.14591	0.04291	0.45378	0.05767
0.15357	0.04372	0.46150	0.05754
0.16124	0.04452	0.46922	0.05740
0.16893	0.04531	0.47693	0.05723
0.17661	0.04607	0.48464	0.05704
0.18431	0.04681	0.49235	0.05682
0.19201	0.04754	0.50006	0.05657
0.19970	0.04825	0.50778	0.05630
0.20740	0.04895	0.51550	0.05602
0.21509	0.04962	0.52323	0.05571
0.22277	0.05027	0.53096	0.05539
0.23046	0.05089	0.53868	0.05506
0.23814	0.05148	0.54640	0.05470

Upper Surface (Continued)

x/c	y/c	x/c	y/c
0.55412	0.05433	0.86258	0.02549
0.56183	0.05394	0.87030	0.02457
0.56954	0.05353	0.87802	0.02363
0.57724	0.05309	0.88573	0.02270
0.58494	0.05263	0.89344	0.02175
0.59265	0.05214	0.90115	0.02080
0.60035	0.05163	0.90885	0.01984
0.60806	0.05110	0.91654	0.01887
0.61577	0.05055	0.92423	0.01788
0.62348	0.04998	0.93191	0.01688
0.63120	0.04940	0.93959	0.01587
0.63892	0.04881	0.94724	0.01487
0.64663	0.04820	0.95483	0.01388
0.65434	0.04757	0.96232	0.01289
0.66205	0.04692	0.96964	0.01190
0.66975	0.04626	0.97669	0.01091
0.67745	0.04558	0.98335	0.00995
0.68515	0.04487	0.98946	0.00906
0.69286	0.04415	0.99492	0.00826
0.70056	0.04342	1.00000	0.00750
0.70826	0.04266		
0.71598	0.04189		
0.72369	0.04110		
0.73141	0.04031		
0.73913	0.03951		
0.74685	0.03870		
0.75457	0.03788		
0.76230	0.03705		
0.77002	0.03622		
0.77774	0.03537		
0.78546	0.03452		
0.79317	0.03366		
0.80089	0.03279		
0.80860	0.03192		
0.81630	0.03103		
0.82400	0.03012		
0.83171	0.02920		
0.83942	0.02827		
0.84713	0.02734		
0.85485	0.02641		

A.3. Inboard Airfoil Coordinates

Lower Surface			
x/c	y/c	x/c	y/c
0.00000	0.00000	0.20309	-0.07692
0.00012	-0.00305	0.21111	-0.07790
0.00026	-0.00441	0.21915	-0.07886
0.00045	-0.00568	0.22719	-0.07977
0.00067	-0.00691	0.23525	-0.08065
0.00108	-0.00870	0.24331	-0.08150
0.00195	-0.01150	0.25138	-0.08232
0.00328	-0.01475	0.25945	-0.08310
0.00487	-0.01782	0.26753	-0.08385
0.00679	-0.02071	0.27560	-0.08456
0.00902	-0.02364	0.28367	-0.08524
0.01166	-0.02650	0.29175	-0.08589
0.01467	-0.02930	0.29982	-0.08650
0.01803	-0.03203	0.30789	-0.08707
0.02179	-0.03468	0.31596	-0.08761
0.02594	-0.03725	0.32403	-0.08811
0.03049	-0.03973	0.33209	-0.08857
0.03539	-0.04212	0.34015	-0.08899
0.04061	-0.04443	0.34821	-0.08937
0.04604	-0.04668	0.35627	-0.08972
0.05171	-0.04870	0.36433	-0.09002
0.05776	-0.05042	0.37238	-0.09028
0.06423	-0.05205	0.38043	-0.09050
0.07110	-0.05365	0.38848	-0.09068
0.07835	-0.05522	0.39652	-0.09082
0.08584	-0.05683	0.40457	-0.09091
0.09347	-0.05847	0.41261	-0.09096
0.10113	-0.06014	0.42065	-0.09097
0.10877	-0.06180	0.42870	-0.09093
0.11642	-0.06336	0.43675	-0.09086
0.12411	-0.06484	0.44480	-0.09074
0.13185	-0.06626	0.45285	-0.09058
0.13964	-0.06763	0.46091	-0.09037
0.14746	-0.06895	0.46897	-0.09013
0.15533	-0.07021	0.47705	-0.08985
0.16323	-0.07143	0.48512	-0.08952
0.17116	-0.07261	0.49321	-0.08917
0.17911	-0.07375	0.50130	-0.08878
0.18708	-0.07485	0.50940	-0.08835
0.19507	-0.07590	0.51750	-0.08789

Lower Surface (Continued)

x/c	y/c	x/c	y/c
0.52559	-0.08740	0.84449	-0.03605
0.53369	-0.08688	0.85250	-0.03419
0.54179	-0.08632	0.86051	-0.03235
0.54988	-0.08573	0.86850	-0.03054
0.55797	-0.08511	0.87649	-0.02875
0.56607	-0.08446	0.88447	-0.02699
0.57415	-0.08378	0.89244	-0.02525
0.58224	-0.08306	0.90040	-0.02354
0.59031	-0.08232	0.90836	-0.02187
0.59838	-0.08154	0.91632	-0.02023
0.60642	-0.08074	0.92426	-0.01860
0.61444	-0.07990	0.93218	-0.01702
0.62242	-0.07902	0.94007	-0.01549
0.63039	-0.07809	0.94787	-0.01399
0.63832	-0.07713	0.95555	-0.01256
0.64623	-0.07612	0.96308	-0.01117
0.65412	-0.07504	0.97042	-0.00985
0.66200	-0.07391	0.97741	-0.00862
0.66987	-0.07273	0.98391	-0.00747
0.67773	-0.07151	0.98981	-0.00647
0.68558	-0.07022	0.99508	-0.00558
0.69342	-0.06887	1.00000	-0.00475
0.70128	-0.06747		
0.70915	-0.06601		
0.71702	-0.06452		
0.72489	-0.06297		
0.73277	-0.06138		
0.74066	-0.05972		
0.74858	-0.05803		
0.75652	-0.05632		
0.76447	-0.05457		
0.77243	-0.05277		
0.78041	-0.05095		
0.78842	-0.04912		
0.79644	-0.04726		
0.80446	-0.04539		
0.81248	-0.04352		
0.82048	-0.04164		
0.82847	-0.03976		
0.83647	-0.03790		

Upper Surface

x/c	y/c	x/c	y/c
0.00000	0.00000	0.22467	0.08553
0.00018	0.00310	0.23257	0.08616
0.00070	0.00628	0.24049	0.08675
0.00158	0.00953	0.24841	0.08730
0.00286	0.01282	0.25636	0.08782
0.00457	0.01615	0.26431	0.08830
0.00672	0.01951	0.27227	0.08874
0.00933	0.02287	0.28024	0.08915
0.01240	0.02624	0.28822	0.08952
0.01593	0.02960	0.29621	0.08987
0.01988	0.03294	0.30421	0.09018
0.02423	0.03625	0.31221	0.09046
0.02892	0.03950	0.32023	0.09071
0.03392	0.04268	0.32824	0.09094
0.03922	0.04577	0.33626	0.09114
0.04477	0.04869	0.34429	0.09130
0.05047	0.05148	0.35232	0.09144
0.05622	0.05420	0.36035	0.09156
0.06205	0.05671	0.36838	0.09165
0.06808	0.05900	0.37641	0.09171
0.07441	0.06107	0.38445	0.09175
0.08102	0.06296	0.39248	0.09176
0.08787	0.06479	0.40052	0.09175
0.09491	0.06654	0.40855	0.09171
0.10208	0.06821	0.41659	0.09164
0.10936	0.06979	0.42462	0.09155
0.11673	0.07130	0.43265	0.09143
0.12418	0.07273	0.44068	0.09128
0.13169	0.07408	0.44870	0.09111
0.13925	0.07536	0.45672	0.09092
0.14686	0.07657	0.46474	0.09069
0.15451	0.07771	0.47274	0.09044
0.16220	0.07879	0.48075	0.09016
0.16992	0.07982	0.48874	0.08984
0.17767	0.08078	0.49673	0.08950
0.18545	0.08170	0.50471	0.08913
0.19325	0.08256	0.51269	0.08872
0.20108	0.08337	0.52067	0.08828
0.20892	0.08413	0.52864	0.08781
0.21679	0.08485	0.53661	0.08730

Upper Surface (Continued)

x/c	y/c	x/c	y/c
0.54459	0.08677	0.86110	0.04028
0.55256	0.08620	0.86893	0.03853
0.56052	0.08559	0.87676	0.03676
0.56849	0.08496	0.88458	0.03496
0.57645	0.08430	0.89239	0.03314
0.58442	0.08360	0.90020	0.03128
0.59238	0.08287	0.90800	0.02941
0.60034	0.08211	0.91580	0.02750
0.60829	0.08132	0.92359	0.02557
0.61625	0.08050	0.93136	0.02362
0.62420	0.07965	0.93912	0.02165
0.63215	0.07876	0.94685	0.01966
0.64009	0.07785	0.95452	0.01765
0.64803	0.07690	0.96210	0.01565
0.65597	0.07592	0.96950	0.01367
0.66391	0.07492	0.97663	0.01174
0.67184	0.07388	0.98334	0.00990
0.67977	0.07281	0.98946	0.00820
0.68770	0.07172	0.99492	0.00668
0.69563	0.07059	1.00000	0.00525
0.70355	0.06943		
0.71146	0.06825		
0.71938	0.06703		
0.72729	0.06578		
0.73519	0.06451		
0.74309	0.06321		
0.75099	0.06188		
0.75888	0.06052		
0.76678	0.05913		
0.77466	0.05771		
0.78254	0.05626		
0.79042	0.05479		
0.79829	0.05329		
0.80616	0.05176		
0.81402	0.05020		
0.82188	0.04862		
0.82974	0.04700		
0.83759	0.04536		
0.84543	0.04370		
0.85327	0.04200		

Appendix B. MSES Flowfield Data Extraction

MSES is a multi-element airfoil analysis code that couples an Euler solver in the inviscid region with an integral boundary layer solver in the viscous boundary layer region. Because solutions are obtained in a matter of minutes, MSES is favorable over full Navier-Stokes solvers as a tool for airfoil design and analysis. Once a solution is found with MSES, the user can access numerous forms of output:

- Graphical pressure and Mach number distributions over the airfoil surface
- Contour plots the pressure, Mach number, and density throughout the flowfield
- Numerical values of lift, drag, and pitching moment
- Numerical values of the pressure distribution, Mach number, and boundary layer quantities over the surface of the airfoil

The Embedded region approach required velocity, temperature, and pressure values through the flowfield as boundary conditions. While MSES does find graphically output flowfield quantities in contour plots, a numerical output of the flowfield quantities was originally not available. Fortunately, the MSES source code was available and could be examined to find a way to retrieve the flowfield data. Because the flowfield data is used in the MSES “mplot” postprocessor, the files and routines associated with this portion of the MSES code were examined. The “contpl.f” file and the “mplot.f” file were found to be the most useful in provided clues to how the flowfield quantities were stored.

When an airfoil problem is setup in MSES, only three flowfield quantities are required as input: the freestream Mach number M_∞ , the Reynolds number based on the chord Re_c , and the angle of attack α . MSES internally sets two reference quantities: the freestream stagnation density, $\rho_{0_\infty} = 1$, and the freestream stagnation speed of sound, $a_0 = 1$. All other quantities are normalized by these two quantities. When the flowfield data is extracted from MSES, ρ_0 and a_0 must be specified for the flow, and the flowfield data must be properly computed using ρ_0 and a_0 . Table B.1 lists flowfield properties, the associated MSES variables, and the symbolic representation of each MSES variable.

Table B.1: Flowfield quantities from MSES.

Flowfield Quantity	MSES Representation	Symbolic Representation of MSES Output
Freestream enthalpy, h_∞	HINF	$\frac{h_\infty}{a_0^2}$
Freestream velocity, U_∞	QINF	$\frac{U_\infty}{a_0}$
Freestream dynamic pressure, q_∞	QU	$\frac{q_\infty}{\rho_{0_\infty} \cdot a_0^2}$
Freestream stagnation density, ρ_{0_∞}	RSTINF	$\frac{\rho_{0_\infty}}{\rho_{0_\infty}}$
Freestream density, ρ_∞	RHOINF	$\frac{\rho_\infty}{\rho_{0_\infty}}$
Freestream stagnation pressure, p_{0_∞}	PSTINF	$\frac{p_{0_\infty}}{\rho_{0_\infty} \cdot a_0^2}$
Freestream pressure, p_∞	PINF	$\frac{p_\infty}{\rho_{0_\infty} \cdot a_0^2}$
x-coordinate, $\frac{x}{c}$	X(I,J)	$\frac{x}{c}$
y-coordinate, $\frac{y}{c}$	Y(I,J)	$\frac{y}{c}$
Velocity, U	Q(I,J)	$\frac{U}{a_0}$
Pressure, p	P(I,J)+PSTINF	$\frac{p}{\rho_{0_\infty} \cdot a_0^2}$
Pressure coefficient, C_p	(PI(IJ)-DPINF)/QU	C_p
Mach number, M	SQRT(ABS(MACHSQ))	M
Density, ρ	R(I,J)	$\frac{\rho}{\rho_{0_\infty}}$
x-component of velocity, u	Q(I,J)*(DELTAX/DELTAS)	$\frac{u}{a_0}$
y-velocity of velocity, v	Q(I,J)*(DELTAY/DELTAS)	$\frac{v}{a_0}$
Mach number squared, M^2	R(I,J)*Q(I,J)**2/ (GAM*(P(I,J)+PSTINF))	M^2

It is important to note that MSES aligns the grid with the streamlines. Therefore, the components of the local velocity vector, u and v can be found simply using the slope

between its adjacent points along the streamline. For the point (x_i, y_i) , with adjacent points (x_{i-1}, y_{i-1}) and (x_{i+1}, y_{i+1}) :

$$\begin{aligned} u_i &= U_i \cdot \left(\frac{\Delta x_i}{\Delta s_i} \right) \\ v_i &= U_i \cdot \left(\frac{\Delta y_i}{\Delta s_i} \right) \end{aligned} \tag{B.1}$$

where:

$$\begin{aligned} \Delta x_i &= x_{i+1} - x_{i-1} \\ \Delta y_i &= y_{i+1} - y_{i-1} \\ \Delta s_i &= \sqrt{(x_{i+1} - x_{i-1})^2 + (y_{i+1} - y_{i-1})^2} \end{aligned} \tag{B.2}$$

The following portion of code was inserted into the “contpl.f” routine. When the MSES “mplot” command is run, this portion of code is run and the flowfield data is extracted from MSES and written to two files: the flow properties through the entire flowfield are output to the file “dataMSES.txt”; various other quantities are output to the file “data2MSES.txt.”

```

=====
C   This section of code was added to output the following flowfield
C   properties: x, y, U, u, v, M, p, Cp, rho.  The data can then be
C   read by a program such as TechPlot.
C
C   Vance Dippold, III
C   December, 2002
C-----
      OPEN(40,FILE='dataMSES.txt',STATUS='UNKNOWN')
      OPEN(41,FILE='data2MSES.txt',STATUS='UNKNOWN')

C TechPlot File Header information
      IIM1=II-1
      JJM1=JJ-1
4011 FORMAT (A21)
4012 FORMAT (A11,1X,A12,1X,A12,1X,A12,1X,A12,1X,A12,1X,A12,1X,A13,1X,A15,
      &      1X,A12,1X,A12)
4013 FORMAT (A29,I4,A4,I3,A9)
4015 FORMAT (A26,1X,E17.8E2)
4016 FORMAT (A40)
4017 FORMAT (A26,1X,I4)
      WRITE(41,4016) 'Various MSES calculated data & properties'
      WRITE(41,4015) 'Hinf:   h/(a0^2)           =', HINF
      WRITE(41,4015) 'Qinf:   Uinf/a0             =', QINF
      WRITE(41,4015) 'Qu:     q/(rho0*a0^2)          =', QU
      WRITE(41,4015) 'RSTinf: rho0/rho0             =', RSTINF
      WRITE(41,4015) 'RHOinf: rhoinf/rho0          =', RHOINF
      WRITE(41,4015) 'PSTout: p0/(rho0*a0^2)        =', PSTOUT
      WRITE(41,4015) 'PSTinf: p???(rho0*a0^2)       =', PSTINF
      WRITE(41,4015) 'Pinf:   pinf/(rho0*a0^2)       =', PINF
      WRITE(41,4015) 'DPinf:  (pinf-p0inf)           =', DPINF
      WRITE(41,4017) 'No. I elements: II             =', II
      WRITE(41,4017) 'No. J elements: JJ             =', JJ
      WRITE(41,4017) 'No. I elements: II-1           =', IIM1
      WRITE(41,4017) 'No. J elements: JJ-1           =', JJM1

      WRITE(40,4011) 'TITLE = "MSES Output"'
      WRITE(40,4012) 'VARIABLES =', 'x/c','y/c','V/a0',
      &      'Vx/a0','Vy/a0','M','p/(rho0*a0^2)',
      &      'Cp','rho/rho0'
      WRITE(40,4013) 'ZONE T="MSES zone 1, K=1", I=', IIM1, ', J=',
      &      JJM1, ', F=POINT'

      DPINF = PINF-PSTINF
      DO 4000 J=1, JJM1
C       IF(JSTAG(J).GT.0) GO TO 4000
      DO 4001 I=1, IIM1

C Velocity Vector calculation
      IP1=I+1
      IM1=I-1
      IF (I.EQ.1) THEN
          DELTAX=(X(IP1,J)-X(I,J))
          DELTAY=(Y(IP1,J)-Y(I,J))
          DELTAS=SQRT(DELTA X*DELTA X+DELTA Y*DELTA Y)
      ELSEIF (I.EQ.II) THEN
          DELTAX=(X(I,J)-X(IM1,J))

```

```

        DELTAY=(Y(I,J)-Y(IM1,J))
        DELTAS=SQRT(DELTAX*DELTAX+DELTAY*DELTAY)
    ELSE
        DELTAX=0.5*(X(IP1,J)-X(IM1,J))
        DELTAY=0.5*(Y(IP1,J)-Y(IM1,J))
        DELTAS=SQRT(DELTAX*DELTAX+DELTAY*DELTAY)
    ENDIF
    VELX=Q(I,J)*(DELTAX / DELTAS)
    VELY=Q(I,J)*(DELTAY / DELTAS)

C Pressure calculation
    PRESS = P(I,J)+PSTINF

C Pressure Coefficient calculation
    PRESCOEF = (PI(I,J)-DPINF)/QU

C Mach Number calculation
    MACHSQ = R(I,J)*Q(I,J)**2 / (GAM*(P(I,J)+PSTINF))
C    MACH = SQRT(MAX(MACHSQ,0.0))
    MACH = SQRT(ABS(MACHSQ))

C Write Output file
4014     FORMAT (9E17.8E2)
        WRITE(40,4014) X(I,J), Y(I,J), Q(I,J), VELX, VELY, MACH,
    &                PRESS, PRESCOEF, R(I,J)
4001     CONTINUE
4000     CONTINUE
        CLOSE(40)
C=====
C

```

Vita

Vance Fredrick Dippold, III was born on April 26, 1978 in Washington, DC. He is the first son of Vance and Sandy Dippold, Jr., and he has a young brother, Sam, and younger sister, Laurie. Vance and his family lived in Waldorf, Maryland, before moving to La Plata, Maryland when he was eight. At the age of 18, Vance received his high school diploma from La Plata High School, where he graduated at the top of his class. Vance began his undergraduate studies at Virginia Tech in the fall of 1996, dual-majoring in Aerospace Engineering and Ocean Engineering. In May of 2000, Vance completed his Bachelor of Science degree in Aerospace Engineering at Virginia Tech. His senior aircraft design team received Second Place in the 1999-2000 AIAA Team Aircraft Design Competition. Vance took a year off from studies before pursuing a graduate degree. During this time, Vance worked as an assistant in the Aerospace and Ocean Engineering Machine Shop at Virginia Tech, and he completed a four-month internship with Eagles' Wings Ministries in Buffalo, New York. Vance returned to Virginia Tech in the summer of 2001 to begin his graduate work. After completing his Master of Science degree, Vance plans to work with NASA Glenn Research Center in Cleveland, Ohio.